A MULTI-DIMENSIONAL APPROACH TO THE CHARACTERIZATION OF EXOPLANETARY ATMOSPHERES

A DISSERTATION SUBMITTED TO THE GRADUATE SCHOOL OF
BROWN UNIVERSITY IN PARTIAL FULFILLMENT OF THE
REQUIREMENTS FOR THE DEGREE OF

DOCTOR OF PHILOSOPHY

IN

PHYSICS

MAY 2019

By
Brian M. Kilpatrick

Dissertation Committee:

G. Tucker, Chairperson
N. Lewis, Reader
I. Dell'Antonio, Reader

This dissertation by Brian M. Kilpatrick is accepted in its present form by the Department of Physics as satisfying the dissertation requirement for the degree of Doctor of Philosophy.

DISSERTATION COMMITTEE

Gregory S. Tucker, Chairperson

Nikole K. Lewis, Reader

Ian Dell'Antonio, Reader

APPROVED BY THE GRADUATE COUNCIL

Andrew G. Campbell, Dean of the Graduate School

Curriculum Vitae

Brian M. Kilpatrick

Brian Kilpatrick is a graduate student and NASA Earth and Space Science Fellow pursuing his Ph.D. in physics at Brown University. His research focuses on the characterization of exoplanetary atmospheres under the advisement of Gregory Tucker and Nikole Lewis (Cornell University). Brian grew up on the shores of the Chesapeake Bay in West River, MD. He spent most of the summers of his youth crabbing, sailing, and playing lacrosse. He is a veteran of the United States Marine Corps. After his military service, Brian completed his B.S. in Physics at Kutztown University of Pennsylvania graduating Summa Cum Laude. During his time at KU he performed research on the quantum behavior of ultra cold atoms with Prof. Kunal Das.

Brian resides in Portsmouth, Rhode Island with his wife and three children. They can often be found enjoying the neighborhood parks or playing on a Narragansett beach.

Education

Ph.D. Physics, *Brown University* — expected May 2019
Thesis: A Multi-Faceted Approach to the Characterization of Exoplanetary Atmospheres

M.Sc. Physics, *Brown University* — May 2015

B.S. Physics, *Kutztown University* — December 2013
Summa Cum Laude

Selected Professional Appointments

Graduate Research Fellow, *Brown University* — 2016-Present
Performing analysis of transit, eclipse, and full orbit phase curve observations from both the *Hubble Space Telescope* and *Spitzer Space Telescope*. Developing and employing novel methods to link observational data to the physical and chemical processes occurring in exoplanetary atmospheres.

Adjunct Instructor of Physics, Astronomy and Geophysics, *Connecticut College* — 2017-2018

Selected Honors and Awards

Sigma Xi The Scientific Research Honor Society	2019
NASA Earth and Space Science Fellow	2017-2019
NASA Rhode Island Space Grant Fellow (declined)	2017
Roy W. Hamme Memorial Award in Physical Sciences, *Kutztown University*	2013
Phi Kappa Phi National Honor Society	2012
Sigma Pi Sigma Physics Honor Society	2012
Letter of Commendation, Commanding Officer, Naval Academy Preparatory School	2000
Letter of Commendation Commanding General, 3d MarDiv	2000
Meritorius Mast, Honor Graduate, Marine Corps Personnel and Administration School	1999
Commandant of the Marine Corps Achievement Award	1999

Funded Grants and Observing Proposals

NASA Earth and Space Science Fellowship: 2017-2018
Probing the 3-D Nature of Exoplanet Atmospheres.

Hubble Space Telescope, (Co-I, PI Fraine) 2018
WFC3-UVIS Eclipse Observation of WASP-43b: Helping James Webb See Through the Clouds.

James Webb Space Telescope, (Co-I, PI Natalie Batalha) 2017
The Transiting Exoplanet Community Early Release Science Program

Spitzer Space Telescope, (Co-I, PI Fraine) 2017
Maximizing JWST GTO Observations of HAT-P-26b with Time-Critical Spitzer Eclipse Measurements

Hubble Space Telescope, (Co-I, PI Kevin Stevenson) 2017
A Preparatory Program to Identify the Single Best Transiting Exoplanet for *JWST* Early Release Science Cycle 24 Program GO-14642

Spitzer Space Telescope, (Co-I, PI Laetitia Delrez) 2017
Improved characterization of the TRAPPIST-1 planets Cycle 13 DDT Program 13175

Acknowledgements

I wish to thank my advisor Greg Tucker for allowing me to forge a new trail in my studies at Brown. It was his interest in a new and burgeoning topic and the boldness to branch out into something new that provided me the opportunity to discover this wonderful field. If not for Nikole Lewis this boldness to venture into the unknown may have ended up as a fools errand instead of success. Her knowledge, guidance and kindness were essential to my success. As you continue your immersion into a new faculty role, I have every confidence that your students will be well mentored and given every opportunity to succeed. Nikole once told me to make sure there was never just a single point of failure my support system. I was fortunate to have a cast of mentors who, collectively, were always there for me. Tiffany Kataria, Kevin Stevenson, and Hannah Wakeford were pillars of support that I leaned on time and time again. Your mentorship was critical and I thank you for investing your time in me.

The Brown University Physics Department has been a supportive and fun place to spend five years of my life. I chose to come to Brown because of the camaraderie I felt amongst the students, faculty, and staff. I developed timeless relationships with people from all three of those categories and will miss seeing you all on the rare occasions I leave the basement.

I would be remiss not to mention the amazing Physics faculty at Kutztown University. When I walked onto that campus I was just beginning to form my vision for where I wanted this journey to go. Prof. Kunal Das opened my eyes to the possibilities that existed for me and showed me what research was all about. Prof. Sudarshan Fernando built the basis of my knowledge of physics in a way that made me love my work. Prof. Phill Reed has embraced my slow and steady drift

into astronomy and astrophysics (much to his own delight, I'm sure) and has been a friend and supporter throughout my graduate career. Thank you all for believing in me and getting me to believe in myself.

To my family, there are no words to describe the gratitude I owe you for your many sacrifices. You have endured the long hours, the moves, the travel and , of course, the cranky husband/father. Your belief and support is the only reason I am here today. Melissa, thank you for your unrelenting love. You, more than anyone, have had to give in order for this to happen. You are an amazing woman and I hope that over the course of our lifetime I am able to come close to showing you the same support you have shown me.

To my parents, I made it....finally. Your patience has paid off. You taught me from a young age what it meant to work hard and chase your dreams. Then gave me every opportunity you could to make sure that I could chase them. I had to find this dream on my own, decide that it was what I wanted and do it for myself. Thanks for letting me walk my own road, providing course corrections along the way, and being willing to walk along with me when I needed you.

Though victory's proof of the skill you possess,
Defeat is the proof of your grit;
A weakling can smile in his days of success,
But at trouble's first sign he will quit.
So the test of the heart and the test of your pluck
Isn't skies that are sunny and fair,
But how do you stand to the blow that is struck
And how do you battle despair?

A fool can seem wise when the pathway is clear
And it's easy to see the way out,
But the test of man's judgment is something to fear,
And what does he do when in doubt?
And the proof of his faith is the courage he shows
When sorrows lie deep in his breast;
It's the way that he suffers the griefs that he knows
That brings out his worst or his best.

The test of a man is how much he will bear
For a cause which he knows to be right,
How long will he stand in the depths of despair,
How much will he suffer and fight?
There are many to serve when the victory's near
And few are the hurts to be borne,
But it calls for a leader of courage to cheer
The men in a battle forlorn.

It's the way you hold out against odds that are great
That proves what your courage is worth,
It's the way that you stand to the bruises of fate
That shows up your stature and girth.
And victory's nothing but proof of your skill,
Veneered with a glory that's thin,
Unless it is proof of unfaltering will,
And unless you have suffered to win.

Edgar Albert Guest

Table of Contents

List of Tables

List of Figures

Chapter 1

Introduction: Exoplanets from Detection to Characterization

1.1 Exoplanet Populations

The field of exoplanetary science is a young field in comparison to many other sub fields in astrophysics and astronomy. Science in the field has blossomed from its infancy to a diverse and thriving community of researchers exploring topics from planet formation to astro-biology and everything in between over the short span of less than 25 years. Discoveries of new exoplanets were slowly increasing by tens of planets per year, mostly via the radial velocity method during the end of the 1990's and beginning of the 2000's. The discovery of the first transiting exoplanet (HD 209458b) in 1999 (Charbonneau et al. 2000) demonstrated the potential for a powerful new detection technique that sparked an exponential increase in the number of detections over the next six years shown in Figure 1.1. Many of those detections came as a product of the *Kepler Space Telescope (Kepler)*. *Kepler* was responsible for increasing the number of known exoplanets from several hundred to several thousand in a period of just a few years. It has been the most fruitful exoplanet detection instrument to date and has been the inspiration for the next generation transiting exoplanet detection mission; the *Transiting Exoplanet Survey Satellite (TESS)*.

One of the prime objectives of the *Kepler* mission, and other detection efforts, was to gain an understanding of the population of exoplanets to answer questions like: Are other planetary

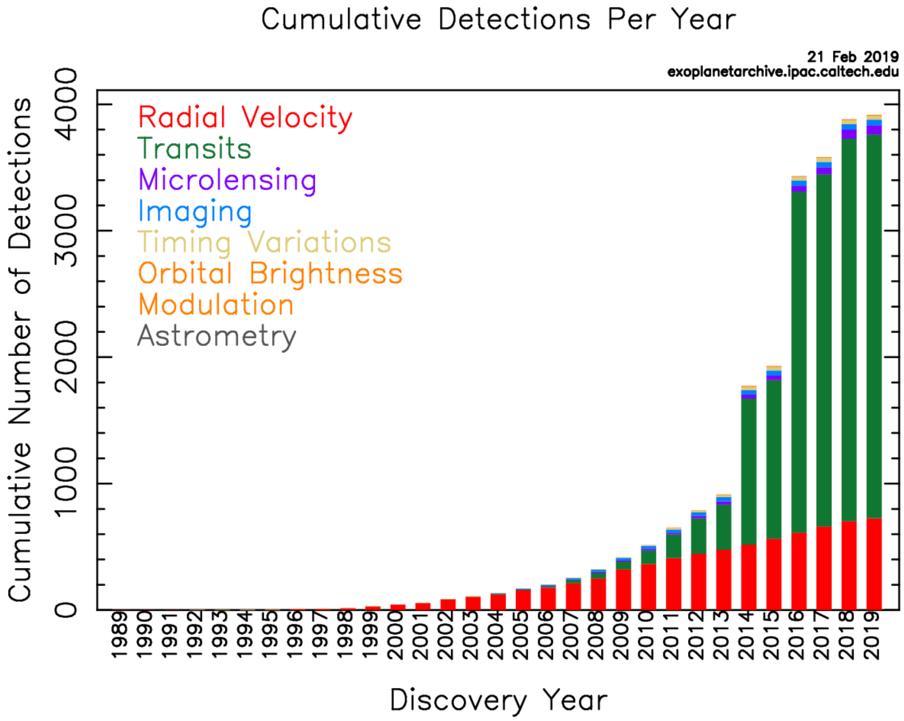

Figure 1.1 Cumulative Exoplanet detections by year. Note the dramatic increases in 2014 and 2016 due to Kepler releases.

systems similar to ours and what are the implications of the distribution of planets for formation theories? Figure 1.2 shows the distribution of exoplanet discoveries in Period vs Mass space. Obvious in this figure are the biases present in each of the observational techniques. Transits detection signal is proportional to the ratio of the radii of the planet and star. Numerous transits are required to establish the presence of a periodic signal and eliminate false positives. As a result, the transit method is more likely to discover large planets at short periods. The radial velocity technique signal strength is proportional to $m_{planet} \times Period^{\frac{1}{3}}$ leading to see more detections at large mass and greater separation. There is still the limitation that numerous orbits are needed to ensure a robust detection and weed out false positives thus limiting the maximum period to reasonable observing times of several (Earth) years.

The sample of known exoplanets is biased as a result of the limitations in our ability to detect them. Many studies have been performed to account for biased detection rates and predict the true distribution of planets. These studies have produced several interesting results about the population

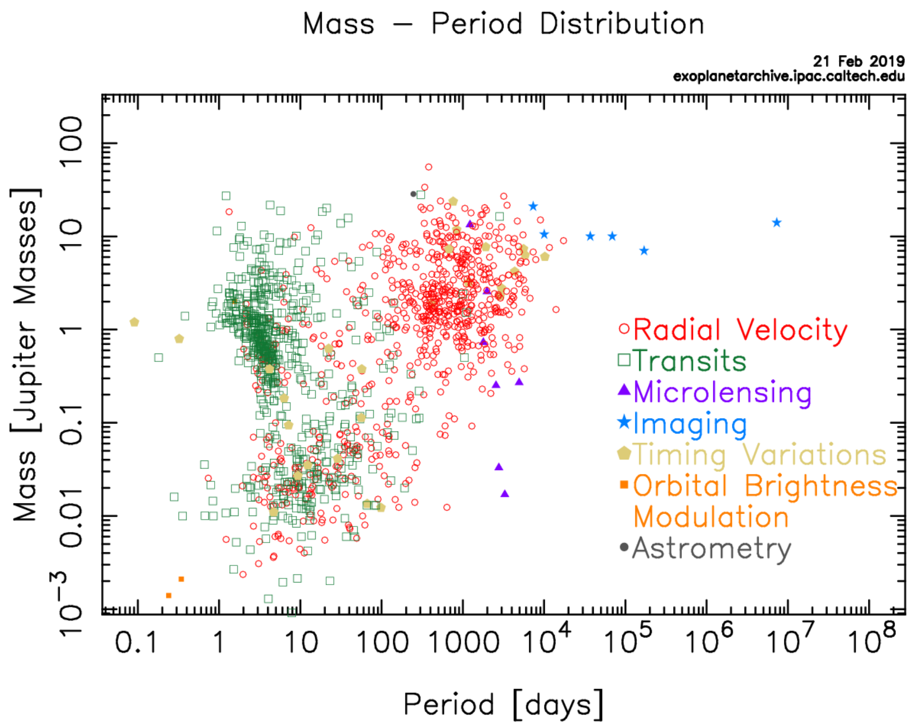

Figure 1.2 Distribution of the known exoplanet population by mass and period. Colors indicate the various detection methods with which they were discovered. The detection bias of each method becomes evident in this space. Transits (green) preferentially detect large short period objects and RV is most sensitive to large long period objects.

of exoplanets in comparison to our solar system (e.g. Howard et al. 2010; Fulton et al. 2017; Bryan et al. 2019) that are beyond the scope of this work. What is noteworthy about the biased sample of exoplanets detected is that they form the entirety of the sample that we can attempt to characterize.

1.2 The Dynamics and Structure of Exoplanet Atmospheres

As we begin a discussion on how to study atmospheres it is important to first have an introduction to some of the key physical components that govern them.

- Hydrostatic Equilibrium
- The role of Temperature
- Rotation (Coriolis Force)

- Scale analysis

As a first assumption we will assume that the atmospheres are in hydrostatic equilibrium. To first order, this simply means that the force of gravity is balanced by a pressure-gradient force. This assumption also implies that vertical and horizontal motions are negligible in comparison to the scale of the atmosphere. By definition, hydrostatic equilibrium means that

$$\frac{dP}{dz} = -\rho g. \tag{1.1}$$

Note that in this case, because we assume the atmosphere to be at rest, the derivative is a full derivative. If we assume the atmosphere to behave as an ideal gas we can substitute for the density so that the expression becomes

$$\frac{dP}{dz} = -P\frac{\mu}{k_B T}g, \tag{1.2}$$

where μ is the mean molecular weight of the atmosphere and k_B is Boltzmann's constant. Grouping like terms results in:

$$\frac{dP}{P} = -g\frac{\mu}{k_B T}dz, \tag{1.3}$$

and integrating both sides:

$$\ln P\Big|_{\infty}^{0} = -\frac{\mu}{k_B T}gz\Big|_{0}^{\infty}. \tag{1.4}$$

Exponating both sides produces an expression for the pressure as a function of altitude:

$$P(z) = e^{-\frac{\mu g}{k_B T}z}. \tag{1.5}$$

We define the scale height, the change in altitude over which the pressure drops by a factor of e as

$$H = \frac{kT}{\mu g}, \tag{1.6}$$

so that the final expression for pressure as a function of altitude is simply

$$P(z) = e^{-\frac{z}{H}}. \tag{1.7}$$

To expand our model of a planetary atmosphere we must now consider an atmosphere in which both horizontal and vertical pressure gradients can initiate winds and planetary rotation influences those flows. We adopt a x,y,z coordinate system for a parcel of air near the surface (East, North, Radially Up). East is defined as the prograde direction and Φ is the latitude. We define the velocity vector $\vec{u}$ as having components (u,v,w). An object in motion on a rotating sphere will experience forces due to rotation. In the horizontal direction the Coriolis Force acts as $-2\vec{\Omega} \times \vec{u}$. The viscous forces experienced are proportional to a coefficient of the atmsmospheric viscosity (ν). The Navier-Stokes equations in this frame of reference are:

$$\frac{Du}{Dt} = \underbrace{\boxed{\frac{-1}{\rho}\frac{\partial P}{\partial x}}}_{\nabla P} + \underbrace{\boxed{\nu\left(\frac{\partial^2 u}{\partial x^2} + \frac{\partial^2 v}{\partial x^2} + \frac{\partial^2 w}{\partial x^2}\right)}}_{\text{Viscous}} - \underbrace{\boxed{2\Omega\left(v\sin\phi - w\cos\phi\right)}}_{\text{Coriolis}}, \tag{1.8}$$

$$\frac{Dv}{Dt} = \boxed{\frac{-1}{\rho}\frac{\partial P}{\partial y}} + \boxed{\nu\left(\frac{\partial^2 u}{\partial y^2} + \frac{\partial^2 v}{\partial y^2} + \frac{\partial^2 w}{\partial y^2}\right)} - \boxed{2\Omega\left(u\sin\phi\right)}, \tag{1.9}$$

$$\frac{Dw}{Dt} = \boxed{g - \frac{1}{\rho}\frac{\partial P}{\partial z}} + \boxed{\nu\left(\frac{\partial^2 u}{\partial z^2} + \frac{\partial^2 v}{\partial z^2} + \frac{\partial^2 w}{\partial z^2}\right)} - \boxed{2\Omega\left(u\cos\phi\right)}. \tag{1.10}$$

Here we use the material derivative ($\frac{Du}{Dt}$), the acceleration of a particular parcel of air. We could also choose to use the local derivative $\left(\frac{\partial u}{\partial t} + u\frac{\partial u}{\partial x} + v\frac{\partial u}{\partial y} + w\frac{\partial u}{\partial z}\right)$. Here we use the material derivative ($\frac{Du}{Dt}$), the acceleration of a particular parcel of air. We could also choose to use the local derivative $\left(\frac{\partial u}{\partial t} + u\frac{\partial u}{\partial x} + v\frac{\partial u}{\partial y} + w\frac{\partial u}{\partial z}\right)$. The three major contributing forces; pressure gradient, viscous, and Coriolis, are labeled and boxed in red. Grouping them in this way allows us to define several ratios that will aid in determining which forces are dominant or negligible in certain situations. These simplifications will lead to scale analysis that will motivate our desire to study hot Jupiter atmospheres.

We first define the Rossby Number Ro as the ratio of the inertial term ($\frac{\partial \vec{u}}{\partial t}$) to the Coriolis term. The Rossby Number scales as

$$\frac{\frac{L}{T^2}}{2\Omega\frac{L}{T}} \sim \frac{U}{fL}, \tag{1.11}$$

where $f \equiv 2\Omega \sin\phi$ A small $Ro(< 0.1)$ means Coriolis forces are important.

The Reynolds Number compares inertial term ($\frac{\partial u}{\partial t}$) to viscous term $\nu\left(\frac{\partial^2 u}{\partial x^2} + \frac{\partial^2 v}{\partial x^2} + \frac{\partial^2 w}{\partial x^2}\right)$. It scales as

$$\frac{\frac{U^2}{L}}{\nu\frac{U}{L^2}} \sim \frac{UL}{\nu}. \tag{1.12}$$

Flows are laminar when $Re < 2300$, transient when $2300 < Re < 4000$, turbulent when $Re > 4000$. In Earth's atmosphere $\nu \sim 10^{-5}$ and $Re \sim 10^{11}$.

There are a couple of relevant length scales that are useful tools in approximating the structure of planetary atmospheres. The Rossby Deformation Radius L_D, is the length scale at which rotational forces dominate (geostrophic flow) in a vertically stratisfied atmosphere.

$$L_D \propto \frac{NH}{f}, \tag{1.13}$$

where N is Brunt–Väisälä frequency, a measure of the vertical stability of the atmosphere.

The Rhines Scale L_β is the length scale at which the growth of eddies is prohibited to due the latitudinal change in Coriolis force. $\beta \equiv \frac{\partial f}{\partial y} \sim 2\Omega\frac{\cos\phi}{a}$.

$$L_\beta \propto \pi\left(\frac{U}{\beta}\right)^{\frac{1}{2}}. \tag{1.14}$$

1.2.1 Hot Jupiters as Chemical and Physical Laboratories

Many of the transiting planets that are amenable to atmospheric characterization with current instruments are close-in giant planets ('hot Jupiters'). They are ideal targets for probing atmospheric physics and chemistry. Close-in planets have short orbital periods, providing ample

Table 1.1. Planetary parameters (Showman et al. 2010)

Planet	a^* (10^3 km)	Rot. Per.$^\sharp$ (Days)	Ω ($\mathrm{rad\,s^{-1}}$)	$\mathrm{g}^\aleph$ ($\mathrm{m\,s^{-2}}$)	$F_*^\square$ ($\mathrm{W\,m^{-2}}$)	$T_\mathrm{e}^\spadesuit$ (K)	$H_p^\dagger$ (km)	$U^\ddagger$ ($\mathrm{m\,s^{-1}}$)	$Ro^\P$	$L_D/a^\clubsuit$	$L_\beta/a^\diamond$
Venus	6.05	243	3×10^{-7}	8.9	2610	232	5	~ 20	10	70	7
Earth	6.37	1	7.27×10^{-5}	9.82	1370	255	7	~ 20	0.1	0.3	0.5
Mars	3.396	1.025	7.1×10^{-5}	3.7	590	210	11	~ 20	0.1	0.6	0.6
Titan	2.575	16	4.5×10^{-6}	1.4	15	85	18	~ 20	2	10	3
Jupiter	71.4	0.4	1.7×10^{-4}	23.1	50	124	20	~ 40	0.02	0.03	0.1
Saturn	60.27	0.44	1.65×10^{-4}	8.96	15	95	39	~ 150	0.06	0.03	0.3
Uranus	25.56	0.72	9.7×10^{-5}	8.7	3.7	59	25	~ 100	0.1	0.1	0.4
Neptune	24.76	0.67	1.09×10^{-4}	11.1	1.5	59	20	~ 200	0.1	0.1	0.6
WASP-12b	128	1.09	6.7×10^{-5}	11.5	8.8×10^6	2500	800	-	0.01–0.3	0.1	0.2–1.5
HD 189733b	81	2.2	3.3×10^{-5}	22.7	4.7×10^5	1200	200	-	0.03–1	0.3	0.4–3
HD 149026b	47	2.9	2.5×10^{-5}	21.9	1.8×10^6	1680	280	-	0.06–2	0.8	0.6–4
HD 209458b	94	3.5	2.1×10^{-5}	10.2	1.0×10^6	1450	520	-	0.04–1	0.4	0.5–3
TrES-2	87	2.4	2.9×10^{-5}	21	1.1×10^6	1475	260	-	0.03–1	0.3	0.4–3
TrES-4	120	3.5	2.0×10^{-5}	7.8	2.5×10^6	1825	870	-	0.03–1	0.4	0.4–3
HAT-P-7b	97	2.2	3.3×10^{-5}	25	4.7×10^6	2130	320	-	0.02–1	0.3	0.4–3
GJ 436b	31	2.6	2.8×10^{-5}	9.8	4.3×10^4	660	250	-	0.1–3	0.7	0.8–5
HAT-P-2b	68	5.6	1.3×10^{-5}	248	9.5×10^5	1400	21	-	0.1–3	1	0.8–5
Corot-Exo-4b	85	9.2	7.9×10^{-6}	13.2	3.0×10^5	1080	300	-	0.1–4	1	0.9–5

Note. — *Equatorial planetary radius. $^\sharp$Assumes synchronous rotation for exoplanets. $^\aleph$ Equatorial gravity at the surface. $^\square$Mean incident stellar flux. $^\spadesuit$Global-average blackbody emission temperature, assuming zero albedo. †Pressure scale height, evaluated at temperature T_e. ‡Rough estimates of characteristic horizontal wind speed. Estimates for Venus and Titan are in the high-altitude superrotating jet; both planets have weaker winds (few $\mathrm{m\,sec^{-1}}$) in the bottom scale height. In all cases, peak winds exceed the listed values by factors of two or more. ¶Rossby number, evaluated in mid-latitudes using wind values listed in Table and $L \sim 2000$ km for Earth, Mars, and Titan, 6000 km for Venus, and 10^4 km for Jupiter, Saturn, Uranus, and Neptune. For exoplanets, we present a range of possible values evaluated with $L = a$ and winds from 100 to $4000\,\mathrm{m\,sec^{-1}}$. $^\clubsuit$Ratio of Rossby deformation radius to planetary radius, evaluated in mid-latitudes with H equal to the pressure scale height and N appropriate for a vertically isothermal temperature profile. $^\diamond$Ratio of Rhines length to planetary radius, calculated using the equatorial value of β and the wind speeds listed in the Table.

opportunities to observe at different geometries throughout their orbit probing multiple spatial regions of the planet. Their large radii produce large transit depths. Hot Jupiters have both low molecular weight atmospheres and high temperatures resulting in scale heights of several hundreds of kilometers in comparison to 8 km on Earth. Hot Jupiters are typically assumed to be tidally locked. Tidally locked planets have one side of the planet under constant flux while the other is dark. This creates large temperature gradients between hemispheres producing an inhomogeneous atmosphere with strong dynamics unlike any in our solar system. Hot Jupiters are also chemical laboratories for elemental composition since we can usually assume them to be Hydrogen dominated with varying degrees of metallicity and in chemical equilibrium due to their high temperatures.

Table 1.1, from Showman et al. (2010) presents the relevant length scales, rotation rates, temperatures and wind speeds for the solar system planets in comparison to a subset of known exoplanets (mostly hot Jupiters). Clearly, hot Jupiters are unique test beds by almost any measure. Their large radii and rotation rates lead to Rossby deformation radii and Rhines scales comparable to the planetary radius. This results in atmospheric dynamics comprised of a few jets and large scale polar vortices. Theory has predicted (Showman et al. 2009) and observations have shown (Agol et al. 2010) that these simple atmospheres are also very stable . The stable and large scale structure of hot Jupiter atmospheres make them ideal candidates for study given limitations in our ability to spatially resolve them.

1.3 Techniques to Characterize Transiting Exoplanets

Observations of transiting exoplanets not only produced the greatest yields in terms of detection, they have also provided the most insight into characterizing these planets. Gaining insight into the complex structure of exoplanet atmospheres is challenging since we do not have the capability to spatially resolve them. They are often too faint to disentangle their light from that of their much brighter host star. Even when directly imaged, exoplanetary signals are often encompassed by a single bright pixel.

Transiting exoplanets offer an opportunity to probe atmospheric properties without being required to resolve the planetary signal from that of the host star. The multiple geometries accessible (see Figure 1.3) probe different regions of the planetary atmosphere and different physical processes.

During primary transit the planet passes in front of its host star with reference to the observer. A fraction of the stellar flux is consequently obscured from the view of the observer. The amount of light blocked, the transit depth, is equivalent to the ratio of the radii squared $(R_p/R_\star)^2$. As previously mentioned, observing photometric transits has been a valuable detection tool but it also provides the first piece of characterization information by constraining the planetary radius (Figure

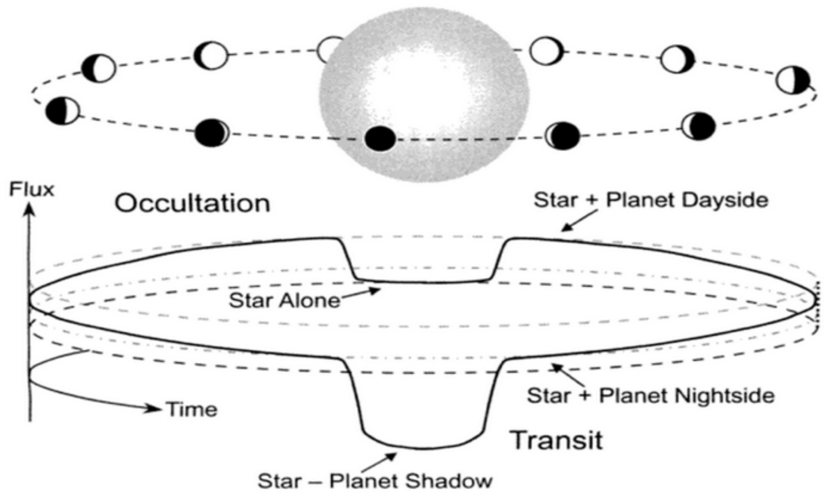

Figure 1.3 Schematic of the multiple transit geometries including Transit, Secondary Eclipse (Occultation), and the Full Orbit Phase Variation. Credit: Winn (2010)

1.4. The addition of RV observation adds constraints on mass as well as tightening constraints on other orbital properties such as inclination and eccentricity. Hot Jupiter planets have large transit signals, a high probability of transit, and large RV signals making them ideal targets.

If the planet has an atmosphere, the radius of the planet may appear to be larger (transit deeper) at wavelengths where elements or molecules in the atmosphere absorb radiation. Broad band photometric transits with observatories like the *Spitzer Space Telescope (Spitzer)* can provide some information on atmospheric composition if the radii vary in bands where common molecules absorb. For example *Spitzer* observations at 3.6 μm should be dominated by CH_4 absorption and the 4.5 μm band by CO/CO_2 so that differential radii provide information on the carbon chemistry of the atmosphere.

Measuring the transit depth at many wavelengths (i.e. spectroscopically) creates a transmission spectrum which can be used to place even greater constraints on the chemical composition of the atmosphere. The magnitude of the change in planetary radius during transit due to molecular absorption is largely a function of the atmospheric scale height. As a result, ideal candidates for transmission spectroscopy have some combination of high equilibrium temperatures, small host stars, low surface gravity, and low mean molecular mass composition (hydrogen-dominated).

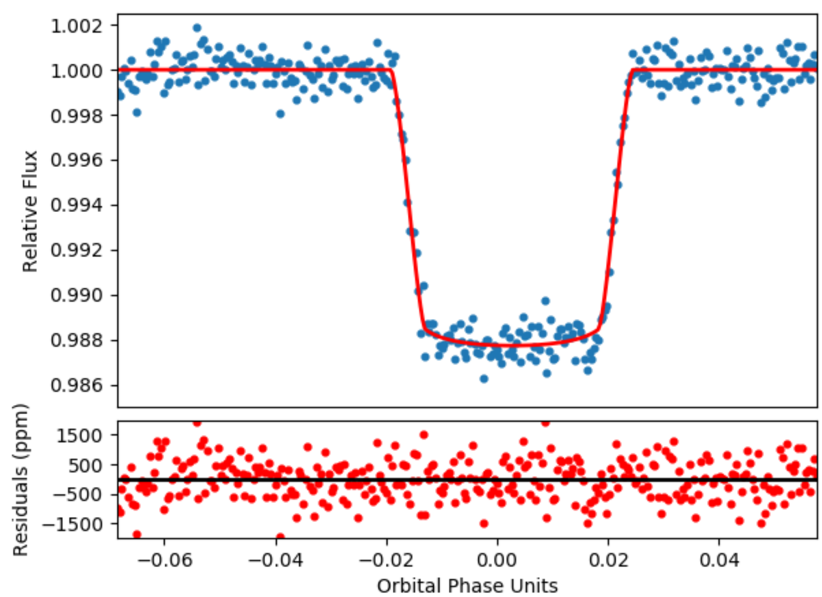

Figure 1.4 Photometric transit of the planet WASP-79b with the *Spitzer* space telescope at 4.5 μm. Photometric transits constrain planetary radius and other properties of the orbit. The transit depth is equivalent to $\left(\frac{R_p}{R_\star}\right)^2$ .Comparison of radii at multiple wavelengths can provide information about atmospheric absorbers. Figure by Kilpatrick and Jayaraman for Sotzen et al. (in prep).

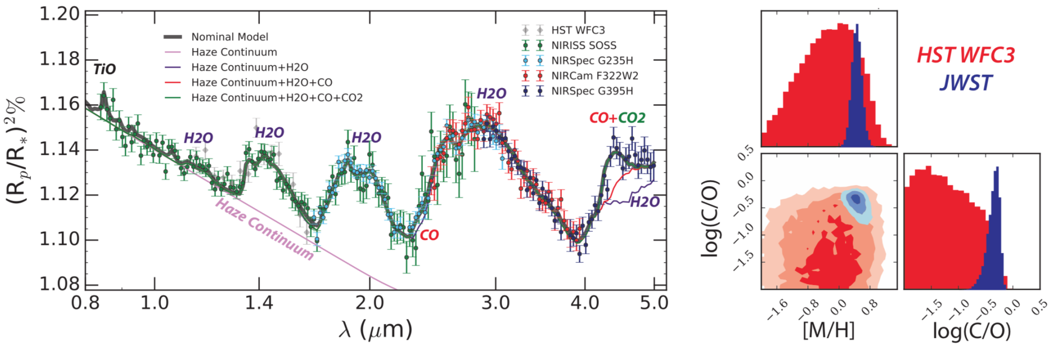

Figure 1.5 Simulated Transmission spectra of WASP-79 b showing the numerous molecular absorption features accessible by NIR observations with HST and JWST (Bean et al. 2018). The posterior distributions of the retrieved atmospheric metallicity and C/O ratio are shown at right. The red distributions are the results of data from currently available HST instruments and the blue adds in JWST observations.

Transmission spectroscopy is often conducted in the near infrared (NIR) where there are a number of rotational and vibrational transitions of molecules predicted to be in abundance in planetary atmospheres. Figure 1.5 shows an example of simulated transmission spectroscopy and the resultant constraints on chemical composition one could achieve with measurements from the *Hubble Space Telescope (HST)* and *James Webb Space Telescope (JWST)*. Note that in the example shown in the figure the magnitude of the changes in transit depth are on the order of a few percent of the continuum signal. This is typical of predictions for clear hot Jupiter atmospheres. Also note that absorption features increase $R_p/R_\star$ and appear as 'bumps' in the spectrum while scattering due to hazes (Mie Scattering) or molecular scattering of the atmosphere (Raleigh scattering) appear as a slope increasing at shorter wavelengths. Transit observations probe the limb of the planet at relatively low pressures as a result of the long optical path lengths required of the transit geometry.

Secondary Eclipse occurs when the planet passes behind the star in the reference frame of the observer. Here the flux, either reflected or emitted from the planet, is obscured by the star. Secondary eclipse depths are a measure of the flux of the planet to the flux of the star:

$$\frac{B_p(\lambda, T_{eq})}{B_\star(\lambda, T_\star)} \left(\frac{R_p}{R_\star}\right), \tag{1.15}$$

where $B_p(\lambda, T_{eq})$ and $B_\star(\lambda, T_\star)$ are the brightness flux of the planet and star respectively at a particular wavelength and effective temperature. Secondary eclipse signals of hot Jupiters vary strongly as a function of wavelength and are typically at least an order of magnitude smaller than transit signals. They are typically largest for hot Jupiters in the NIR near the peak of the planet's spectral energy density.

Photometric measures of secondary eclipses in the NIR are typically dominated by thermal emission rather than reflected light and provide information on the dayside temperature of the planet. Chapter 2 describes how measures of dayside brightness temperature in comparison to irradiation provide constraints on atmospheric circulation and albedo. Spectroscopic eclipses, similar to transit spectroscopy, can directly probe chemical composition via absorption or emission features. Molecules absorbing planetary flux at certain wavelengths will make $F_p/F_\star$ appear smaller while molecules emitting flux in an inverted atmosphere will increase $F_p/F_\star$ at particular wavelengths. Equally as import as detecting absorption/emission features is the manner in which eclipses measure the vertical temperature profile of the atmosphere. As optical opacity changes as a function of wavelength the pressure at which the eclipse observation probes also changes. This allows observers to reconstruct the temperature pressure profile of the atmosphere. Secondary Eclipses probe the hemispherically averaged dayside of the planet at relatively deeper pressures than transmission.

Full orbit phase curves are another observational technique for characterizing exoplanet atmospheres. During the planet's full orbit the observer will see the phases of the planet (similar to the phases of the moon). The change in flux as a function of phase can provide valuable information on the composition of the planet in multiple regions. In cases where the planet is tidally locked to the host star, very common in short period planets, phase is directly related to longitude. Observations of thermal emission over the full phase of tidally locked planets yield maps of the temperature distribution as a function of longitude. The distribution of thermal energy longitudinally provides insight into the relationship between circulatory winds, albedo, and radiation. A shift of the peak of radiation from the substellar point is indicative of circulatory winds and the amplitude of the phase curve signal is representative of the day-night temperature contrast.

Observing exoplanet atmospheres from multiple geometries is crucial because each probes a different region of the planet where temperatures accessed can vary by hundreds of Kelvin (Kataria et al. 2016) greatly affecting the regional chemistry. My research has employed a multi-faceted approach to the characterization of exoplanet atmospheres. I have utilized a number of observational techniques and theoretical frameworks to explore atmospheric composition and structure. I have placed an emphasis on ensuring robustness of scientific results by analyzing data with multiple methodologies and engaging diverse cross sections of the community in collaboration. In this dissertation I will review my implementation of multiple techniques and instruments to comprehensively study exoplanet atmospheres.

References

Agol, E., Cowan, N. B., Knutson, H. A., Deming, D., Steffen, J. H., Henry, G. W., & Charbonneau, D. 2010, ApJ, 721, 1861

Bean, J. L., Stevenson, K. B., Batalha, N. M., Berta-Thompson, Z., Kreidberg, L., Crouzet, N., Benneke, B., Line, M. R., Sing, D. K., Wakeford, H. R., Knutson, H. A., Kempton, E. M.-R., Désert, J.-M., Crossfield, I., Batalha, N. E., de Wit, J., Parmentier, V., Harrington, J., Moses, J. I., Lopez-Morales, M., Alam, M. K., Blecic, J., Bruno, G., Carter, A. L., Chapman, J. W., Decin, L., Dragomir, D., Evans, T. M., Fortney, J. J., Fraine, J. D., Gao, P., García Muñoz, A., Gibson, N. P., Goyal, J. M., Heng, K., Hu, R., Kendrew, S., Kilpatrick, B. M., Krick, J., Lagage, P.-O., Lendl, M., Louden, T., Madhusudhan, N., Mandell, A. M., Mansfield, M., May, E. M., Morello, G., Morley, C. V., Nikolov, N., Redfield, S., Roberts, J. E., Schlawin, E., Spake, J. J., Todorov, K. O., Tsiaras, A., Venot, O., Waalkes, W. C., Wheatley, P. J., Zellem, R. T., Angerhausen, D., Barrado, D., Carone, L., Casewell, S. L., Cubillos, P. E., Damiano, M., de Val-Borro, M., Drummond, B., Edwards, B., Endl, M., Espinoza, N., France, K., Gizis, J. E., Greene, T. P., Henning, T. K., Hong, Y., Ingalls, J. G., Iro, N., Irwin, P. G. J., Kataria, T., Lahuis, F., Leconte, J., Lillo-Box, J., Lines, S., Lothringer, J. D., Mancini, L., Marchis, F., Mayne, N., Palle, E., Rauscher, E., Roudier, G., Shkolnik, E. L., Southworth, J., Swain, M. R., Taylor, J., Teske, J., Tinetti, G., Tremblin, P., Tucker, G. S., van Boekel, R., Waldmann, I. P., Weaver, I. C., & Zingales, T. 2018, PASP, 130, 114402

Bryan, M. L., Knutson, H. A., Lee, E. J., Fulton, B. J., Batygin, K., Ngo, H., & Meshkat, T. 2019, AJ, 157, 52

Charbonneau, D., Brown, T. M., Latham, D. W., & Mayor, M. 2000, ApJ, 529, L45

Fulton, B. J., Petigura, E. A., Howard, A. W., Isaacson, H., Marcy, G. W., Cargile, P. A., Hebb, L., Weiss, L. M., Johnson, J. A., Morton, T. D., Sinukoff, E., Crossfield, I. J. M., & Hirsch, L. A. 2017, AJ, 154, 109

Howard, A. W., Marcy, G. W., Johnson, J. A., Fischer, D. A., Wright, J. T., Isaacson, H., Valenti, J. A., Anderson, J., Lin, D. N. C., & Ida, S. 2010, Science, 330, 653

Kataria, T., Sing, D. K., Lewis, N. K., Visscher, C., Showman, A. P., Fortney, J. J., & Marley, M. S. 2016, ApJ, 821, 9

Showman, A. P., Cho, J. Y.-K., & Menou, K. 2010, Atmospheric Circulation of Exoplanets, ed. S. Seager, 471–516

Showman, A. P., Fortney, J. J., Lian, Y., Marley, M. S., Freedman, R. S., Knutson, H. A., & Charbonneau, D. 2009, ApJ, 699, 564

Winn, J. N. 2010, arXiv e-prints, arXiv:1001.2010

Chapter 2

Secondary Eclipse Observations with the Spitzer Space Telescope

This Chapter is based on work performed with coauthors and previously published in the Astronomical Journal as Kilpatrick et al. (2017).

The purpose of this study was twofold:

- To evaluate the precision of results when using various models to correct *Spitzer* instrument systematics. At the time of publication, the problem of intrapixel variation in the warm *Spitzer* mission was well documented. There were a number of procedures and models developed for correcting the raw flux yet little cross comparison between methods was done to ensure convergence and evaluate their precision. A data challenge hosted by *Spitzer's* Infrared Processing and Analysis Center (IPAC) (Carey et al. 2015) tested many of the available methods on a common dataset. The results of that study were promising but were only a sample size of one. The question remained whether or not each methodology would be reliable across a diverse set of observations. The observations discussed here span different exposure times, length of observation, pointing positions and stability, and brightness.

- To place constraints on the albedo and circulation of hot Jupiter atmospheres. Photometric secondary eclipses provide information on the dynamics and albedo of the atmosphere. The effective temperature of the planet in comparison to the incident irradiation places constraints on how much energy was either scattered back into space or redistributed to the night side of the planet.

In the context of the entirety of the thesis, this work laid the foundation for being able to achieve the best precision possible from *Spitzer* observations. I developed pipelines for correcting the intrapixel variability with four different methods and became intimately familiar with the tendencies of *Spitzer* data. This skill set would be key to future work aimed at detecting small variations in the lightcurve.

2.1 Abstract

We measure the 4.5 μm thermal emission of five transiting hot Jupiters, WASP-13b, WASP-15b, WASP-16b, WASP-62b and HAT-P-22b using channel 2 of the Infrared Array Camera (IRAC) on the *Spitzer Space Telescope*. Significant intrapixel sensitivity variations in *Spitzer* IRAC data require careful correction in order to achieve precision on the order of several hundred parts per million (ppm) for the measurement of exoplanet secondary eclipses. We determine eclipse depths by first correcting the raw data using three independent data reduction methods. The Pixel Gain Map (PMAP), Nearest Neighbors (NNBR), and Pixel Level Decorrelation (PLD) each correct for the intrapixel sensitivity effect in *Spitzer* photometric time-series observations. The results from each methodology are compared against each other to establish if they reach a statistically equivalent result in every case and to evaluate their ability to minimize uncertainty in the measurement. We find that all three methods produce reliable results. For every planet examined here NNBR and PLD produce results that are in statistical agreement. However, the PMAP method appears to produce results in slight disagreement in cases where the stellar centroid is not kept consistently on the most well characterized area of the detector. We evaluate the ability of each method to reduce the scatter in the residuals as well as in the correlated noise in the corrected data. The NNBR and PLD methods consistently minimize both white and red noise levels and should be considered reliable and consistent. The planets in this study span equilibrium

Table 2.1. Observations

	WASP-13b	WASP-15b	WASP-16b	WASP-62b	HAT-P-22b
AOR	45675520	45675776	45674496	48680448	45674752
Date of Obs.(UT)	June 08, 2012	September 14, 2012	September 09, 2012	September 19, 2013	June 03, 2012
Frame Time (s)	0.4	2.0	2.0	2.0	0.4
Duration of Obs. (min)	469	495	277	444	371

temperatures from 1100 to 2000 K and have brightness temperatures that require either high albedo or efficient recirculation. However, it is possible that other processes such as clouds or disequilibrium chemistry may also be responsible for producing these brightness temperatures.

2.2 Introduction

The *Spitzer Space Telescope* has been the preeminent observatory used to obtain photometric light curves of transiting exoplanets in the infrared. The relative flux variations during a secondary eclipse (planet passing behind the star) provide insight into the planetary energy budget and atmospheric circulation. Hot Jupiters, Jupiter-sized planets less than 0.1 AU from their host stars, are valuable targets for such studies in the near infrared. The *Spitzer* Infrared Array Camera (IRAC) instrument has two channels well positioned to sample the peak of hot-Jupiter emission spectra. The decrease in relative flux during a secondary eclipse is representative of the planetary dayside emission. The magnitude of this signal is often on the order of several hundred to a few thousand parts per million (ppm). In its post cryogenic 'Warm Mission', *Spitzer* IRAC is capable of obtaining better than 100 ppm precision in time series observations (Ingalls et al. 2012). However, these IRAC observations are also affected by systematic and spatially correlated variations as the image centroid moves across a detector pixel. The intra-pixel sensitivity effect in the under-sampled camera can cause variations on the order of 10% with normal pointing jitter and movement (Ingalls et al. 2016). This movement is attributed to several factors but on timescales of the order of several hours is primarily due to jitter (high frequency and stochastic) and a heater cycling (wobble) that changes the alignment between the star tracker and optical axes by $\sim 0.15''$ over a 40 minute period (Grillmair et al. 2012).

There have been many methods used to remove this correlated noise effect (e.g. Reach et al. 2005; Charbonneau et al. 2008; Ballard et al. 2010), but the past several years have seen the development of a few novel methods that have been utilized in a number of recent *Spitzer* publications (e.g. Lewis et al. 2013; Deming et al. 2015; Stevenson et al. 2012; Ingalls et al. 2012; Gibson et al. 2012; Evans et al. 2015; Morello et al. 2015).

In this work we consider three of the more commonly used methods; the Infrared Processing and Analysis Center's (IPAC) provided Pixel Variation Gain Map (PMAP) (Ingalls et al. 2012), the Nearest Neighbor Method (NNBR) (Lewis et al. 2013), and Pixel Level Decorrelation (PLD) (Deming et al. 2015). Each of these methods has been independently tested and used to analyze various data sets. A recent IPAC Data Challenge (Ingalls et al. 2016) invited members of the community to employ these methods, and others, in the reduction of a set of multi-epoch eclipses of the planet XO-3b along with a set of synthetic data. The data challenge sought to show that the full range of reduction methodologies could provide accurate and consistent results over many observations of the same planet.

The work reported here continues the effort to validate that each method produces results that are in statistical agreement with each other by using measurements of five different planets. This approach will provide insight into how well each method performs in reducing correlated noise over a range of eclipse depths, observation times, cadence, and pointing stability. Note for comparison purposes that in the data challenge and in Krick et al. (2016) NNBR is referred to as Kernel Regression with Data and what we will later define as KMAP is referred to as Kernel Regression with Pixel Map.

2.3 Observations

The observations analyzed here are all part of Program ID 80016 (PI: J. Krick) and include the planets WASP-13b, WASP-15b, WASP-16b, WASP-62b and HAT-P-22b. Each planet was observed during one secondary eclipse by IRAC Channel 2 ($4.5\,\mu\mathrm{m}$ bandpass) (Fazio et al. 2004). The details of each Astronomical Observing Request (AOR) are displayed in Table 2.1. All of these observations were carried out in sub-array mode (32×32 pixels, 39" $\times$ 39") with a 30 minute peak-up observation preceding them. The use of a peak up observation allows the instrument to stabilize the image on the detector 'sweet spot' and decreases the likelihood of a ramp in the data (Ingalls et al. 2012).

2.4 Methods

In each case we began with Basic Calibrated Data (BCD) available on the Spitzer Heritage Archive. Each BCD file contains a cube of 64 frames of 64×64 pixels. Each frame was corrected by two separate methods for bad pixels (pixels with values outside of a pre-defined range, which we take to be $(-100, 10, 000)$) or NaN values. The PMAP routine defines the area of an annulus with a 3 pixel inner radius and 7 pixel outer radius centered on the stellar centroid as the background. The PMAP photometry routine ignores bad pixels in the background when calculating the sky contribution but will not produce a flux value from aperture photometry if a bad pixel is found within the 3 pixel aperture radius.

NNBR and PLD employ a slightly different photometry routine which replaces any bad pixels or NaN values outside of the aperture with the median background value. The background is defined as any point outside a 10 pixel radius from the stellar centroid. All points in the background area were sorted, clipped at 3σ three times to remove outliers, then fit with a Gaussian to determine the sky value and uncertainty in the background subtraction.

Time-series photometry data were filtered to remove outliers by iteratively clipping values outside 3σ of the median of the nearest 50 points temporally. Less than 1% of the data was removed by this filtering. Each eclipse fit was based on the model of Mandel & Agol (2002) for a uniform occultation. *Spitzer* IRAC data is known to have an exponential ramp in flux over the first 30–60 minutes of observing (e.g. Lewis et al. 2013; Knutson et al. 2012); however the peak-up technique has alleviated this problem to some extent. As a precaution, each data set was trimmed at 10, 20, and 30 minutes from the beginning to see if this resulted in a decrease in the standard deviation of the normalized residuals (SDNR). In each case we determined that trimming was not necessary. Aside from these commonalities, the particulars of each method are described in the following sections.

2.4.1 Pixel Gain Map

The PMAP method was applied using the tools available from the IRAC program website [1]. The instructions provided were followed closely in an attempt to produce consistent results. BCD files from the IRAC Data Reduction Pipeline were downloaded and analyzed as follows. The IDL `box_centroider.pro` routine [1] calculates the centroid (x,y) position as shown in Ingalls et al. (2012):

$$x_{\text{cen}} = \frac{\sum_{j,k}(I_{jk}j)}{\sum_{j,k} I_{jk}}; \qquad y_{\text{cen}} = \frac{\sum_{j,k}(I_{jk}k)}{\sum_{j,k} I_{jk}}. \tag{2.1}$$

Here, I_{jk} is the surface brightness of pixel (j,k), where the center of bottom left pixel of the subarray is position (0,0) (Ingalls et al. 2012). In practice, we confine the centroiding to a 7 $\times$ 7 pixel box with the pixel containing the peak flux at the center. Based upon the recommendations from IPAC, we used a fixed radius circular aperture of 3 pixels. The IDL routine `aper.pro` was used to integrate over a circular area of square pixels. The filtered flux along with the corresponding x and y positions of the stellar centroid were passed to the `iracpc_pmap_corr.pro` IDL routine in order to calculate the corrected flux values. The derivation of the photometric gain maps is discussed in detail in Ingalls et al. (2012). The peak of pixel sensitivity for channel 2 corresponds to a position of (15.12, 15.09). The sweet spot is a 0.5×0.5 pixel box centered at the position of peak sensitivity.

[1] http://irachpp.spitzer.caltech.edu/page/contrib

A non-variable calibration target was observed at various offsets from the peak in order to create the grid of relative flux values. The ch2 gain map has 409, 539 photometry points in it, 90% of which are within the sweet spot. Each point on the grid is the result of a combination of a number of observational points. This number, the occupation number, can be used to assess the reliability of any point on the grid. Figure 2.1 shows occupation number contours. Areas outside of the contours do not have a high enough occupation number to be considered accurate.

Once the flux values were corrected, a Levenberg-Marquardt (LM) fitting routine (Markwardt 2009) determined the best fit for eclipse depth, center of eclipse, nd stellar flux baseline using the Mandel & Agol (2002) model for a uniform occultation. Values for $\frac{a}{R_\star}$, $\frac{R_p}{R_\star}$, and inclination (listed in Table 2.2), from the exoplanets.org database (Han et al. 2014) were input as constants in the calculation of the eclipse model. The results of the LM minimization were used to seed a multi-chain Markov-Chain Monte Carlo (MCMC) simulation to determine the best fit and uncertainties for the eclipse depth and time of eclipse parameters.

In order to take correlated "red" noise into account in our uncertainties we binned the residuals from the LM fit in bin sizes of 2.0 s intervals up to 90 min and calculated the $\beta_{\rm red}$ coefficient as defined in Gillon et al. (2010). The maximum $\beta_{\rm red}$ value over the entire 90 min range was used as the worst case scenario. The uncertainty of each photometric point, as determined by the SDNR of the unbinned time-series, was multiplied by the $\beta_{\rm red}$ factor before being passed to the MCMC to account for time-correlated noise. The priors for each parameter in the MCMC were based on a normal distribution centered at the LM result with a width determined by the uncertainty in the LM result.

We employ a Metropolis-Hasting algorithm within the Gibbs sampler MCMC (Ford 2005). There were two free parameters, depth and center of eclipse. Four independent chains were initiated from four unique and randomly selected starting points, run for a minimum of 10^4 steps and then tested for Gelman-Rubin convergence (Gelman & Rubin 1992). The algorithm sought to minimize χ^2. Step size was adjusted to produce $\sim$ 40% acceptance rate. The first 20% of the steps

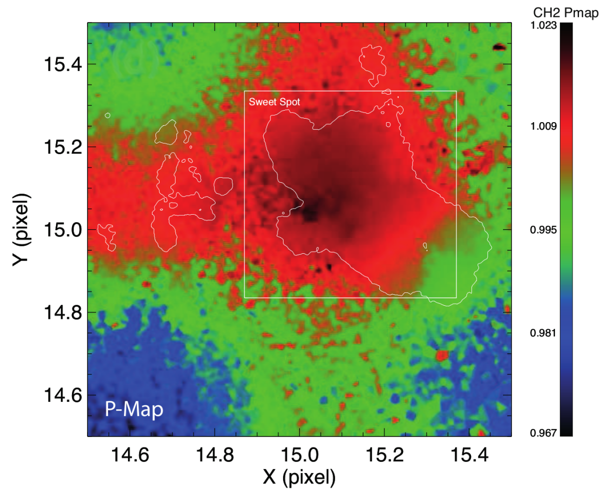

Figure 2.1 This plot from Ingalls et al. (2012) shows how the pixel responds as a function of stellar centroid position. The sweet spot is a 0.5×0.5 pixel area outlined by the white box in the figure. The color map shows the pixel response, or gain, at each location on the pixel. The areas enclosed by the contour lines are areas with an occupation number of 20 or greater. For the most reliable results the observation should seek to keep the stellar centroid in an area that is both highly responsive and well characterized (i.e. has a high occupation number).

were discarded to remove any burn in period and the rest were kept to create a histogram of results for each parameter. After inspecting each histogram for evidence of asymmetry; we determined that symmetric uncertainty would be appropriate. We find the best fit Gaussian to the MCMC histogram and take the 1σ width of the Gaussian to be the 1σ uncertainty in the parameter.

2.4.2 Nearest Neighbors

Each data set was also corrected for intra-pixel sensitivity variations using the NNBR as applied to HAT-P-2b phase-curve observations in Lewis et al. (2013). Using this method we take the BCD files and calculate the centroid position of each exposure using a center of light method. The noise pixel parameter ($\tilde{\beta}$), defined by equation A2 of Lewis et al. (2013) as

$$\tilde{\beta} = \frac{\left(\sum P_i\right)^2}{\sum \left(P_i^2\right)}, \tag{2.2}$$

is calculated for each exposure. Circular aperture photometry is performed using fixed and variable aperture radii. Variable radius apertures were based on either multiplying $\tilde{\beta}$ by some scaling factor or adding/subtracting some constant from $\tilde{\beta}$. Each flux value i was linked with its 50 nearest neighbors j by distance:

$$r_{i,j} = \sqrt{a(x_i - x_j)^2 + b(y_j - y_i)^2 + c(\tilde{\beta}_j^{\frac{1}{2}} - \tilde{\beta}_i^{\frac{1}{2}})^2}. \tag{2.3}$$

Each nearest neighbor was weighted with a Gaussian smoothing kernel $K_i(j) =$

$$exp\left(-\frac{(x_j - x_i)^2}{2\sigma_{x,i}^2} - \frac{(y_j - y_i)^2}{2\sigma_{y,i}^2} - \frac{(\tilde{\beta}_j^{\frac{1}{2}} - \tilde{\beta}_i^{\frac{1}{2}})^2}{2\sigma_{\tilde{\beta}_j^{\frac{1}{2}},i}^2}\right), \tag{2.4}$$

where x and y are the stellar centroid locations on the detector and the three-dimensional widths of the smoothing kernel are controlled by the σ terms that adjust depending on the density of the nearest neighbors (see Lewis et al. (2013) for further details).

The corrected relative flux value for any photometric point F_i with centroid position (x_i, y_i) and uncorrected flux value $F_{0,i}$ then becomes

$$F_i = \frac{F_{0,i}}{W_i(x_i, y_i)}, \tag{2.5}$$

where

$$W_i(x_i, y_i) = \frac{\sum_j F_{0,j} K_i(j)}{\sum_j K_i(j)}. \tag{2.6}$$

W_i(x$_i$, y$_i$) is summed over the 50 nearest neighbors (those with the smallest $r_{i,j}$ values). Best fit parameters for each aperture were solved for using the same LM minimization routine as described in ssec: pmapsec. The fit from each aperture size, including both fixed and variable, was evaluated for goodness of fit by considering the SDNR and the maximum β_{red} factor over the same range as PMAP. The aperture which minimized both β_{red} and SDNR was chosen and sent to the four chain MCMC to fine tune parameter fits and determine uncertainties. Error on the data points used in

Table 2.2. Ephemerides

Parameter	WASP-13b	WASP-15b	WASP-16b	WASP-62b	HAT-P-22b
$T_\star$	5950±70	6300±100	5700±150	6230±80	5302±80
$M_\star$ (M_{Sun})	1.090±0.05	1.180±0.03	1.000±0.0.03	1.250±0.05	0.916±0.35
$R_\star$ (R_{Sun})	1.574±0.048	1.477±0.072	0.946±0.0.057	1.280±0.05	1.040±0.044
M_p (M_{Jup})	0.474±0.034	0.543±0.021	0.842±0.0.032	0.562±0.042	2.151±0.077
R_p (R_{Jup})	1.407±0.052	1.379±0.067	1.008±0.0.083	1.390±0.060	1.080±0.058
$R_p/R_\star$	0.0919±0.0126	0.0984±0.0114	0.1095±0.0228	0.1109±0.014	0.1063±0.06
log(g)	2.775±0.042	2.829±0.046	3.315±0.055	2.865±0.047	3.660±0.144
Period	$4.3530135 \pm 2.7 \times 10^{-6}$	$3.752100^{+9 \times 10^{-6}}_{-1.1 \times 10^{-5}}$	$3.118601 \pm 1.46 \times 10^{-5}$	$4.4119530 \pm 3 \times 10^{-6}$	$3.2122200 \pm 9 \times 10^{-6}$
i (°)	85.43±0.29	$85.96^{+0.29}_{-0.41}$	85.22±0.35	$88.30\ ^{+0.9}_{-0.6}$	$86.90\ ^{+0.6}_{-0.5}$
msin i	0.472±0.034	0.541±0.021	0.839±0.032	0.562±0.042	2.148±0.077
$a/R_\star$	7.35±0.26	7.29±0.38	9.52±0.57	9.55±0.41	8.58±0.39
T_c [a]	55575.5136±0.00160	$54584.69819^{+0.00021}_{-0.0002}$	$54584.42878^{+0.00035}_{-0.00025}$	55855.39195 ±0.00027	54930.22001±0.00025
T_{14} (d)[a]	$0.1693^{+0.00108}_{-0.00133}$	0.1813±0.0013	0.0800±0.0018	0.1588±0.0014	0.1196±0.0014

[a] T_{14} is the total transit or eclipse duration.

the MCMC are equivalent to the SDNR multiplied by the $\beta_{\rm red}$ factor. The aperture type and radius (pixels) chosen for each planet are as follows: Var. 1.98, Fixed 2.45, Var. 2.70, Var. 2.88, Fixed 2.00 for WASP-13b, WASP-15b, WASP-16b, WASP-62b, and HAT-P-22b respectively. In cases where a variable aperture was used, the radius presented is the mean radius over the entire data set. MCMC analysis as described in ssec: pmapsec was used to establish uncertainty in the parameter results. In this case there are still only the same two free parameters, however, it is important to note that the correction applied to the raw data (the nearest neighbor map) is dependent upon these two parameters and recalculated at each step in the MCMC. Conversely the PMAP is independent of choices of eclipse depth and center.

2.4.3 Pixel Level Decorrelation

Using the PLD method of Deming et al. (2015), we apply an array of both fixed and variable circular apertures (as a function of $\tilde{\beta}$) to calculate photometric flux values from BCD data. The array of 3×3 pixels centered on the stellar centroid were saved and normalized so that at any time step their sum was unity thus removing any astrophysical signal. PLD assumes that the total flux observed can be broken down into a linear equation:

$$\Delta S^t = \sum_{i=1}^{n} c_i \hat{P}_i^t + DE(t) + ft + gt^2 + h, \tag{2.7}$$

where the pixel value of each of the 3×3 saved pixels is multiplied by some coefficient ($c_i \hat{P}_i^t$) and summed along with the eclipse model ($DE(t)$)and a time dependent 'ramp' ($ft + gt^2$). We introduce the eclipse through the Mandel & Agol (2002) model. This is the $E(t)$ term in the equation, and the free parameter D is the eclipse depth. This model component is then normalized by

$$\mathrm{model} = (\mathrm{model} - 1.0)/(1.0 - \min(\mathrm{model})). \tag{2.8}$$

The result is a light curve that is zero out of eclipse and -1 in eclipse. The problem is then reduced to solving the linear equation (Equation 4.4) using matrix inversion.

A regression routine solves the equation for the coefficients over an array of several hundred different values for the center of eclipse. The position of the center of eclipse which produces the smallest χ^2 value is kept as the solution for the center of eclipse.

One of the key components to the PLD method, in its attempt to reduce red noise, is to bin the data over various time scales and to find a solution at each binning. The solution found at each binning is then applied to the full set of unbinned data and evaluated for goodness of fit by determining the SDNR and maximum β_{red}. The fit which minimizes these noise components is selected as the best fit for that aperture. This process is repeated over each aperture size until a best fit is found for each.

Once the best fit for each aperture is found we follow the broadband solution method outlined in Deming et al. (2015). Each set of residuals is binned at various timescales up to ingress/egress timescales. The logarithm of the standard deviation of the residuals at each bin size is plotted against the logarithm of the bin size in time (s). A line of slope -0.5 passing through the log of the unbinned SDNR is used as the theoretical solution. The aperture that minimizes the χ^2 with the theoretical model is chosen as the best fit and sent to a MCMC to fine tune the solution and establish the uncertainties. The β_{red} coefficient is again used as a multiplicative factor on the SDNR for the uncertainty in each time series data point in the MCMC. A similar MCMC algortithm as described in ssec: pmapsec is used here with 14 free parameters (nine pixel coefficients, depth and center of eclipse, two time coefficients, and offset).

2.5 Results

The secondary eclipse depth and time of the center of eclipse derived for each observation are shown in Table 2.3. These results are derived by fitting a Gaussian to the histogram of results from the MCMC chains, minus a 20% burn in period. Visual inspection of the histograms indicate no asymmetry, so we assume the uncertainty in each measurement to be symmetric and equivalent to the 1σ value of the Gaussian distribution. The brightness temperature for each planet was calculated using the methods of Seager (2010). The stellar properties used are shown in Table 2.2.

2.6 Discussion

2.6.1 Systematic Implications

As a primary goal, we sought to verify whether the application of each of these data analysis methods would produce statistically consistent results. As shown in Table 2.3 and the plots in Figure 2.5, this is generally true. In all cases the NNBR and PLD methods agree to within 1σ uncertainty. In all but two cases PMAP also agrees to within 1σ uncertainty. The PMAP is reliant on pointing stability to keep the image on the well characterized sweet spot. Examination of the centroid positions of these discrepant observations suggest that the image was either not on the most well characterized part of the detector and/or had significant y drift in comparison to other observations. The plots in Figure 2.3 show the stellar centroid positions for each observation.

It is also worth noting that both of the data sets where PMAP did not match the NNBR and PLD reductions at the one sigma level utilized 0.4 s exposure times in contrast with the others that

Table 2.3. Results

Parameter	WASP-13b	WASP-15b	WASP-16b	WASP-62b	HAT-P-22b
PMAP Depth (ppm)	570±155	932±230	1010±149	1025±172	1466±120
NNBR Depth (ppm)	977±260	954±221	1060±222	761±312	1018±88
$NNBR_{\rm fixed}$ Depth (ppm)	1027±221	981±142	1131±118	874±156	1003±106
PLD Depth (ppm)	1261±123	832±179	1075±265	882±95	1120±91
$PLD_{\rm fixed}$ Depth (ppm)	1232±123	841±217	1099±233	948±103	1178±77
PMAP T_c [a]	1086.9964±0.0106	1184.9675±0.0139	1179.5994±0.0056	1554.7008±0.0078	1081.8057±0.0029
NNBR T_c [a]	1086.9977±0.0093	1184.9644±0.0063	1179.6017±0.0039	1554.6958±0.0080	1081.8041±0.0010
$NNBR_{\rm fixed}$ T_c [a]	1086.9954±0.0110	1184.9648±0.0060	1179.6001±0.0032	1554.6964±0.0060	1081.8037±0.0033
PLD T_c [a]	1086.9958±0.0022	1184.9714±0.0066	1179.6007±0.0055	1554.6992±0.0029	1081.8049±0.0013
$PLD_{\rm fixed}$ T_c [a]	1086.9963±0.0018	1184.9704±0.0063	1179.6001±0.0062	1554.6992±0.0029	1081.8044±0.0011
PMAP $T_B^{\circ} K$	1253.0±123.7	1485.04±151.0	1113.65 ±54.3	1393.4±92	1518.9±52.1
NNBR $T_B^{\circ} K$	1581.7±151.0	1499.42±144	1131.71±79.4	1245.4±184.5	1313.9±42.8
PLD $T_B^{\circ} K$	1732.6±77.4	1418.30±121.6	1137.1±94.3	1315.1±53.4	1362.7±42.9
Photon Noise Limit	0.0098	0.0057	0.0055	0.0041	0.0056
PMAP σ_w	0.0144	0.0069	0.0067	0.0048	0.0076
NNBR σ_w	0.0122	0.0063	0.0063	0.0045	0.0066
PLD σ_w	0.0125	0.0061	0.0061	0.0045	0.0066
PMAP $\beta_{\rm red}$	1.269	2.457	1.183	2.299	2.554
NNBR $\beta_{\rm red}$	2.112	1.673	1.081	1.459	1.587
PLD $\beta_{\rm red}$	1.071	1.347	1.172	1.258	1.232
PMAP σ_r	0.00049	0.00046	0.00036	0.00058	0.00074
NNBR σ_r	0.00061	0.00046	0.00037	0.00036	0.00024
PLD σ_r	0.00044	0.00039	0.00020	0.00036	0.00023

[a] We list all center of eclipse times in BJD_UTC-2.455E6 for consistency with other studies; to convert to BJD_TT add 66.184 s.

Table 2.4. Secondary Eclipse Depth Results Using KMAP

Planet	Eclipse Depth (ppm)	SDNR	$\beta_{\rm red}$	Aperture Radius (pixels)
WASP-13b	798 ± 193	0.0127	1.64	2.25
WASP-15b	1110 ± 216	0.0066	2.36	2.50
WASP-16b	1004 ± 128	0.0062	1.06	2.00
WASP-62b	1279 ± 110	0.0046	1.58	2.50
HAT-P-22b	999 ± 99	0.0069	1.62	2.50

used 2.0 s exposure times. It is entirely possible that this is purely coincidental, however, further investigation into differences in PMAP performance between targets of different brightness may be worthwhile. Inspection of the centroid position plots in Figure 2.3 suggest that the degrading performance efficiency with PMAP is more likely due to the drift in the stellar centroid.

The same team that developed PMAP has been recently employed a modification to their correction method that would utilize a kernel regression to create a calibration map (similar to NNBR) rather than the pre-gridded gain map (Krick et al. 2016). We applied this new Kernel Regression with Pixel Map (KMAP), to all of our targets as another means of comparison. Each data set was corrected using KMAP with an array of fixed aperture sizes [2.00, 2.25, 2.50, 2.75, 3.00]. Similar to previous analyses, we chose the photometry that produced the fit which minimized the white and red noise. In cases where stellar centroid is stable on the sweet spot, we find that results are not significantly different from the original PMAP results. However, the uncertainty in each result is reduced through improvements in both white and red noise. When we applied KMAP to the two cases where PMAP results were not within 1σ of NNBR and PLD we find that KMAP results are in close statistical agreement with PLD and NNBR ($< 1\sigma$). Results are shown in Table 2.4.

We also aimed to determine which methodologies produced the least amount of uncertainty in the eclipse depth and center of eclipse times. In order to facilitate this evaluation we determine the white (σ_w) and red (σ_r) components of the noise as described in Gillon et al. (2008) for comparison. The white noise component is simply a measure of the scatter in the residuals after applying the best fit to the corrected data. We can benchmark the white noise against the photon noise limit, and we can expect to achieve precision of approximately 1.3 times the photon noise limit using PMAP[2]. We find that the SDNR is, on average, 1.28, 1.15, and 1.15 times the photon noise limit for PMAP, NNBR, and PLD respectively. A cursory examination of the uncertainty associated with each eclipse depth in Figure 2.2 may lead one to believe that PMAP far out performed NNBR in limiting the scatter in the residuals. However, this evidence would be counter to the σ_w values

[2]http://irsa.ipac.caltech.edu/data/SPITZER/docs/irac/warmimgcharacteristics/

which suggest that NNBR does significantly better than PMAP at reducing uncertainty. Despite this, results from the MCMC still suggested that the NNBR results had a larger uncertainty. What we find is that in the PMAP method the gain map itself is a fixed value map assumed to be correct (i.e. have no uncertainty) while the NNBR 'map' is an additional degree of freedom, recalculated at every iteration of the MCMC. The pixel gain map does have an uncertainty $\sigma_P(x, y)$ as defined in Ingalls et al. (2012), however, the correction routine provided by IPAC does not use the uncertainty in the map to scale the error in the corrected data. The PMAP uncertainties given by the MCMC are underestimated as a result of this failure to propagate uncertainty forward from the gain map itself. To verify, we fixed the NNBR map values after the LM fitting and passed it to the MCMC as a fixed parameter. This produced uncertainties substantially smaller than when it is allowed to vary and substantially smaller than the PMAP uncertainty (shown in Table 2.3 denoted with the subscript 'fixed'). We performed a similar test of PLD by fixing the coefficients of the pixel values (c_i) when passing to the MCMC rather than allowing the MCMC to treat them as free parameters. This did not have a significant effect on the PLD results. The uncertainties associated with NNBR and PLD are thought to be accurate and conservative estimates while the uncertainties of PMAP measurements are, perhaps, underestimated.

Another important measure of how an analysis method succeeds in reducing noise in *Spitzer* time series data is how it reduces the correlated (red) noise. As previously discussed in Section 4.2 the source of the intrapixel sensitivity variation, the primary source of correlated noise in IRAC data, is the coupling between intrapixel gain variations and spacecraft pointing fluctuations. A full correction for the effect would produce corrected data absent of any spatially correlated periodicity. Figure 2.3 shows the periodograms of the normalized power in the residuals of both the corrected and uncorrected data. The heater cycle with a period of ∼40 minutes is the main source of spatially correlated noise. We see power removed from this frequency when applying corrections to the data. Any remaining power is on the order of random white noise and is not reduced if it is not spatially correlated. We measure the correlated noise remaining in the data after correction using both the

β_{red} coefficient and σ_{red} (Gillon et al. 2010). We find that the mean red noise component is 7.5%, 6.0%, and 4.9% of the magnitude of the white noise for PMAP, NNBR, and PLD respectively.

Computational efficiency is another factor worthy of consideration in comparing reduction methods. We will need to employ efficient methods to keep pace as the amount of data available increases. There are still a large number of observations to be analyzed, which were considered problematic before the development of the reduction techniques discussed in this work, and we anticipate another round of *Spitzer* observations in the coming year. Applying these methodologies to phase curves will require careful management of computational resources. Phase curve observations are several times longer than eclipse observations making cumbersome methodologies impractical.

PMAP is by far the quickest way to reduce *Spitzer* data and perform a fit. The photometry of a single eclipse observation using a single aperture can be extracted and fit in a matter of minutes with this method.

NNBR an PLD are very similar in their computational time. Both make use of multiple fixed and variable apertures, effectively performing the reduction several times over. PLD takes advantage of binning in order to speed up many of its calculations. Fitting and performing χ^2 analysis on binned data is far faster than working with the full data set. The use of DeLauney Triangles to sort the nearest neighbors in the NNBR method greatly improves efficiency (Lewis et al. 2013). The number of neighbors utilized has been determined based upon the cost of computational time weighed against the improvement in SDNR.

The KMAP is the most time consuming method at this stage. Both NNBR and KMAP recalculate a calibration map for each set of aperture photometry. This is the most time consuming task in the process. Further development of KMAP to find more efficient ways to perform the sorting and identification of the neighbors could lead to significant increases in computational efficiency.

The advantage to using either the PMAP or KMAP methods is that they are not self calibrated. Both NNBR and PLD rely solely on the data set at hand in calculating the corrections. This makes them susceptible to degeneracies between the variation due to intrapixel sensitivity and the astrophysical signal. Both PMAP and KMAP reference a grid of data points from a number of different calibration observations. PMAP simply interpolates to find a solution based on the closest grid points while KMAP uses a kernel regression of nearest neighbors.

2.6.2 Atmospheric Implications

These observations add five important data points to the exoplanets with measured infrared eclipses. To constrain the atmospheric properties of our planet sample within the larger hot Jupiter population, we have calculated the $4.5\,\mu$m brightness temperatures, T_B, corresponding to each method in Table 2.3. We then calculated a weighted-average T_B to constrain each planet's bond albedo and recirculation. We follow the methodology of Schwartz & Cowan (2015), who estimate a range of dayside effective temperatures (T_d) as

$$T_d = T_0(1 - A_B)^{\frac{1}{4}} \left(\frac{2}{3} - \frac{5}{12}\epsilon\right)^{\frac{1}{4}}. \tag{2.9}$$

Here $\mathrm{T_0}$ is the equilibrium temperature. $\mathrm{T_0} \equiv T_{\mathrm{eff}*}\sqrt{R_* a}$, where $T_{\mathrm{eff}*}$ is the stellar effective temperature, R_* is the stellar radius, and a is the orbital distance. Additionally, A_B is the albedo, and ϵ is the recirculation efficiency, where $\epsilon = 0$ implies no heat redistribution (i.e, no heat is transported from the dayside to the nightside), and $\epsilon = 1$ implies full recirculation. Because each brightness temperature is derived from a single eclipse, we can only constrain each planet's dayside temperature. Therefore, our solution is degenerate, and a range of albedos and recirculation efficiencies are consistent with our measurements. We perform a χ^2 analysis using a weighted-average of the brightness temperatures over a 101×101 grid of albedo and recirculation values as was done in Schwartz & Cowan (2015), and interpolate the median values. Our results are shown in Fig. 2.4. Furthermore, we compare our average T_B to upper and lower bounds of equilibrium temperatures in Table 2.5. The lower bound is calculated assuming an albedo of 0.4

Table 2.5. Comparison of the weighted-average brightness temperature (T_B) with upper and lower bounds represented by T_{eq1} and T_{eq2} all in °K. T_{eq1} is calculated as a lower bound using an albedo of 0.4 and uniform recirculation ($\epsilon = 1$), and T_{eq2} is an upper bound with albedo of 0 and ϵ of 0.

Planet	T_{eq1}	T_{eq2}	Avg. T_B
WASP-13b	1365.4	1983.1	1595.1±197.9
WASP-15b	1452.1	2108.41	1461.1±79.1
WASP-16b	1149.7	1669.3	1122.7 ±40.5
WASP-62b	1254.6	1821.6	1329.6±44.8
HAT-P-22b	1126.5	1635.6	1383.9±81.3

and full recirculation ($\epsilon = 1$) while the upper bound is calculated assuming an albedo of 0.0 and no recirculation ($\epsilon = 0$).

Comparing each map in Figure 2.4, we see that WASP-13b has the largest possible range of albedos and recirculation efficiencies; this is a result of its large uncertainty in weighted-average brightness temperature (Table 2.5). If we compare the weighted-average brightness temperatures to the upper and lower bound equilibrium temperatures, we see that the brightness temperatures for WASP-13b, WASP-15b, WASP-16b and WASP-62b are nearer in value to the lower bound equilibrium temperature, suggesting that those planets' atmospheres favor moderate albedo and high recirculation. All of these targets have orbital periods on the order of several days, and the $\frac{a}{R_*}$ values are greater than 7. Previous works have shown that planets in this regime are far more likely to have efficient recirculation (Perez-Becker & Showman 2013; Cowan & Agol 2011; Schwartz & Cowan 2015; Kammer et al. 2015).

The weighted-average brightness temperature of HAT-P-22b is more centered between the two extremes, suggesting the atmosphere may favor moderate albedo and less efficient recirculation.

Because the atmosphere is expected to be dominated by equatorial super-rotation at photospheric pressures (Showman et al. 2010), this might suggest other atmospheric processes at play on HAT-P-22b to inhibit recirculation. For example, it is possible that the infrared photosphere could be located at lower pressures than we expect, where radiative timescales are short compared to advective timescales. This could result from a low C/O ratio, which would imply an excess of CO and produce enhanced opacity at 4.5 m where CO has strong vibrational bands (Wong et al. 2016). Enhanced opacity could also arise if the atmospheric metallicity were greater than solar (e.g. Lewis et al. 2010; Kataria et al. 2015); this could also produce a dayside temperature inversion, which would additionally move the IR photosphere to lower pressures. Clearly, multi-wavelength eclipse and phase-curve measurements are needed for all five planets to further constrain the radiative, advective, and chemical processes taking place in their atmospheres.

2.7 Conclusions

We present secondary eclipse measurements for WASP-13b, WASP-15b, WASP-16b, WASP-62b, and HAT-P-22b in IRAC channel 2 at 4.5 μm. The reduction of *Spitzer* photometric observations requires accurate corrections to the intrapixel sensitivity effect in order to achieve the precision necessary to extract eclipse depths. The methodologies discussed in this work all are suitable approaches for achieving this goal. The computational efficiency and reliability with which PMAP is able to produce an eclipse fit makes it a valuable tool which researchers can use to quickly produce results. Each of the other methods considered potentially improve upon PMAP in producing a more precise measurement by their handling of both correlated and uncorrelated noise effects. However, this improvement comes at the cost of computational efficiency. PMAP proves quite reliable in cases where the peak up method of observation has been employed and the stellar centroid is well positioned on the detector. We have shown that methods that employ a nearest neighbor kernel handle cases where centroid position or drift may not be optimal. PLD may not be as well suited for data sets with large a amount of drift (Wong et al. 2016), however, the observations considered here are relatively short and stable in comparison to phase curves and PLD performed quite well. Both the PLD and NNBR methods consistently minimized the correlated noise in the corrected data.

We find that the brightness temperatures derived for WASP-13, WASP-15, WASP-16, and WASP-62 from our measured eclipse depths place them in a regime requiring either high albedo or efficient recirculation. While it is possible that these these planets have a higher albedo than previously observed planets, we suggest that there are a myriad of other physical processes not considered in a simple albedo-recirculation model that would produce similar results. HAT-P-22b occupies an area of phase where moderate albedo (0.4) and much less efficient recirculation would produce the measured brightness temperature.

2.8 Acknowledgments

BMK acknowledges Brown University for its financial support of his contributions to this work. This work is based on observations made with the *Spitzer Space Telescope*, which is operated by the Jet Propulsion Laboratory, California Institute of Technology under a contract with NASA. We also acknowledge that part of this work was completed at the Space Telescope Science Institute (STScI) operated by AURA, Inc. This research has made use of the Exoplanet Orbit Database and the Exoplanet Data Explorer at exoplanets.org.

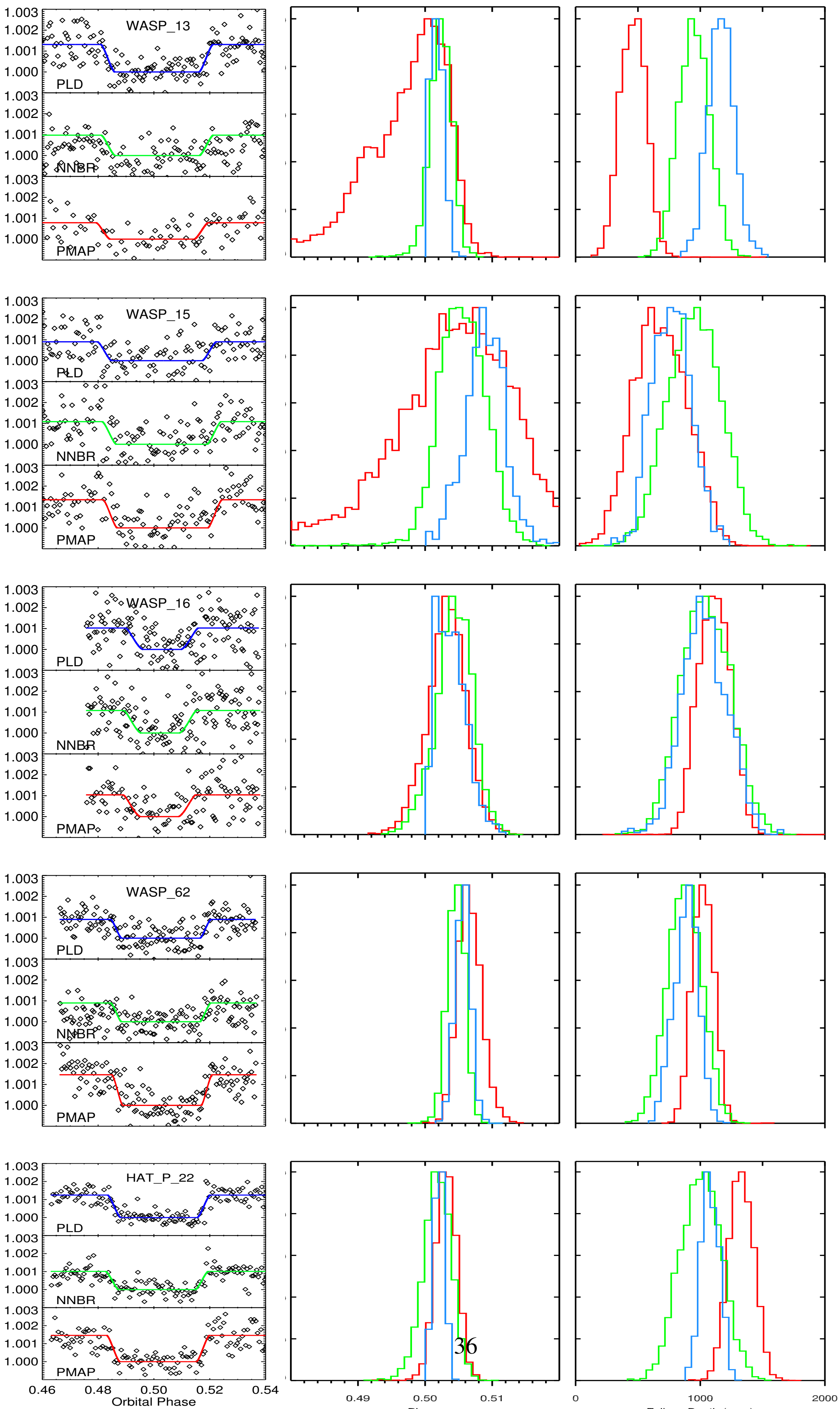
WASP_13
PLD
NNBR
PMAP
WASP_15
WASP_16
WASP_62
HAT_P_22
1.003
1.002
1.001
1.000
0.46
0.48
0.50
0.52
0.54
Orbital Phase
0.49
0.50
0.51
Phase
0
1000
2000
Eclipse Depth (ppm)

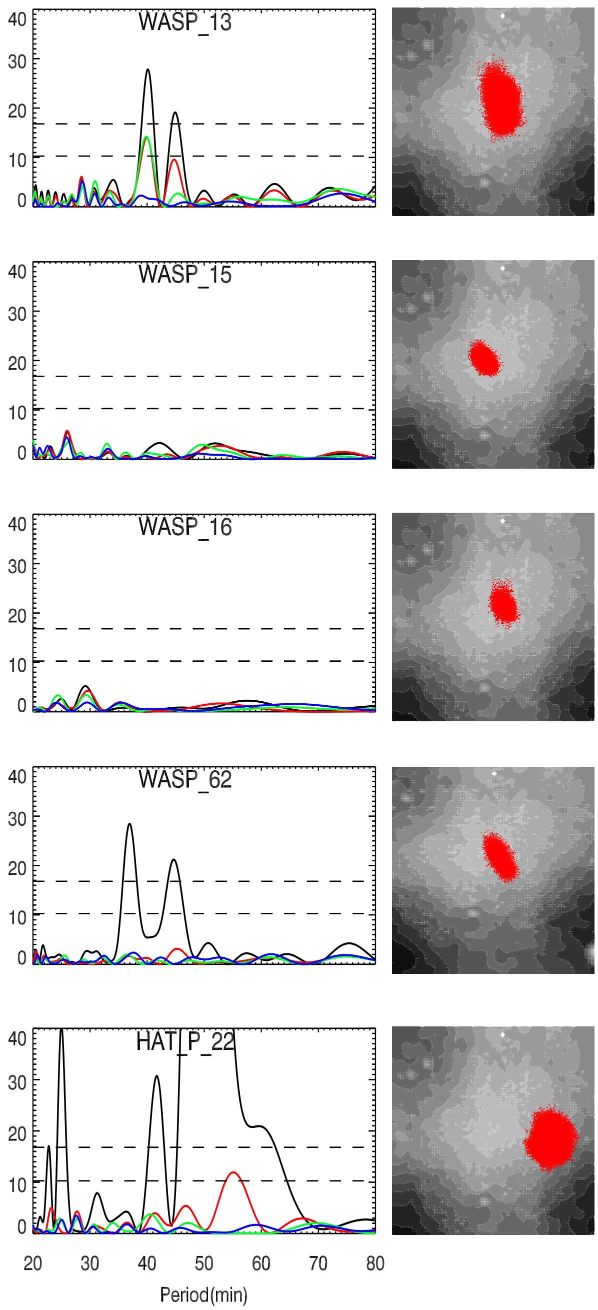

Figure 2.3 LEFT: Periodograms of the normalized power in the residuals of the uncorrected data (black), along with the periodogram of the residuals from fitting corrected data for each method (PMAP-red, NNBR-green, PLD-blue). Significance levels 0.5 and 0.001 are shown as horizontal dashed lines. RIGHT: Positions of the stellar centroid overlaid on a gray scale image of the detector sweet spot as shown in Figure 1. The period of the heater cycling responsible for most of the y drift is on the order of 40 minutes. Significant spikes in power are seen at this frequency in all but the most well positioned observations.

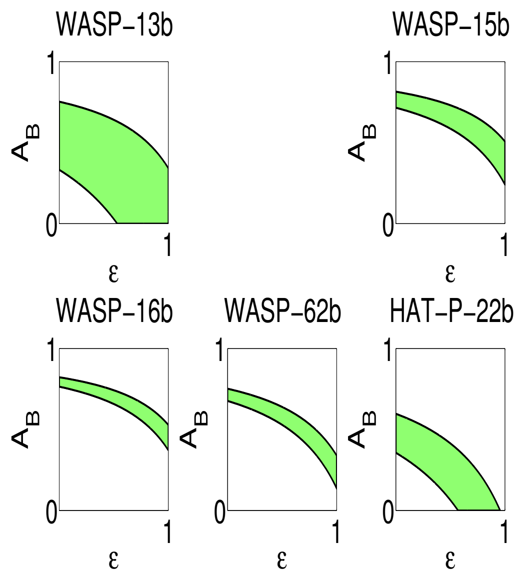

Figure 2.4 Possible albedo (A_B) and recirculation efficiency (ϵ) values that produce a dayside brightness temperature within the uncertainties of the weighted average brightness temperatures derived from our *Spitzer* $4.5\,\mu$m eclipses. Calculations were performed using the methodology of Schwartz & Cowan (2015). Both A_B and ϵ range from 0 to 1. 0 A_B is total reflection and 1 full absorption. ϵ of 0 is no recirculation and ϵ of 1 is uniform redistribution.

References

Ballard, S., Charbonneau, D., Deming, D., Knutson, H. A., Christiansen, J. L., Holman, M. J., Fabrycky, D., Seager, S., & A'Hearn, M. F. 2010, PASP, 122, 1341

Carey, S. J., Krick, J., & Ingalls, J. 2015, in AAS/Division for Extreme Solar Systems Abstracts, Vol. 3, AAS/Division for Extreme Solar Systems Abstracts, 110.08

Charbonneau, D., Knutson, H. A., Barman, T., Allen, L. E., Mayor, M., Megeath, S. T., Queloz, D., & Udry, S. 2008, ApJ, 686, 1341

Cowan, N. B. & Agol, E. 2011, ApJ, 729, 54

Deming, D., Knutson, H., Kammer, J., Fulton, B. J., Ingalls, J., Carey, S., Burrows, A., Fortney, J. J., Todorov, K., Agol, E., Cowan, N., Desert, J.-M., Fraine, J., Langton, J., Morley, C., & Showman, A. P. 2015, ApJ, 805, 132

Evans, T. M., Aigrain, S., Gibson, N., Barstow, J. K., Amundsen, D. S., Tremblin, P., & Mourier, P. 2015, MNRAS, 451, 680

Fazio, G. G., Hora, J. L., Allen, L. E., Ashby, M. L. N., Barmby, P., Deutsch, L. K., Huang, J.-S., Kleiner, S., Marengo, M., Megeath, S. T., Melnick, G. J., Pahre, M. A., Patten, B. M., Polizotti, J., Smith, H. A., Taylor, R. S., Wang, Z., Willner, S. P., Hoffmann, W. F., Pipher, J. L., Forrest, W. J., McMurty, C. W., McCreight, C. R., McKelvey, M. E., McMurray, R. E., Koch, D. G., Moseley, S. H., Arendt, R. G., Mentzell, J. E., Marx, C. T., Losch, P., Mayman, P., Eichhorn, W., Krebs, D., Jhabvala, M., Gezari, D. Y., Fixsen, D. J., Flores, J., Shakoorzadeh, K., Jungo, R., Hakun, C., Workman, L., Karpati, G., Kichak, R., Whitley, R., Mann, S., Tollestrup, E. V., Eisenhardt, P., Stern, D., Gorjian, V., Bhattacharya, B., Carey, S., Nelson, B. O., Glaccum, W. J., Lacy, M., Lowrance, P. J., Laine, S., Reach, W. T., Stauffer, J. A., Surace, J. A., Wilson, G., Wright, E. L., Hoffman, A., Domingo, G., & Cohen, M. 2004, ApJS, 154, 10

Ford, E. B. 2005, AJ, 129, 1706

Gelman, A. & Rubin, D. B. 1992, Statistical science, 457

Gibson, N. P., Aigrain, S., Pont, F., Sing, D. K., Désert, J.-M., Evans, T. M., Henry, G., Husnoo, N., & Knutson, H. 2012, MNRAS, 422, 753

Gillon, M., Anderson, D. R., Demory, B., Wilson, D. M., Hellier, C., Queloz, D., & Waelkens, C. 2008, ArXiv e-prints

Gillon, M., Lanotte, A., Barman, T., Miller, N., Demory, B.-O., Deleuil, M., Montalbán, J., Bouchy, F., Cameron, A. C., Deeg, H., et al. 2010, Astronomy & Astrophysics, 511, A3

Grillmair, C. J., Carey, S. J., Stauffer, J. R., Fisher, M. E., Olds, R., Ingalls, J. G., Krick, J. E., Glaccum, W. J., Laine, S., Lowrance, P. J., & Surace, J. A. 2012, in Proc. SPIE, Vol. 8448, Observatory Operations: Strategies, Processes, and Systems IV, 84481I

Han, E., Wang, S. X., Wright, J. T., Feng, Y. K., Zhao, M., Fakhouri, O., Brown, J. I., & Hancock, C. 2014, PASP, 126, 827

Ingalls, J. G., Krick, J. E., Carey, S. J., Laine, S., Surace, J. A., Glaccum, W. J., Grillmair, C. C., & Lowrance, P. J. 2012, in SPIE Astronomical Telescopes+ Instrumentation, International Society for Optics and Photonics, 84421Y–84421Y

Ingalls, J. G., Krick, J. E., Carey, S. J., Stauffer, J. R., Lowrance, P. J., Grillmair, C. J., Buzasi, D., Deming, D., Diamond-Lowe, H., Evans, T. M., Morello, G., Stevenson, K. B., Wong, I., Capak, P., Glaccum, W., Laine, S., Surace, J., & Storrie-Lombardi, L. 2016, AJ, 152, 44

Kammer, J. A., Knutson, H. A., Line, M. R., Fortney, J. J., Deming, D., Burrows, A., Cowan, N. B., Triaud, A. H. M. J., Agol, E., Desert, J.-M., Fulton, B. J., Howard, A. W., Laughlin, G. P., Lewis, N. K., Morley, C. V., Moses, J. I., Showman, A. P., & Todorov, K. O. 2015, ApJ, 810, 118

Kilpatrick, B. M., Lewis, N. K., Kataria, T., Deming, D., Ingalls, J. G., Krick, J. E., & Tucker, G. S. 2017, AJ, 153, 22

Knutson, H. A., Lewis, N., Fortney, J. J., Burrows, A., Showman, A. P., Cowan, N. B., Agol, E., Aigrain, S., Charbonneau, D., Deming, D., Désert, J.-M., Henry, G. W., Langton, J., & Laughlin, G. 2012, ApJ, 754, 22

Krick, J. E., Ingalls, J., Carey, S., von Braun, K., Kane, S. R., Ciardi, D., Plavchan, P., Wong, I., & Lowrance, P. 2016, ApJ, 824, 27

Lewis, N. K., Knutson, H. A., Showman, A. P., Cowan, N. B., Laughlin, G., Burrows, A., Deming, D., Crepp, J. R., Mighell, K. J., Agol, E., Bakos, G. Á., Charbonneau, D., Désert, J.-M., Fischer, D. A., Fortney, J. J., Hartman, J. D., Hinkley, S., Howard, A. W., Johnson, J. A., Kao, M., Langton, J., & Marcy, G. W. 2013, ApJ, 766, 95

Mandel, K. & Agol, E. 2002, ApJ, 580, L171

Markwardt, C. B. 2009, in Astronomical Society of the Pacific Conference Series, Vol. 411, Astronomical Data Analysis Software and Systems XVIII, ed. D. A. Bohlender, D. Durand, & P. Dowler, 251

Morello, G., Waldmann, I. P., Tinetti, G., Howarth, I. D., Micela, G., & Allard, F. 2015, ApJ, 802, 117

Perez-Becker, D. & Showman, A. P. 2013, ApJ, 776, 134

Reach, W. T., Megeath, S. T., Cohen, M., Hora, J., Carey, S., Surace, J., Willner, S. P., Barmby, P., Wilson, G., Glaccum, W., Lowrance, P., Marengo, M., & Fazio, G. G. 2005, PASP, 117, 978

Schwartz, J. C. & Cowan, N. B. 2015, MNRAS, 449, 4192

Seager, S. 2010, Exoplanet Atmospheres: Physical Processes

Showman, A. P., Cho, J. Y.-K., & Menou, K. 2010, Atmospheric Circulation of Exoplanets, ed. S. Seager, 471–516

Stevenson, K. B., Harrington, J., Fortney, J. J., Loredo, T. J., Hardy, R. A., Nymeyer, S., Bowman, W. C., Cubillos, P., Bowman, M. O., & Hardin, M. 2012, ApJ, 754, 136

Wong, I., Knutson, H. A., Kataria, T., Lewis, N. K., Burrows, A., Fortney, J. J., Schwartz, J., Shporer, A., Agol, E., Cowan, N. B., Deming, D., Désert, J.-M., Fulton, B. J., Howard, A. W., Langton, J., Laughlin, G., Showman, A. P., & Todorov, K. 2016, ApJ, 823, 122

Chapter 3

Community Targets for JWST's Early Release Science Program: Evaluation of WASP-63b

This chapter was previously published as Kilpatrick et al. (2018). In this work I sought to expand my toolset to encompass spectrosocopic transits. Spectroscopic observations are far different from photometric in the way they are analyzed and interpreted.

The main scientific goal of this work was to support the Transiting Exoplanet Community Early Release Science (ERS) Program (Bean et al. 2018) in identifying a suitable target. The Transiting Exoplanet Community Early Release Science Program brought together the expertise of over 100 members (61 Investigators and 43 Collaborators) of the community to put forth a program to accelerate the acquisition and diffusion of technical expertise for transiting exoplanet observations with *JWST*. The product of this collaborative effort by the transiting exoplanet community was the development of a single ERS program that is both comprehensive and efficient. The program was the highest rated program of all ERS submissions and was awarded 78 of the 500 hours allocated to ERS observations.

The program includes a panchromatic near-infrared (NIR, 0.6 – 5.2 μm) spectroscopic transmission observation of a close-in giant planet (i.e. hot Jupiter) to demonstrate *JWST's* ability to obtain precise composition measurements for transiting planets. Transmission spectroscopy is a proven technique for composition determinations, and the implemented instrument modes will be the workhorses for observations of planets ranging from hot giants to temperate terrestrials.

The community ERS program has been designed to include the necessary wavelength coverage to cross-compare and validate the three NIR instruments (NIRSpec, NIRCam, and NIRISS), and thus establish the best strategy for obtaining these measurements in future cycles.

It was necessary to identify a target, or set of targets, that would ensure the success of such a large program. Consequently, a working group was formed with the objective to perform a comprehensive search through all existing *HST* observations of potential targets to identify the best 'community' targets for the ERS program. The targets must have visibility windows such that one or more targets will be available regardless of what time of year the ERS program is conducted. Also, a planet with a relatively short orbital period is necessary to complete observations in all instrument modes and wavelength regions within a reasonable time frame (< 3 months) and within the number of awarded hours of *JWST* time. The spectroscopic light curve signal-to-noise (S/N) ratio benefits from having a bright star, while a quiet host star (as determined by its $\log R'_{HK}$ value) minimizes confusion between the desired signal and non-Gaussian, time-correlated astrophysical variations. Finally, it is important that the selected community target has measurable and identifiable features within its transmission spectrum. In order to effectively characterize exoplanet atmospheres with *JWST* we **must** determine the optimal instrument resolutions and wavelength regions for abundance retrieval studies. A flat spectrum would not meet this need.

Here we present the analysis of one of the targets that met initial criteria to warrant further study with *HST* to determine if it had observable spectroscopic features. We discuss the finding of a muted water feature and the retrieved chemical compositions.

This study is unique in that it engaged a large number of, often competing, members of the community to work together to compare methodologies. It laid the groundwork for future collaborative exercises such as data challenges in preparation for *JWST* observations.

3.1 Abstract

We present observations of WASP-63b by the *Hubble Space Telescope (HST)* as part of "A Preparatory Program to Identify the Single Best Transiting Exoplanet for *JWST* Early Release

Science". WASP-63b is one of the community targets under consideration for the *James Webb Space Telescope (JWST)* Early Release Science (ERS) program. We present a spectrum derived from a single observation by *HST* Wide Field Camera 3 in the near infrared. We engaged groups across the transiting exoplanet community to participate in the analysis of the data and present results from each. Extraction of the transmission spectrum by several independent analyses find an H_2O absorption feature with varying degrees of significance ranging from 1–3 σ. The feature, in all cases, is muted in comparison to a clear atmosphere at solar composition. The reasons for the muting of this feature are ambiguous due to a degeneracy between clouds and composition. The data does not yield robust detections of any molecular species other than H_2O. The group was motivated to perform an additional set of retrieval exercises to investigate an apparent bump in the spectrum at $\sim$ 1.55 μm. We explore possible disequilibrium chemistry and find this feature is consistent with super-solar HCN abundance but it is questionable if the required mixing ratio of HCN is chemically and physically plausible. The ultimate goal of this study is to vet WASP-63b as a potential community target to best demonstrate the capabilities and systematics of *JWST* instruments for transiting exoplanet science. In the case of WASP-63b, the presence of a detectable water feature indicates that WASP-63b remains a plausible target for *JWST* observations.

3.2 Introduction

The *James Webb Space Telescope* will revolutionize transiting exoplanet atmospheric science due to a combination of its capability for continuous, long duration observations and its larger collecting area, spectral coverage, and resolution compared to existing space-based facilities. We previously outlined a plan in Stevenson et al. (2016) to fully demonstrate the capabilities of the *JWST* instruments during the Early Release Science (ERS) program allowing the community to plan more efficient and successful transiting exoplanet characterization programs in later cycles.

Stevenson et al. (2016) identified a set of "community targets" which meet a certain set of criteria for ecliptic latitude, period, host star brightness, well constrained orbital parameters, and predicted strength of spectroscopic features. WASP-63b was identified as one of the strongest transmission spectroscopy candidates for *JWST* Early Release Science. It is an inflated planet (1.43 R_J) with a low mass of only 0.38 M_J (Hellier et al. 2012) resulting in a large atmospheric scale height. It orbits a bright (11.2 V_{mag}) star. Additionally, WASP-63b occupies an important, under-explored, region of transmission spectroscopy due to its mass. Most exoplanets studied in detail with transmission spectroscopy are either hot Jupiters of mass ($\sim$1–3 M_J)(e.g. Deming et al. 2013; Kreidberg et al. 2014b, 2015a; Line et al. 2016; Sing et al. 2016) or Super Earth-to-Neptune mass planets ($\sim$0.01–0.1 M_J) (e.g. Kreidberg et al. 2014a; Fraine et al. 2014; Knutson et al. 2014). In order to understand formation and evolution processes, it's important to understand the composition of atmospheres over a full and continuous range of masses (e.g. Mordasini et al. 2016).

WASP-63b will be accessible to *JWST* approximately six months after the planned April 2019 start of Cycle 1 and ERS observations making it an ideal candidate should there be any delays in the *JWST* timetable. Here, we observe WASP-63b to evaluate its suitability as a prime candidate to test the capabilities of *JWST*. We can use the strength of the water absorption feature at 1.4 μm as a way to screen potential targets for the presence of obscuring aerosols and determine the amplitude of predicted spectral features (e.g. Deming et al. 2013; Kreidberg et al. 2014b; Sing et al. 2016; Stevenson 2016). Ideally, a clear atmosphere with large amplitude spectroscopic features will be best suited for benchmarking the instruments and identifying their systematics.

3.3 Observations and Analysis

We observed the WASP-63 system using the *HST* Wide Field Camera 3 (WFC3) on September 19, 2016. The observations were taken as part of program GO-14642, "A Preparatory Program to Identify the Single Best Transiting Exoplanet for *JWST* Early Release Science" (PI Stevenson). The observations were made using the G141 grism in forward/reverse spatial scan mode. Spatial scanning (McCullough & MacKenty 2012) involves slewing the telescope in the cross dispersion

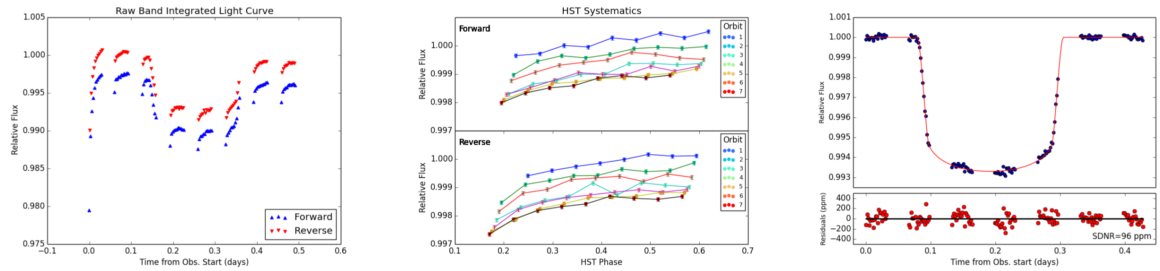

Figure 3.1 *Top:* The normalized raw band integrated light curve. Forward/Reverse scans are shown in red/blue. *Middle:* The Band Integrated Light Curve phase folded by *HST* Orbital Phase after removing the best fit transit model to illustrate the systematic 'hook' in WFC3 observations. The forward and reverse scan directions are shown in separate panels. Each color corresponds to an *HST* orbit. Note that here the first orbit has been discarded since it exhibits different systematics leaving only 7 orbits. The exponential increase over each orbit and a visit long decrease in response are evident by visual inspection. *Bottom:* The best fit white light curve shown with systematics removed. We achieve a standard deviation of the normalized residuals of 96 ppm.

direction during the exposure. In forward/reverse mode the telescope is exposing in both directions of the slew thus eliminating time to reset the target at the initial position on the detector between exposures. Each exposure, utilizing SPARS10, consists of 16 non-destructive reads with a total exposure time of approximately 103s which yielded peak per pixel counts near 32,000 electrons. The spectrum was read out using the 256 $\times$ 256 subarray with a scan rate of $\sim$ 0.08 arcsec/s (0.62 pixels/s). This corresponds to a total scan length of $\sim$ 8.76 arcsec which spreads the spectrum in the cross dispersion direction over $\sim$ 70 pixels. We observed WASP-63 for a total of 8 *HST* orbits, yielding a total of 86 time series integrations, to cover the entirety of the relatively long duration of transit ($\sim$ 5 hours).

We use the *IMA* files from the CalWF3 pipeline in our analysis. These files have been calibrated for dark current and zero read bias. We applied flat field corrections to each non-destructive read (NDR). Each NDR was background subtracted by considering a background window consisting of ($\sim$50) rows of pixels below the spectrum spanning the dispersion direction. A mean value for each column of the background window was taken to produce a one-dimensional background correction. The 1-D solution was then smoothed in the dispersion direction to correct for outliers. The column by column background value was then subtracted from each pixel of the image. We then extract the spectrum by taking the difference between successive NDRs. We apply a top hat filter to each NDR to limit any contribution from cosmic rays and/or overlapping spectra (Evans et al. 2016; Wakeford et al. 2017). The differences between each NDR are then summed to produce a final working image.

3.3.1 Band Integrated Light Curve

We perform the extraction of the band integrated light curve (white light curve) using a range of different aperture sizes in the cross-dispersion direction. The aperture sizes range from ± 10 pixels–± 10 Each orbit includes a direct image of the star from which we calculate the stellar centroid using applying a 2-D Gaussian fit to a 5×5 section of pixels centered on maximum pixel. The trace and wavelength solutions are calculated from the centroid of the undispersed image using the coefficients provided in Kuntschner et al. (2009). We extract a box from each working image with the number of columns corresponding to wavelength limits 1.125-1.65 μm and rows determined by the chosen aperture size. The band integrated light curve is the summation of all pixels within the box at each time step. The results of the initial extraction of the raw white light curve are shown in Figure 3.1 (top).

Fitting the white light curve requires accounting for *HST* systematics. We choose to follow the standard practice of discarding the first orbit as it presents different systematics from the remainder of the data (e.g. Deming et al. 2013; Stevenson et al. 2014). The raw light curve exhibits a ramp like increase in flux, commonly referred to as the 'hook', with each *HST* orbit consistent with previous observations (e.g. Berta et al. 2012; Deming et al. 2013; Fraine et al. 2014; Kreidberg et al. 2014b). The hook effect, shown in Figure 3.1 (middle), is generally steeper in the first frame of each *HST* orbit so we discard those data points. We then model the hook as an exponential plus linear function of the form $1 - A\exp\{S(\theta-\theta_0)\} + c_1\theta$ where θ is the *HST* orbital phase, θ_0 is a reference angle for setting zero *HST* phase and A, S, and c_1 are scaling factors. The hook model is combined multiplicatively with a second order polynomial in time over the entirety of the observation.

We model the transit using the methods of Mandel & Agol (2002) implemented by the Python routine BATMAN Kreidberg (2015). The transit model assumes a circular orbit with a fixed period. Orbital parameters used for the transit model were taken from Hellier et al. (2012). We calculate non–linear limb darkening coefficients using the PHOENIX Code to fit theoretical spectra as described in detail in de Wit et al. (2016). We assume a stellar T_{eff} of 5550±100 K and log(g) of 4.01 +0.02/-0.04 producing coefficients $c_1 ... c_4$ of (0.36627439, 0.63188403, -0.69135111, 0.23393244) for a limb darkening law of the form $I(\mu) = I_0[1 - c_1\left(1 - \mu^{1/2}\right) - c_2\left(1 - \mu\right)] - c_3\left(1 - \mu^{3/2}\right) - c_4\left(1 - \mu^2\right)$. During the fitting process we allow for the time of transit center ($T_{\rm cen}$), planetary radius as a fraction of stellar radius ($R_p/R_\star$), a/$R_\star$, inclination (i), and a normalizing factor (the ratio of the amplitudes of the scan directions) to be free parameters and fit both scan directions simultaneously. All fits and uncertainty estimates are derived from the Python routine 'emcee' (Foreman-Mackey et al. 2013) utilizing 50 walkers with 10^4 steps. Each walker is initialized at a point in parameter space determined by randomly shifting the value of each parameter by some fraction of twice the corresponding one sigma uncertainty. This forms an over–distributed sphere of starting points surrounding the initial best fit value. Given the number of observational data during both ingress and egress we place uninformative priors on the orbital properties. The first 20% of steps are removed for burn in. We test for convergence using Gelman Rubin statistics with a threshold for acceptance of 1.1 and find convergence to levels of 1.01–1.03 in all cases (Gelman & Rubin 1992). We choose the best aperture by minimizing the scatter of the residuals of the white light curve fit. We find a best aperture of $\pm$ 44 pixels in the spatial direction centered on the spectral image centroid. We achieve a standard deviation of the normalized residuals (SDNR) of 96 parts per million (ppm). There is no indication that the selection of aperture size has a statistically significant effect on the transit depth fit. The standard deviation of the transit depth for the five apertures above and below the best aperture is 93 ppm with an average Rp/Rs of 0.077761. These results all fit well within our best fit value and uncertainty. The best fit white light curve is shown in Figure 3.1 and the values and uncertainties for the planetary physical properties and ephemeris from the best fit white light curve are presented in Table 3.3.1.

Table 3.1. Best fit values and uncertainties for the planetary physical properties and ephemeris from the band integrated light curve fit.

$R_p/R_\star$	$T_{cen}(MJD)$	$a/R_\star$	i (°)
$0.077762\pm^{0.000204}_{0.000183}$	$57650.435\pm^{6.97\times10^{-5}}_{5.93\times10^{-5}}$	$6.633\pm^{0.031}_{0.015}$	$88.52\pm^{0.26}_{0.12}$

Table 3.2. Transmission spectrum of WASP-63b measured with *HST* WFC3 G141 grism.

BMK			KBS			HRW		
Wavelength(μm)	$R_p/R_\star$	Unc (ppm)	Wavelength(μm)	$R_p/R_\star$	Unc (ppm)	Wavelength(μm)	$R_p/R_\star$	Unc (ppm)
1.1425	0.07791	310	1.1425	0.07819	290	1.1352	0.07810	460
1.1775	0.07732	290	1.1775	0.07801	275	1.1677	0.07740	450
1.2125	0.07717	300	1.2125	0.07785	290	1.2002	0.07762	430
1.2475	0.07753	300	1.2475	0.07770	270	1.2327	0.07839	420
1.2825	0.07812	280	1.2825	0.07848	260	1.2651	0.07832	420
1.3175	0.07789	270	1.3175	0.07846	285	1.2977	0.07782	420
1.3525	0.07847	290	1.3525	0.07853	265	1.3301	0.07832	420
1.3875	0.07891	300	1.3875	0.07861	270	1.3626	0.07921	420
1.4225	0.07832	290	1.4225	0.07826	290	1.3951	0.07880	425
1.4575	0.07839	300	1.4575	0.07849	280	1.4275	0.07848	440
1.4925	0.07773	330	1.4925	0.07791	290	1.4600	0.07862	445
1.5275	0.07865	330	1.5275	0.07831	295	1.4925	0.07811	450
1.5625	0.07866	370	1.5625	0.07833	320	1.5250	0.07908	455
1.5975	0.07816	350	1.5975	0.07752	310	1.5575	0.07892	485
1.6325	0.07751	360	1.6325	0.07718	320	1.5899	0.07821	490
						1.6224	0.07789	505

3.3.2 Spectral Light Curves

The spectral light curves are extracted using the same aperture we found to minimize the SDNR of the white light curve. The range of wavelengths included in our aperture are divided into 15 bins of width 0.035 μm ($\sim$10 pixels). The spectrum from each frame is compared to the spectrum of the first frame using cross correlation in Fourier space to check for any shift in the wavelength–pixel solution. The shift in wavelength solution throughout the observation was on the order of a few tenths of a pixel. Each column was summed and weighted by the fraction of that pixel in the bin.

The systematics were removed from the spectral light curves using the divide white method (Deming et al. 2013; Kreidberg et al. 2014b; Stevenson et al. 2014). Removing the best fit transit from the white light curve leaves only the systematics. We divide each spectral light curve by the systematics. This assumes that the systematics are wavelength independent. We do note a linear, observation–long, wavelength dependence in the corrected spectral light curves. We use a first order polynomial to account for the wavelength dependent systematics combined with the transit model when fitting the spectral light curves. We fix the ephemerides to the white light curve solutions and use fixed, wavelength dependent, non-linear limb darkening coefficients derived in the same way as described in Section 3.3.1. The transit depth and normalization factors are left as the only free parameters. We fit both scan directions simultaneously. Spectral light curves and their fits are shown in Figure 3.3.2.

3.3.3 Transmission Spectrum

A transmission spectrum was derived from the transit depth fits of the spectral light curves. The change in the apparent planetary radius as a function of wavelength can be indicative of absorption features of molecular species in the planetary atmosphere. As a test for robustness, the spectrum of WASP-63b was extracted using multiple independent analysis pipelines in addition to the method described in detail in the previous subsections (Table 3.3.1). Figure 3.3 shows a comparison of the results from this methodology (BMK) with that of analysis performed using methods described in Stevenson et al. (2014) (KBS) and Wakeford et al. (2016, 2017) (HRW). The spectra are in

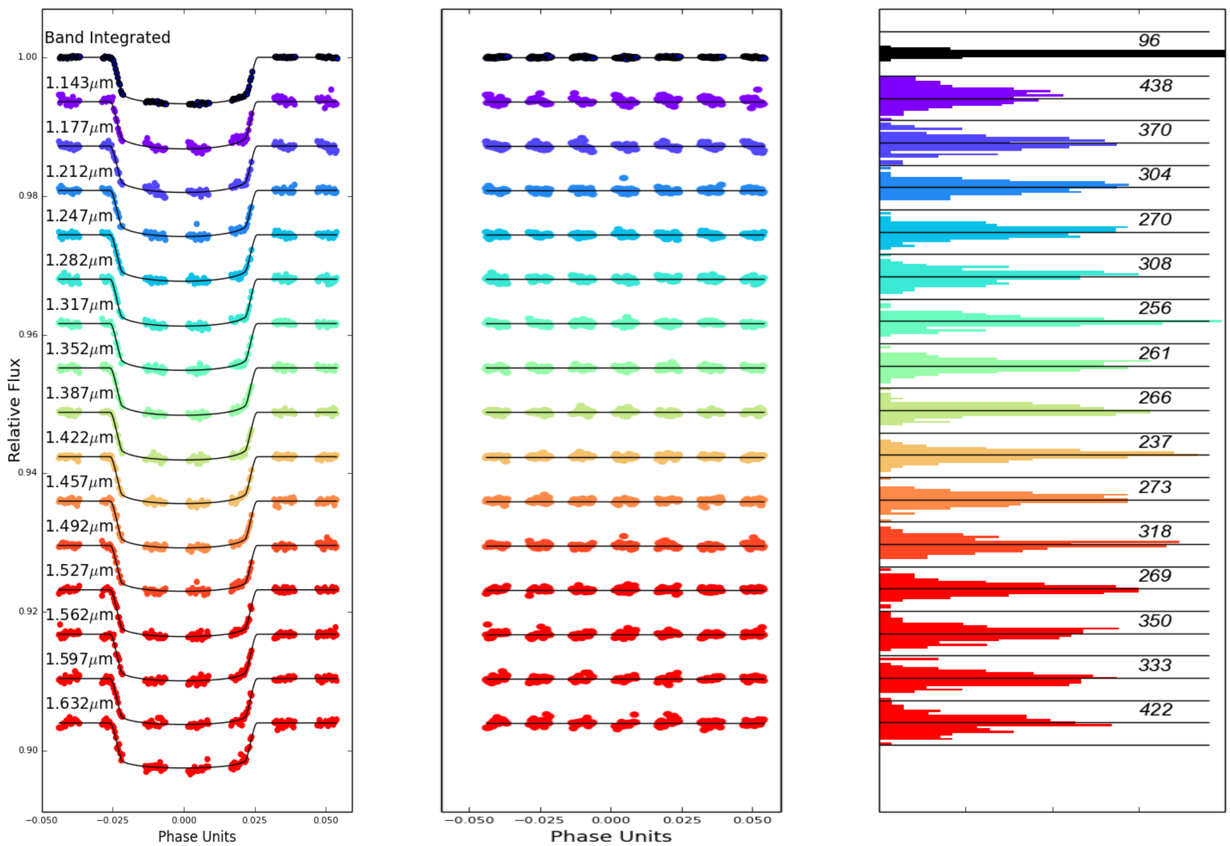

Figure 3.2 *Left:* Spectrophotometric transit light curves (colored dots) with systematics removed compared with the best fit transit (solid line). Light curves are shown as orbital phase (0-1 with 0 as the center of transit) vs. relative flux (vertically shifted for clarity). Each light curve is labeled with the central wavelength of the spectral bin. *Center:* Residuals to the fit. *Right:* Normalized histograms of the residuals. The solid black horizontal lines are spaced at 1000 ppm intervals for scale and the SDNR of each fit is listed in units of ppm.

good agreement with nearly all points from each of the methods in 1σ agreement with each of the other methods. As a test to determine how small differences in the extracted spectrum would affect retrieval results we analyzed the KBS and HRW spectra with the Pyrat Bay model (Section 3.2.1). The KBS spectrum has a shallower bump at 1.5 μm, and thus, the retrieval only detected the water signature significantly (not HCN). The HRW atmospheric retrieval produced similar results to BMK, but with broader 1σ constraints, due to the larger uncertainties of the dataset (compared to BMK or KBS).

We compared these results against a flat-line model using the Bayesian Information Criterion (BIC, Liddle 2007). For the atmospheric model of each dataset we searched for the combination of free parameters that minimized BIC.

For KBS, the BIC favors the atmospheric model (BIC=24.59, with three free parameters, T, $R_{0.1\mathrm{bar}}$, and H_2O), against the flat-line model (BIC=30.82, one free parameter). The posterior odds give the flat-line model a fractional probability of only 0.04 (Raftery 1995).

For HRW, the BIC favors again the atmospheric model (BIC=19.19, with four free parameters, T, $R_{0.1\mathrm{bar}}$, H_2O, and HCN) over the flat-line model (BIC=22.92). However, this time there is weaker evidence, with the flat-line model having a fractional probability of 0.13.

Therefore, in all three datasets, there is evidence of spectral features, but with different degrees of confidence. The BMK spectrum shows strong evidence, KBS spectrum shows moderate evidence, whereas HRW shows only weak evidence for water absorption. The HRW spectrum is based upon the marginalization technique described in Wakeford 2016 and represents the most conservative estimate of uncertainty. As such, it serves as a sort of lower bound on the detection threshold whereas the BMK and KBS methods assume we are justified in our choice of systematic model. The arguments for this choice of model are well extablished and summarized in Section 3.3.1 and so we will choose the BMK spectral extraction to continue on with retrieval analysis.

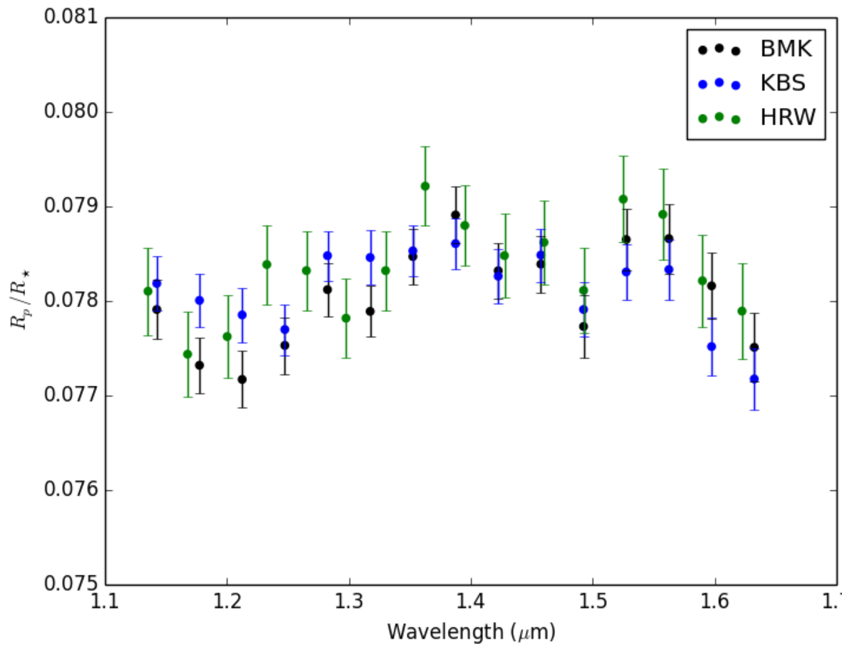

Figure 3.3 Results of spectral extraction from multiple independent analyses show good agreement. Here we show the best fit value for $R_p/R_\star$ as a function of wavelength with 1σ error bars derived from the MCMC posteriors. Colors correspond to analysis performed by Brian Kilpatrick (BMK), Kevin Stevenson (KBS), and Hannah Wakeford (HRW).

3.4 Results

The results produced by the methodology described in in detail in Section 3.3 (presented in Table 3.3.1 as BMK) were distributed to the members of the transiting exoplanet community who were involved with the preparation of Stevenson et al. (2016) and/or *HST* program GO 14642. Each was given an opportunity to provide an independent analysis of the results. Wide community involvement resulted in a number of contributions in the form of forward model comparisons and retrievals. Here we present the methods and findings from each interpretation of the BMK spectrum. All models in this section adopt the system parameters from Hellier et al. (2012).

3.4.1 Forward Models

Burrows

We apply the transit models from Howe & Burrows (2012), which adopt chemical equilibrium abundances for molecular species from Burrows & Sharp (1999) and opacities from Sharp & Burrows (2007). The atmospheric models consider an isothermal temperature profile and gray haze opacity with cross sections of 0.001–0.005 $cm^2 g^{-1}$ from 10^{-6} bar to 1 bar.

By exploring a range of temperatures, haze opacities, metallicities, and non-equilibrium CO/CH_4 abundances, the best-fitting solutions pointed to solar-abundance atmospheres at a temperature of 1000 K, with a haze/cloud muting the water absorption feature at 1.4 μm (Figure 3.4, top panel). There is no indication of significant CH_4. There is a slight degeneracy between the cloud thickness and temperature, but it is clear that the atmosphere is cloudy. These models do not show a significant metallicity dependence. Finally, a high CO abundance excess ($\sim$100 times solar) can help to fit the data at 1.5 μm, but it does not seem realistic.

Heng

As a complementary approach to the full retrieval calculations, we fit the data with a 3-parameter analytical model (Heng & Kitzmann 2017). In that study, it was demonstrated that this isothermal, isobaric model matched full numerical calculations at the $\sim 0.1\%$ level over the WFC3 wavelength range. The model has three parameters: temperature, water abundance, and a constant cloud opacity. The constant cloud opacity assumes that the cloud particles are large over the wavelength range probed by WFC3 (i.e., micron-sized or larger radius). Water opacities are computed using the HELIOS-K opacity calculator (Grimm & Heng 2015) and the HITEMP spectroscopic database. This procedure confronts the data with a simple model, which has a minimal number of parameters, to serve as a plausibility check.

Following the approach of Kreidberg et al. (2015b), we equate the reference transit radius to the white-light radius and set the reference pressure to 10 bar. We assume a hydrogen-dominated atmosphere and set the mean molecular weight to 2.4. The top panel of Figure 3.4 shows the best-fit model to the WFC3 WASP-63b data. Our general conclusion mirrors that of the retrieval calculations: water is present in the atmosphere of WASP-63b, but its presence is muted by a continuum, which in this case is attributed to a constant cloud opacity. The values of our fitting parameters span a temperature range from 500 to 1000 K, a water mixing ratio from $\sim 10^{-8}$ to 10^{-7}, and a cloud opacity $\sim 10^{-8}$ to 10^{-7} cm^2 g^{-1}.

Morley

In order to determine the clouds that are predicted to form in the atmosphere of WASP-63b and their effect on the planet's transmission spectrum, we ran self-consistent models including the effects of cloud condensation. These models solve for the temperature structure of the atmosphere in radiative-convective and chemical equilibrium and are more extensively described in McKay et al. (1989); Marley et al. (1996); Burrows et al. (1997); Marley et al. (1999, 2002); Fortney (2005); Saumon & Marley (2008); Fortney et al. (2008); Morley et al. (2015). Our opacity database for gases is described in Freedman et al. (2008, 2014), and we calculate the effect of cloud opacity using Mie theory, assuming spherical particles. We include iron and silicate clouds and vary the cloud sedimentation efficiency $f_{\rm sed}$ from 0.1 to 1, and find that these clouds do indeed form at high altitudes and damp the size of the signal for low sedimentation efficiencies (i.e. lofted clouds of small particles). Figure 3.4 top panel shows a representative transmission model for WASP-63b.

Parmentier

In order to understand how the three-dimensional structure of the planet might affect our interpretation of the planet's transmission spectrum, we model WASP-63b with the three-dimensional global circulation model SPARC/MITgcm described in Showman et al. (2009). Our model solves for the three-dimensional temperature structure of the atmosphere assuming a cloud-free, solar-composition atmosphere. We then use the temperature map to predict the position of the clouds at the limb of the planet by comparing the partial pressure and the saturation pressure of the cloud gaseous constituents as described in Parmentier et al. (2016). The cloud top level and size of the cloud particles are free parameters representing vertical mixing and microphysics respectively. We then compute the transmission spectrum of the whole atmosphere by combining the transmission spectrum obtained with the temperature and cloud profile at each latitude around the limb (Parmentier et al. 2018).

Our global circulation model predicts a temperature difference of $400\mathrm{K}$ between the east and west limb at the 10 mbar level. As a consequence some cloud species are predicted to be condensed all over the limb of the planet whereas others should condense only on the morning limb and be evaporated on the other one, leading to a partially cloudy atmosphere (Line & Parmentier 2016). We computed models assuming the presence of enstatite clouds ($\mathrm{MgSiO_3}$) or manganese sulfide clouds (MnS) corresponding to a fully cloudy and partially cloud case respectively. Our best fit spectrum with enstatite clouds is very similar to the Morley model of Fig.4. It has a cloud top pressure of 1 mbar and no constraints on the particle size. Our best fit model with MnS clouds is the Parmentier model of Fig. 4. It has a limb that is $\approx 60\%$ cloudy, resulting in a qualitatively different spectrum than the other, one-dimensional models shown here. For this model the cloud top pressure is ≈ 0.1 mbar and the particle size is $\approx 1\mu$m. We conclude that the atmosphere of WASP-63b is unlikely to be clear with a solar-composition abundance of water. Both fully cloudy and partially cloudy atmospheres can exist, depending on the cloud composition. A higher signal to noise spectrum should be able to disentangle between the two scenarios.

3.4.2 Retrievals

Four groups provided atmospheric retrieval analyses for WASP-63b. The following subsections describe the retrieval procedure and the individual exploration from each group. Figures relative to the individual retrievals are included in Appendix A.

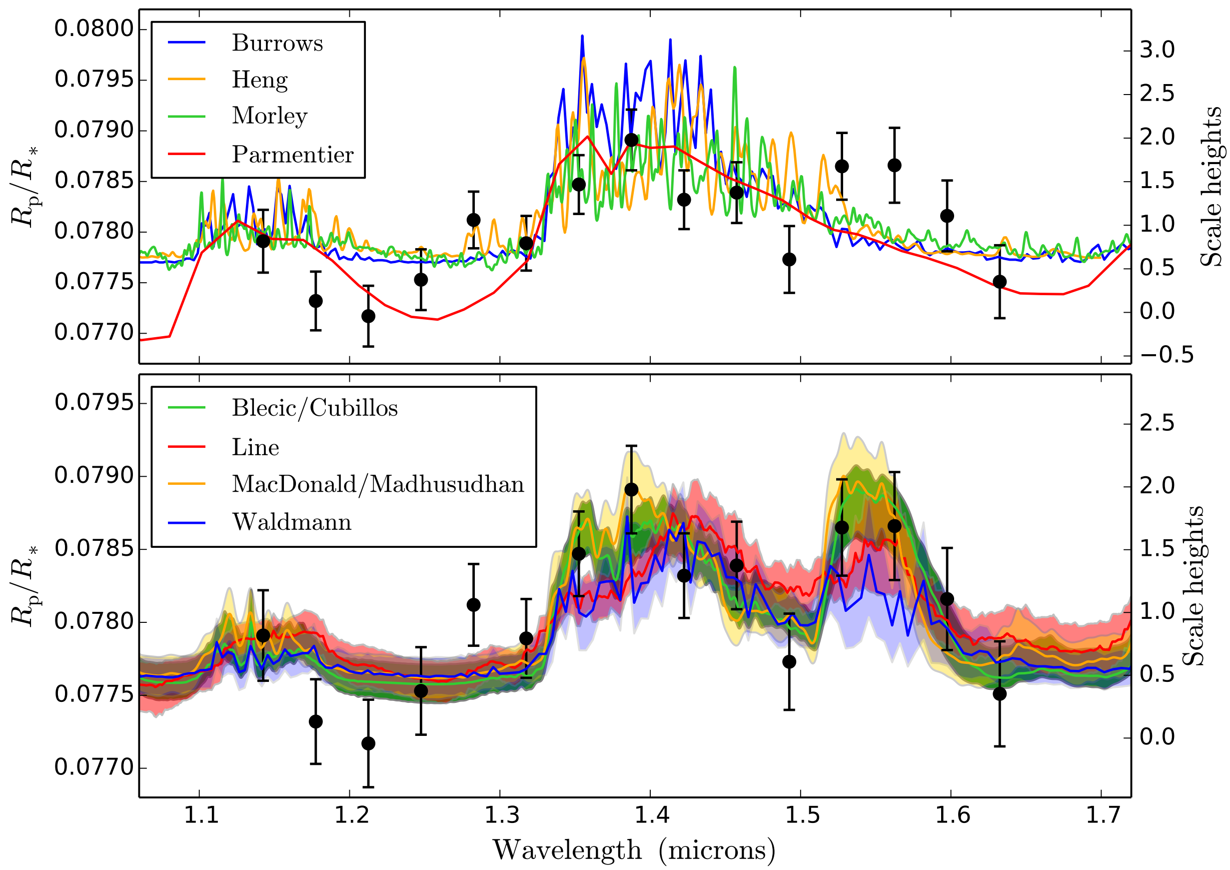

Figure 3.4 *Top:* WASP-63b spectrum and forward models. The black dots with error bars denote the observed best-fit radius ratio and 1σ uncertainties. The labeled solid curves show representative forward model fits to the data described in section 3.4.1. *Bottom:* WASP-63b spectrum and retrieval models including HCN absorption. The black dots with error bars denote the observed best-fit radius ratio and 1σ uncertainties. The labeled solid curves denote the best-fitting models for the consistent retrieval run described in section 3.5. The vertical shaded areas around each model denote the span of the 1σ confidence region of the posterior distribution of sampled models.

Blecic & Cubillos

To model the atmosphere and spectrum of WASP-63b we use the Python Radiative Transfer in a Bayesian framework (Pyrat Bay) package[1] (Cubillos et al. 2018, in prep.; Blecic et al. 2018, in prep.). Pyrat Bay is an open-source reproducible code, based on the Bayesian Atmospheric Radiative Transfer package (Blecic 2016; Cubillos 2016). The code provides a line-by-line radiative-transfer and a thermochemical-equilibrium abundances (TEA, Blecic et al.

[1]http://pcubillos.github.io/pyratbay http://pcubillos.github.io/pyratbay

2016) module, which can be use in forward or retrieval mode, via a Differential-evolution MCMC sampler (Cubillos et al. 2017). The atmospheric model consist of a 1D set of concentric shell layers, in hydrostatic equilibrium, spanning from 10^{-8} to 100 bar. For the temperature profile we consider either the three-channel Eddington approximation parameterization (TCEA, Line et al. 2013b) or an isothermal profile.

The Pyrat Bay code considers molecular opacities for H_2O from HITEMP (Rothman et al. 2010), NH_3 and CH_4 from HITRAN (Rothman et al. 2013), and HCN from Exomol (Barber et al. 2014). We compressed these line-by-line data files using the REPACK package (Cubillos 2017) to extract only the strong lines that dominate the spectrum, speeding up the radiative-transfer calculation. Additionally, Pyrat Bay considers collision induced absorption (CIA) from H_2-H_2 (Borysow et al. 2001; Borysow 2002) and H_2-He (Borysow et al. 1988, 1989; Borysow & Frommhold 1989); and H_2 Rayleigh scattering (Lecavelier Des Etangs et al. 2008). We also consider two cloud parameterizations, a simple gray-cloud opacity with constant cross section (cm^{-2} molec^{-1}) below 10^{-5} bars, and a thermal-stability cloud model based on the approach described in Ackerman & Marley (2001) and Benneke (2015), with additional flexibility (Blecic et al. 2018, in prep). We compute the opacity for either Fe or $MgSiO_3$ condensates using Mie-scattering theory (Toon & Ackerman 1981).

The retrieval parameterization includes free scale factors for the mixing ratios of H_2O, NH_3, CH_4, and HCN (vertical-constant values) and the mean molecular mass of the atmosphere; either the isothermal temperature or the κ, γ, and β parameters of the TCEA model (see Line et al. 2013b); the gray cloud cross section or the Mie-scattering cloud profile shape, condensate mole fraction, particle-size distribution, and gas number fraction just below the cloud deck.; and the planetary radius at 0.1 bar.

We explored several cases, obtaining qualitatively good fits in all gray-cloud, complex-cloud, and clear-atmosphere cases. As expected for transmission spectroscopy, the retrieval returned largely unconstrained parameters for the TCEA temperature model, suggesting that the data does not justify more complex models than an isothermal profile. In all cases the MCMC favors lower temperatures ($T < 1000$ K) than equilibrium temperature (1500 K) at the pressures probed by the observations. We constrain the water abundance, ranging from solar to ~0.1 times solar values. The observed water absorption feature is muted relative to a clear atmosphere with solar abundances. This is caused by a sub-solar water abundance, an absorbing cloud opacity, or a high mean molecular mass, which reflects in a strong correlation between the water abundance and the cloud cross-section. When we compare retrievals with the gray and complex cloud model, we find similar best-fitting spectra between the two cases. The complex-cloud retrieval does not constrain any of the cloud parameters when we set all four species abundances free. In the case when we set the water abundance as the only abundance free parameter, we find a somewhat better condensate-fraction constraint. Since the cloud opacity dominates only a limited region of the observed spectrum (~1.2–1.3 μm), we conclude that there is no need for a more complex cloud model for this study. The Reproducible Research Compendium for the Pyrat Bay models is available at https://github.com/pcubillos/KilpatrickEtal2018_WASP63b https://github.com/pcubillos/KilpatrickEtal2018_WASP63b.

Line

We use the CHIMERA transmission model (Line et al. 2013a; Swain et al. 2014; Kreidberg et al. 2014b, 2015b; Greene et al. 2016; Line et al. 2016). For transit geometry, the code solves the radiative-transfer equation for parallel rays across the terminator of the planet (Brown 2001; Tinetti et al. 2012). The code integrates atmospheric opacities from either correlated-K or sampled "line-by-line" absorption cross sections. To explore the parameter space, the transmission model is coupled with the PyMultiNest (Buchner et al. 2014) multimodal nested-sampling algorithm (Feroz & Hobson 2008). The atmosphere is in hydrostatic equilibrium with height-dependent gravity, temperature, and molecular weight. The temperature profile comes from either the radiative-equilibrium model from Guillot (2010) or an isothermal profile, spanning from 10^{-7} to 30 bar. The atmosphere uses 'thermochemically-consistent' molecular abundances (as defined in Kreidberg et al. 2015b), computed using the NASA CEA2 model for given elemental abundances (Lodders 2009).

The CHIMERA code considers molecular opacities for H_2O, CH_4, CO, CO2, NH_3, Na, K, TiO, VO, C_2H_2, HCN, and FeH (Freedman et al. 2014); CIA from H_2-H_2 and H_2-He Richard et al. (2012); a Rayleigh power-law haze (Lecavelier Des Etangs et al. 2008); and either an opaque gray patchy cloud model (Line & Parmentier 2016) or a more complex, Mie-cloud model (Lee et al. 2013).

The retrieval parameterization includes the metallicity $[\mathrm{M/H}]$, the carbon-to-oxygen ratio $\log(\mathrm{C/O})$, and the carbon- and nitrogen-species quench pressures (Kreidberg et al. 2015b; Morley et al. 2017) to set the elemental abundances; either the isothermal temperature or the κ_{IR}, γ_v, T_{irr} parameters of (Guillot 2010); the top-pressure boundary and a 'patchy terminator' parameter for the gray patchy cloud model, or the Q_0 and r (see Lee et al. 2013) and profile shape (mixing ratio, cloud base pressure, pressure fall off index, Line et al. 2017, in prep.) for the Mie-cloud model; and a radius scale factor to set the reference altitude at 10 bar.

The 'chemically-consistent' retrieval detects the water spectral feature at 3.6σ confidence. This is consistent with a hard upper limit on C/O near 1. The water band is muted relative to solar composition. The retrieval posterior shows two 'composition' modes: low metallicity ($[\mathrm{M/H}] \lesssim 1.3$ (20×)) degenerate with a cloud and high metallicity (peak near ∼300×solar). There is a turn-over degeneracy in cloud top vs. [M/H] (due to the effect on the mean molecular weight) resulting in the bi-modal marginalized metallicity distribution. Clouds can be present, but are not required to fit the spectra as given by the Bayes factor (0.45) and result in a much lower value for the low metallicity mode ($< 0.1\times$solar), while the high metallicity mode remains. The highest of the sampled metallicities (greater than ∼50 times solar) are possibly implausible given mass and radius of WASP-63b.

Further tests found negligible variations when imposing a temperature prior or no patchy-cloud factor. A comparison between correlated-K and line-by-line sampling opacities produced nearly identical results. Likewise, the more complex Mie-cloud model produced qualitatively similar main conclusions (with unconstrained cloud particle sizes, vertical extent, or cloud composition).

MacDonald & Madhusudhan

We use the nested-sampling retrieval algorithm POSEIDON (MacDonald & Madhusudhan 2017) to analyze the WFC3 observations of WASP-63b. The code pre-computes line-by-line molecular cross sections following the methodology of Hedges & Madhusudhan (2016) and Gandhi & Madhusudhan (2017). To compute detection significances we conduct nested Bayesian model comparisons. For simplicity, we model the atmosphere assuming an isothermal temperature-pressure profile, with 100 layers uniformly spaced in log-pressure from 10^{-6} to 100 bar, in hydrostatic equilibrium.

The POSEIDON code considers molecular opacities for H_2O from HITEMP (Rothman et al. 2010) and CH_4, NH_3, and HCN from Exomol (Tennyson et al. 2016); CIA from H_2-H_2 and H_2-He (Richard et al. 2012); Rayleigh scattering (Lecavelier Des Etangs et al. 2008); and a uniform-in-altitude gray opacity cloud model.

The retrieval parameterization includes free scale factors for the mixing ratio of H_2O, CH_4, NH_3, and HCN; the isothermal temperature; the gray-cloud opacity; and the reference pressure at the transit radius.

The model comparison test marginally prefer the gray-opacity case ($\chi^2_{\mathrm{red}} = 1.21$) over a cloud-free case ($\chi^2_{\mathrm{red}} = 1.46$), with a Bayes factor of 2.2. Adopting the gray-opacity model, we detect H_2O at 4.0σ (Bayes factor = 601), HCN at 3.1σ (Bayes factor = 27.6), and 'nitrogen chemistry' (combination of HCN and NH_3) at 3.3σ (Bayes factor = 53.7). We do not detect CH_4.

Waldmann

We retrieved the *HST* /WFC3 spectrum of WASP-63b using the Tau-REx atmospheric retrieval framework (Waldmann et al. 2015b,a; Waldmann 2016). Based on the Tau code transmission forward models by Hollis et al. (2013), Tau-REx employs Nested Sampling (Feroz & Hobson

2008) to solve the full Bayesian argument. Tau-REx can use high-resolution absorption cross-section or correlated-k tables as opacity inputs. Here we used the latter but find both to yield equivalent results for the wavelength ranges and sensitivities of the data at hand. We include pressure-dependent line broadening where such information is available, taking into account the J quantum number dependence on pressure broadening coefficients. In this study, we assume an isothermal atmospheric temperature-pressure profile, spanning from to 10^{-9} to 10 bar.

The Tau-REx code considers molecular opacities for H_2O, CH_4, NH_3, HCN, TiO, and VO from Exomol (Tennyson & Yurchenko 2012),CO and CO2 from HITEMP (Rothman et al. 2010), and O_2, O_3, NO_2, NO, HCOOH, C_2H_6, and C_2H_2 from HITRAN (Rothman et al. 2009, 2013); CIA from H_2-H_2 (Borysow et al. 2001; Borysow 2002) and H_2-He (Abel et al. 2012); Rayleigh scattering (Lecavelier Des Etangs et al. 2008); and clouds using a hybrid model of gray-cloud opacities and a phenomenological Mie scattering (Lee et al. 2013).

We run two types of retrievals, a 'free' retrieval with abundances of H_2O, CH_4, CO, CO_2, NH_3, as well as a chemical-equilibrium retrieval using an implementation of the ACE model by Agúndez et al. (2012), with the C/O ratio and atmospheric metallicity as free parameters. The rest of the retrieval parameters are the isothermal temperature; the top pressure of the gray cloud model and the particle size, composition and mixing ratio of the Mie-cloud model; and the planet reference radius at 10 bar.

We detect water with a 3.5σ significance (Bayes factor = 103) compared with a family of pure-cloud or featureless atmosphere models. We obtain $\log(\mathrm{H_2O}) = -4.84^{+1.04}_{-1.53}$. We do not find any evidence of an extended Rayleigh curve due to hazes but found a gray-cloud model to be sufficient. We constrain the cloud-top pressure to $\log(p) = 3.08^{+1.48}_{-0.93}$ Pa. The chemically consistent retrieval yielded two results. The first result yields a high metallicity atmosphere at 370 times solar. The second result yields a low metallicity atmosphere at 0.24 times solar. Both solutions feature comparable log-evidences and result in upper bounds of C/O at 0.49. A ratio of $\mathrm{C/O} < 0.7$ is expected as only water is retrieved in this data set and is therefore consistent with the 'free' retrieval approach above. The atmospheric metallicity is poorly constrained due to the presence of clouds

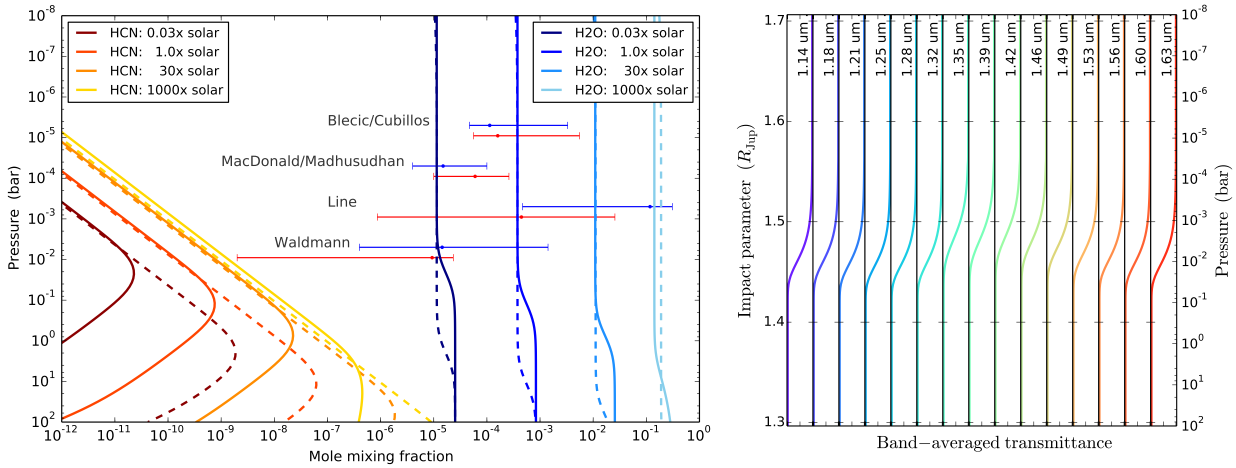

Figure 3.5 *Left:* water and HCN abundances for WASP-63b compared to thermochemical-equilibrium mole mixing fractions models for an isothermal atmosphere at 1000 K (solid lines) and at 1500 K (dashed lines) at a range of metallicities (see labels). The horizontal error bars show the retrieved 68% credible-region abundances from each group (labels) for water (blue) and HCN (red). **Note that the retrieved abundances are vertically offset for clarity, see right panel for the probed pressures.** All abundances correspond to the pressure levels probed by this transmission observation (10^{-2}–10^{-4} bar). All retrieved water abundances are consistent with solar or slightly sub-solar water abundances, however the retrieved HCN values range several order of magnitudes higher than any 1000 K equilibrium value (particularly for the solar to sub-solar HCN curves). The retrieved mole mixing fractions of HCN are more plausible if the temperature at deeper layers were ∼1500 K and vertical transport dominated the abundances in the region probed by observations. The models suggest it would be possible under these conditions to produce mole mixing fractions on the order of 10^{-6}. *Right:* Sample transmittance curves as a function of impact parameter for each WFC3 pass band (see labeled wavelengths) for the Blecic/Cubillos retrieval best fit. The transition from optically thin to optically thick between ∼1.5 an ∼1.4 $R_{\rm Jup}$, respectively, denotes the photosphere of the planet, as observed by WFC3. The pressure scale on the right side denotes the deepest atmospheric pressure probed by each impact parameter. The transmittance curves from other groups show a similar trend.

which has the effect of muting the water feature and biasing the chemical-consistent model to either compensate with unrealistically high mean molecular weight atmospheres or unrealistically low trace gas abundances.

3.5 Discussion

The individual atmospheric analyses of WASP-63b agree that there is a robust water detection (3.5–4.0 σ), but with a muted absorption feature when compared to a clear solar-composition atmospheric model. It is unclear if the reason for the muting of the feature is the result of sub-solar water abundance, absorbing cloud opacity, or a high mean molecular mass. Thermochemically-consistent retrievals show a multimodal solution due to degeneracies between cloud opacity and composition (Figures: A.2 and A.4). Retrievals with simple temperature (isothermal) and cloud (gray opacity) models both produced fits consistent with retrievals with more complex models and thus the data does not warrant the incorporation of more complex models nor does it allow further constraints on cloud properties.

The high transit-depth values between 1.5 and 1.6 μm motivate the inclusion of HCN and the exploration of disequilibrium chemistry. Each retrieval team performed an additional retrieval exercise with a common set of assumptions to further explore the the inclusion of HCN as a means to fit the 'bump' in the spectrum between 1.5 and 1.6 μm. We implemented an isothermal temperature model, a gray-opacity cloud model, a free pressure–radius reference point, and opacities from H_2-Rayleigh, H_2-H_2 and H_2-He CIA, and H_2O, CH_4, HCN, and NH_3. We adopted molecular abundances either from thermochemically-consistent calculations or from free abundances (constant vertical profiles), with the exception of the HCN abundance, which is always a free fitting variable (constant vertical profile).

We begin with this common set of assumptions and then compare retrieval results from teams with differing retrieval frameworks. Notable differences include: the statistical sampler from Blecic/Cubillos (MCMC) differ from the rest (Nested sampling), the molecular opacity handling from Waldmann and Line (correlated-K) differ from the others (cross-section sampling), and the chemistry from Line (thermochemically-consistent) differs from the rest (free constant vertical profiles). Figure 3.4 shows the retrieved spectrum from the run using the common assumptions. All four retrievals produced consistent spectral fits, seen in the intersecting 68% confidence regions around the best-fitting models. In terms of the atmospheric characterization, these retrievals confirm the previously found water detection.

The Bayesian hypothesis testing favors the fit with HCN, improving the fit at 1.5–1.6 μm. However, the detection significance is low and inconsistent, 3.1σ (Blecic/Cubillos), 2.1σ (Line), 3.1σ (MacDonald/Madhusudhan), and 1.9σ (Waldmann). Therefore, for the currently available data, the inclusion of HCN is not statistically justified within this model parameterization. Furthermore, to reproduce the observed values requires the HCN mole fraction be $\gtrsim 10^{-5}$; much higher than thermochemical-equilibrium values at the pressures probed by the WFC3 observations (Figure 3.5). To produce such high HCN abundances, one would need to invoke disequilibrium-chemistry processes by either quenching or photochemistry. Quenching can occur when higher temperatures at deep layers, below the levels probed by this observation, enhance the HCN abundance without needing the high metallicities from Figure 3.5. If vertical mixing dominates the mid-altitude abundances of the WASP-63b atmosphere (expected at the retrieved temperatures of $\sim$1000 K), HCN could be effectively quenched, maintaining the high abundances from the deep layers throughout the probed region. Similar deviations from equilibrium chemistry have been modeled for other Jupiter-like exoplanets (Moses et al. 2011; Venot et al. 2012). None of the retrievals constrain any of the other molecular abundances that could provide additional evidence for quenching (e.g. CO, CH_4, NH_3). However, photochemistry could play a role in removing these other molecules from the atmosphere while enhancing the mole fraction of HCN at pressures less than a millibar. Moses et al. (2011, 2013) show that ammonia and methane can be photochemically converted to HCN at the pressure levels probed by near–IR transmission spectroscopy thus driving the retrieved abundances much higher than equilibrium values. Future observations with extended wavelength ranges and higher sensitivity, such as *JWST* , can help to definitively confirm or rule out the detection of HCN, and other atmospheric species, thus constraining the presence of disequilibrium chemistry.

3.6 Conclusions

We present the observations of one transit of the hot Jupiter WASP-63b. Observations were conducted in the near-infrared using *HST* WFC3 G141. This study was done as a preliminary evaluation of the suitability of WASP-63b as one of the community targets for *JWST* ERS science. We have detected a muted water absorption feature at $\sim$ 1.4 μm confirming WASP-63b as a potential target for ERS science. The potential presence of an absorption feature at 1.55μm is not evidence enough to make strong conclusions about the presence of other molecules in the atmosphere, however, further observations by *JWST* would be able to identify additional spectral features that would allow us to further constrain the atmospheric composition. The observational window for observing WASP-63b with *JWST* is from September 23 – April 5.

3.7 Acknowledgments

This work is based on observations made with the NASA/ESA Hubble Space Telescope, obtained from the Data Archive at the Space Telescope Science Institute, which is operated by the Association of Universities for Research in Astronomy, Inc., under NASA contract NAS 5-26555. These observations are associated with program GO-14642. BMK acknowledges funding by HST-GO-14642.047 provided by the Space Telescope Science Institute. H.R. Wakeford acknowledges support from the NASA Postdoctoral Program, administered by USRA through a contract with NASA. Jasmina Blecic is supported by NASA trough the NASA ROSES-2016/Exoplanets Research Program, grant NNX17AC03G.

The authors acknowledge the contributions and support from members of the transiting exoplanet community who have contributed to and/or supported Program GO-14642 including: E. Agol, D. Angerhausen, T. Barman, J. Barstow, N. M. Batalha, S. Birkman, D. Charbonneau,

N. Cowan, N. Crouzet, S. Curry, J. M. Desert, D. Dragomir, J. Fortney, A. Garcia Munoz, N. Gibson, J. Gizis, T. Greene, J. Harrington, T. Kataria, E. Kempton, H. Knutson, L. Kreidberg, M. Lopez-Morales, M. Rocchetto, E. Schlawin, E. Shkolnik, A. Shporer, D. Sing, K. Todorov, and J. de Wit.

References

Abel, M., Frommhold, L., Li, X., & Hunt, K. L. C. 2012, J. Chem. Phys., 136, 044319

Ackerman, A. S. & Marley, M. S. 2001, ApJ, 556, 872

Agúndez, M., Venot, O., Iro, N., Selsis, F., Hersant, F., Hébrard, E., & Dobrijevic, M. 2012, A&A, 548, A73

Barber, R. J., Strange, J. K., Hill, C., Polyansky, O. L., Mellau, G. C., Yurchenko, S. N., & Tennyson, J. 2014, MNRAS, 437, 1828

Bean, J. L., Stevenson, K. B., Batalha, N. M., Berta-Thompson, Z., Kreidberg, L., Crouzet, N., Benneke, B., Line, M. R., Sing, D. K., Wakeford, H. R., Knutson, H. A., Kempton, E. M.-R., Désert, J.-M., Crossfield, I., Batalha, N. E., de Wit, J., Parmentier, V., Harrington, J., Moses, J. I., Lopez-Morales, M., Alam, M. K., Blecic, J., Bruno, G., Carter, A. L., Chapman, J. W., Decin, L., Dragomir, D., Evans, T. M., Fortney, J. J., Fraine, J. D., Gao, P., García Muñoz, A., Gibson, N. P., Goyal, J. M., Heng, K., Hu, R., Kendrew, S., Kilpatrick, B. M., Krick, J., Lagage, P.-O., Lendl, M., Louden, T., Madhusudhan, N., Mandell, A. M., Mansfield, M., May, E. M., Morello, G., Morley, C. V., Nikolov, N., Redfield, S., Roberts, J. E., Schlawin, E., Spake, J. J., Todorov, K. O., Tsiaras, A., Venot, O., Waalkes, W. C., Wheatley, P. J., Zellem, R. T., Angerhausen, D., Barrado, D., Carone, L., Casewell, S. L., Cubillos, P. E., Damiano, M., de Val-Borro, M., Drummond, B., Edwards, B., Endl, M., Espinoza, N., France, K., Gizis, J. E., Greene, T. P., Henning, T. K., Hong, Y., Ingalls, J. G., Iro, N., Irwin, P. G. J., Kataria, T., Lahuis, F., Leconte, J., Lillo-Box, J., Lines, S., Lothringer, J. D., Mancini, L., Marchis, F., Mayne, N., Palle, E., Rauscher, E., Roudier, G., Shkolnik, E. L., Southworth, J., Swain, M. R., Taylor, J., Teske, J., Tinetti, G., Tremblin, P., Tucker, G. S., van Boekel, R., Waldmann, I. P., Weaver, I. C., & Zingales, T. 2018, PASP, 130, 114402

Benneke, B. 2015, ArXiv e-prints

Berta, Z. K., Charbonneau, D., Désert, J.-M., Miller-Ricci Kempton, E., McCullough, P. R., Burke, C. J., Fortney, J. J., Irwin, J., Nutzman, P., & Homeier, D. 2012, ApJ, 747, 35

Blecic, J. 2016, ArXiv e-prints

Blecic, J., Harrington, J., & Bowman, M. O. 2016, ApJS, 225, 4

Borysow, A. 2002, A&A, 390, 779

Borysow, A. & Frommhold, L. 1989, ApJ, 341, 549

Borysow, A., Frommhold, L., & Moraldi, M. 1989, ApJ, 336, 495

Borysow, A., Jorgensen, U. G., & Fu, Y. 2001, J. Quant. Spec. Radiat. Transf., 68, 235

Borysow, J., Frommhold, L., & Birnbaum, G. 1988, ApJ, 326, 509

Brown, T. M. 2001, ApJ, 553, 1006

Buchner, J., Georgakakis, A., Nandra, K., Hsu, L., Rangel, C., Brightman, M., Merloni, A., Salvato, M., Donley, J., & Kocevski, D. 2014, A&A, 564, A125

Burrows, A., Marley, M., Hubbard, W. B., Lunine, J. I., Guillot, T., Saumon, D., Freedman, R., Sudarsky, D., & Sharp, C. 1997, ApJ, 491, 856

Burrows, A. & Sharp, C. M. 1999, ApJ, 512, 843

Cubillos, P., Harrington, J., Loredo, T. J., Lust, N. B., Blecic, J., & Stemm, M. 2017, AJ, 153, 3

Cubillos, P. E. 2016, ArXiv e-prints

—. 2017, ApJ, 850, 32

de Wit, J., Wakeford, H. R., Gillon, M., Lewis, N. K., Valenti, J. A., Demory, B.-O., Burgasser, A. J., Burdanov, A., Delrez, L., Jehin, E., Lederer, S. M., Queloz, D., Triaud, A. H. M. J., & Van Grootel, V. 2016, Nature, 537, 69

Deming, D., Wilkins, A., McCullough, P., Burrows, A., Fortney, J. J., Agol, E., Dobbs-Dixon, I., Madhusudhan, N., Crouzet, N., Desert, J.-M., Gilliland, R. L., Haynes, K., Knutson, H. A., Line, M., Magic, Z., Mandell, A. M., Ranjan, S., Charbonneau, D., Clampin, M., Seager, S., & Showman, A. P. 2013, ApJ, 774, 95

Evans, T. M., Sing, D. K., Wakeford, H. R., Nikolov, N., Ballester, G. E., Drummond, B., Kataria, T., Gibson, N. P., Amundsen, D. S., & Spake, J. 2016, ApJ, 822, L4

Feroz, F. & Hobson, M. P. 2008, MNRAS, 384, 449

Foreman-Mackey, D., Hogg, D. W., Lang, D., & Goodman, J. 2013, PASP, 125, 306

Fortney, J. J. 2005, MNRAS, 364, 649

Fortney, J. J., Marley, M. S., Saumon, D., & Lodders, K. 2008, ApJ, 683, 1104

Fraine, J., Deming, D., Benneke, B., Knutson, H., Jordán, A., Espinoza, N., Madhusudhan, N., Wilkins, A., & Todorov, K. 2014, Nature, 513, 526

Freedman, R. S., Lustig-Yaeger, J., Fortney, J. J., Lupu, R. E., Marley, M. S., & Lodders, K. 2014, ApJS, 214, 25

Freedman, R. S., Marley, M. S., & Lodders, K. 2008, ApJS, 174, 504

Gandhi, S. & Madhusudhan, N. 2017, MNRAS, 472, 2334

Gelman, A. & Rubin, D. B. 1992, Statistical science, 457

Greene, T. P., Line, M. R., Montero, C., Fortney, J. J., Lustig-Yaeger, J., & Luther, K. 2016, ApJ, 817, 17

Grimm, S. L. & Heng, K. 2015, ApJ, 808, 182

Guillot, T. 2010, A&A, 520, A27

Hedges, C. & Madhusudhan, N. 2016, MNRAS, 458, 1427

Hellier, C., Anderson, D. R., Collier Cameron, A., Doyle, A. P., Fumel, A., Gillon, M., Jehin, E., Lendl, M., Maxted, P. F. L., Pepe, F., Pollacco, D., Queloz, D., Ségransan, D., Smalley, B., Smith, A. M. S., Southworth, J., Triaud, A. H. M. J., Udry, S., & West, R. G. 2012, MNRAS, 426, 739

Heng, K. & Kitzmann, D. 2017, ArXiv e-prints

Hollis, M. D. J., Tessenyi, M., & Tinetti, G. 2013, Computer Physics Communications, 184, 2351

Howe, A. R. & Burrows, A. S. 2012, ApJ, 756, 176

Kilpatrick, B. M., Cubillos, P. E., Stevenson, K. B., Lewis, N. K., Wakeford, H. R., MacDonald, R. J., Madhusudhan, N., Blecic, J., Bruno, G., Burrows, A., Deming, D., Heng, K., Line, M. R., Morley, C. V., Parmentier, V., Tucker, G. S., Valenti, J. A., Waldmann, I. P., Bean, J. L., Beichman, C., Fraine, J., Krick, J. E., Lothringer, J. D., & Mandell, A. M. 2018, AJ, 156, 103

Knutson, H. A., Benneke, B., Deming, D., & Homeier, D. 2014, Nature, 505, 66

Kreidberg, L. 2015, batman: BAsic Transit Model cAlculatioN in Python, Astrophysics Source Code Library

Kreidberg, L., Bean, J. L., Désert, J.-M., Benneke, B., Deming, D., Stevenson, K. B., Seager, S., Berta-Thompson, Z., Seifahrt, A., & Homeier, D. 2014a, Nature, 505, 69

Kreidberg, L., Bean, J. L., Désert, J.-M., Line, M. R., Fortney, J. J., Madhusudhan, N., Stevenson, K. B., Showman, A. P., Charbonneau, D., McCullough, P. R., Seager, S., Burrows, A., Henry, G. W., Williamson, M., Kataria, T., & Homeier, D. 2014b, ApJ, 793, L27

Kreidberg, L., Line, M. R., Bean, J. L., Stevenson, K. B., Désert, J.-M., Madhusudhan, N., Fortney, J. J., Barstow, J. K., Henry, G. W., Williamson, M. H., & Showman, A. P. 2015a, ApJ, 814, 66

—. 2015b, ApJ, 814, 66

Kuntschner, H., Bushouse, H., Kümmel, M., & Walsh, J. R. 2009, WFC3 SMOV proposal 11552: Calibration of the G141 grism, Tech. rep.

Lecavelier Des Etangs, A., Pont, F., Vidal-Madjar, A., & Sing, D. 2008, A&A, 481, L83

Lee, J.-M., Heng, K., & Irwin, P. G. J. 2013, ApJ, 778, 97

Line, M. R., Knutson, H., Deming, D., Wilkins, A., & Desert, J.-M. 2013a, ApJ, 778, 183

Line, M. R. & Parmentier, V. 2016, ApJ, 820, 78

Line, M. R., Stevenson, K. B., Bean, J., Desert, J.-M., Fortney, J. J., Kreidberg, L., Madhusudhan, N., Showman, A. P., & Diamond-Lowe, H. 2016, AJ, 152, 203

Line, M. R., Wolf, A. S., Zhang, X., Knutson, H., Kammer, J. A., Ellison, E., Deroo, P., Crisp, D., & Yung, Y. L. 2013b, ApJ, 775, 137

Lodders, K. 2009, Exoplanet Chemistry (Wiley-VCH)

MacDonald, R. J. & Madhusudhan, N. 2017, ArXiv e-prints

Mandel, K. & Agol, E. 2002, ApJ, 580, L171

Marley, M. S., Gelino, C., Stephens, D., Lunine, J. I., & Freedman, R. 1999, ApJ, 513, 879

Marley, M. S., Saumon, D., Guillot, T., Freedman, R. S., Hubbard, W. B., Burrows, A., & Lunine, J. I. 1996, Science, 272, 1919

Marley, M. S., Seager, S., Saumon, D., Lodders, K., Ackerman, A. S., Freedman, R. S., & Fan, X. 2002, ApJ, 568, 335

McCullough, P. & MacKenty, J. 2012, Considerations for using Spatial Scans with WFC3, Tech. rep.

McKay, C. P., Pollack, J. B., & Courtin, R. 1989, Icarus, 80, 23

Mordasini, C., van Boekel, R., Mollière, P., Henning, T., & Benneke, B. 2016, ApJ, 832, 41

Morley, C. V., Fortney, J. J., Marley, M. S., Zahnle, K., Line, M., Kempton, E., Lewis, N., & Cahoy, K. 2015, ApJ, 815, 110

Morley, C. V., Knutson, H., Line, M., Fortney, J. J., Thorngren, D., Marley, M. S., Teal, D., & Lupu, R. 2017, AJ, 153, 86

Moses, J. I., Madhusudhan, N., Visscher, C., & Freedman, R. S. 2013, ApJ, 763, 25

Moses, J. I., Visscher, C., Fortney, J. J., Showman, A. P., Lewis, N. K., Griffith, C. A., Klippenstein, S. J., Shabram, M., Friedson, A. J., Marley, M. S., & Freedman, R. S. 2011, ApJ, 737, 15

Parmentier, V., Fortney, J. J., Showman, A. P., Morley, C., & Marley, M. S. 2016, ApJ, 828, 22

Parmentier, V., Line, M. R., Bean, J. L., Mansfield, M., Kreidberg, L., Lupu, R., Visscher, C., Desert, J.-M., Fortney, J. J., Deleuil, M., Arcangeli, J., Showman, A. P., & Marley, M. S. 2018, ArXiv e-prints

Richard, C., Gordon, I. E., Rothman, L. S., Abel, M., Frommhold, L., Gustafsson, M., Hartmann, J.-M., Hermans, C., Lafferty, W. J., Orton, G. S., Smith, K. M., & Tran, H. 2012, J. Quant. Spec. Radiat. Transf., 113, 1276

Rothman, L. S., Gordon, I. E., Babikov, Y., Barbe, A., Chris Benner, D., Bernath, P. F., Birk, M., Bizzocchi, L., Boudon, V., Brown, L. R., Campargue, A., Chance, K., Cohen, E. A., Coudert,

L. H., Devi, V. M., Drouin, B. J., Fayt, A., Flaud, J.-M., Gamache, R. R., Harrison, J. J., Hartmann, J.-M., Hill, C., Hodges, J. T., Jacquemart, D., Jolly, A., Lamouroux, J., Le Roy, R. J., Li, G., Long, D. A., Lyulin, O. M., Mackie, C. J., Massie, S. T., Mikhailenko, S., Müller, H. S. P., Naumenko, O. V., Nikitin, A. V., Orphal, J., Perevalov, V., Perrin, A., Polovtseva, E. R., Richard, C., Smith, M. A. H., Starikova, E., Sung, K., Tashkun, S., Tennyson, J., Toon, G. C., Tyuterev, V. G., & Wagner, G. 2013, J. Quant. Spec. Radiat. Transf., 130, 4

Rothman, L. S., Gordon, I. E., Barbe, A., Benner, D. C., Bernath, P. F., Birk, M., Boudon, V., Brown, L. R., Campargue, A., Champion, J.-P., Chance, K., Coudert, L. H., Dana, V., Devi, V. M., Fally, S., Flaud, J.-M., Gamache, R. R., Goldman, A., Jacquemart, D., Kleiner, I., Lacome, N., Lafferty, W. J., Mandin, J.-Y., Massie, S. T., Mikhailenko, S. N., Miller, C. E., Moazzen-Ahmadi, N., Naumenko, O. V., Nikitin, A. V., Orphal, J., Perevalov, V. I., Perrin, A., Predoi-Cross, A., Rinsland, C. P., Rotger, M., Šimečková, M., Smith, M. A. H., Sung, K., Tashkun, S. A., Tennyson, J., Toth, R. A., Vandaele, A. C., & Vander Auwera, J. 2009, J. Quant. Spec. Radiat. Transf., 110, 533

Rothman, L. S., Gordon, I. E., Barber, R. J., Dothe, H., Gamache, R. R., Goldman, A., Perevalov, V. I., Tashkun, S. A., & Tennyson, J. 2010, J. Quant. Spec. Radiat. Transf., 111, 2139

Saumon, D. & Marley, M. S. 2008, ApJ, 689, 1327

Sharp, C. M. & Burrows, A. 2007, ApJS, 168, 140

Showman, A. P., Fortney, J. J., Lian, Y., Marley, M. S., Freedman, R. S., Knutson, H. A., & Charbonneau, D. 2009, ApJ, 699, 564

Sing, D. K., Fortney, J. J., Nikolov, N., Wakeford, H. R., Kataria, T., Evans, T. M., Aigrain, S., Ballester, G. E., Gibson, N. P., Henry, G. W., Huitson, C. M., Knutson, H. A., Lecavelier Des Etangs, A., Pont, F., Showman, A. P., Vidal-Madjar, A., Williamson, M. H., & Wilson, P. A. 2016, Nature, 529, 59

Stevenson, K. B. 2016, ApJ, 817, L16

Stevenson, K. B., Désert, J.-M., Line, M. R., Bean, J. L., Fortney, J. J., Showman, A. P., Kataria, T., Kreidberg, L., McCullough, P. R., Henry, G. W., Charbonneau, D., Burrows, A., Seager, S., Madhusudhan, N., Williamson, M. H., & Homeier, D. 2014, Science, 346, 838

Stevenson, K. B., Lewis, N. K., Bean, J. L., Beichman, C., Fraine, J., Kilpatrick, B. M., Krick, J. E., Lothringer, J. D., Mandell, A. M., Valenti, J. A., Agol, E., Angerhausen, D., Barstow, J. K., Birkmann, S. M., Burrows, A., Charbonneau, D., Cowan, N. B., Crouzet, N., Cubillos, P. E., Curry, S. M., Dalba, P. A., de Wit, J., Deming, D., Désert, J.-M., Doyon, R., Dragomir, D., Ehrenreich, D., Fortney, J. J., García Muñoz, A., Gibson, N. P., Gizis, J. E., Greene, T. P., Harrington, J., Heng, K., Kataria, T., Kempton, E. M.-R., Knutson, H., Kreidberg, L., Lafrenière, D., Lagage, P.-O., Line, M. R., Lopez-Morales, M., Madhusudhan, N., Morley, C. V., Rocchetto, M., Schlawin, E., Shkolnik, E. L., Shporer, A., Sing, D. K., Todorov, K. O., Tucker, G. S., & Wakeford, H. R. 2016, PASP, 128, 094401

Swain, M. R., Line, M. R., & Deroo, P. 2014, ApJ, 784, 133

Tennyson, J. & Yurchenko, S. N. 2012, MNRAS, 425, 21

Tennyson, J., Yurchenko, S. N., Al-Refaie, A. F., Barton, E. J., Chubb, K. L., Coles, P. A., Diamantopoulou, S., Gorman, M. N., Hill, C., Lam, A. Z., Lodi, L., McKemmish, L. K., Na, Y., Owens, A., Polyansky, O. L., Rivlin, T., Sousa-Silva, C., Underwood, D. S., Yachmenev, A., & Zak, E. 2016, Journal of Molecular Spectroscopy, 327, 73

Tinetti, G., Tennyson, J., Griffith, C. A., & Waldmann, I. 2012, Philosophical Transactions of the Royal Society of London Series A, 370, 2749

Toon, O. B. & Ackerman, T. P. 1981, Appl. Opt., 20, 3657

Venot, O., Hébrard, E., Agúndez, M., Dobrijevic, M., Selsis, F., Hersant, F., Iro, N., & Bounaceur, R. 2012, A&A, 546, A43

Wakeford, H. R., Sing, D. K., Evans, T., Deming, D., & Mandell, A. 2016, ApJ, 819, 10

Wakeford, H. R., Stevenson, K. B., Lewis, N. K., Sing, D. K., López-Morales, M., Marley, M., Kataria, T., Mandell, A., Ballester, G. E., Barstow, J., Ben-Jaffel, L., Bourrier, V., Buchhave, L. A., Ehrenreich, D., Evans, T., García Muñoz, A., Henry, G., Knutson, H., Lavvas, P., Lecavelier des Etangs, A., Nikolov, N., & Sanz-Forcada, J. 2017, ApJ, 835, L12

Waldmann, I. P. 2016, ApJ, 820, 107

Waldmann, I. P., Rocchetto, M., Tinetti, G., Barton, E. J., Yurchenko, S. N., & Tennyson, J. 2015a, ApJ, 813, 13

Waldmann, I. P., Tinetti, G., Rocchetto, M., Barton, E. J., Yurchenko, S. N., & Tennyson, J. 2015b, ApJ, 802, 107

Chapter 4

Evaluating Climate Variability of the Canonical Hot Jupiters HD 189733b & HD 209458b

This Chapter is based on work performed with coauthors and has been submitted to the Astronomical Journal as Kilpatrick et al. (2019). In chapter 2 my foundation of *Spitzer* data analysis skills were built. In this chapter I take the next step towards high resolution looks at exoplanet atmospheres. As previously stated, we can not spatially resolve transiting exoplanets. However, through novel observational strategies and analysis techniques we can begin to probe physical processes that manifest on small length scales. Here we accomplish several parallel objectives

- Search for temporal variability in eclipse depth as a probe of atmospheric dynamics.
- Motivate eclipse mapping by providing evidence for non-uniform thermal distributions.
- Develop analysis pipelines for handling large amounts of data.

4.1 Abstract

Here we present the analysis of multi-epoch secondary eclipse observations of HD 189733b and HD 209458b as a probe of temporal variability in the planetary climate using both *Spitzer* channels 1 and 2 (3.6 and 4.5 μm). We expect hot Jupiter atmospheres to be dynamic environments

exhibiting time varying weather. However, it is uncertain to what extent temporal variability will be observable when considering disc integrated observations. Constraining temporal variability will inform models and identify physical processes occurring at either length scales too small to directly observe or at pressure levels that are inaccessible to transit observations. We do not detect statistically significant variability and are able to place useful upper limits on the IR variability amplitudes in these atmospheres. There are very few planets with multi-epoch observations at the required precision to probe variability in dayside emission. The observations considered in this study span several years, providing insight into temporal variability at multiple timescales. In the case of HD 189733b, the best fit eclipse depths for the channel 2 observations exhibit a scatter of 102 ppm about a median depth of 1827 ppm and in channel 1 exhibit a scatter of 88 ppm about a median depth of 1481 ppm. For HD 209458b, the best fit eclipse depths for the channel 2 observations exhibit a scatter of 22 ppm about a median depth of 1406 ppm and in channel 1 exhibit a scatter of 131 ppm about a median depth of 1092 ppm. The precision and scatter in these observations allow us to constrain variability to less than (5.6% and 6.0%) and (12% and 1.6%) for channels (1,2) of HD 189733b and HD 209458b respectively. We compare the results of our observations to general circulation models (GCMs) and find that periodic changes in eclipse depth due to wave dynamics are expected but only at the magnitude of a per cent or two at the wavelengths probed here. There is a difference in the best fit eclipse timing compared to the predicted time. HD 209458b consistently shows an offset in the eclipse time of 155 $\pm$ 25 seconds in Channel 1 and 129 $\pm$ 16 seconds in Channel 2. HD 189733b shows an offset of 28 $\pm$ 27 seconds in Channel 1 and 35 $\pm$ 13 seconds in Channel 2. The delay in eclipse timing for HD 209458b is consistent with an offset hotspot as predicted by GCMs and confirmed in previous phase curve observations while the results for HD 189733b are smaller than expected in comparison to GCM predictions and previous observations but within statistical uncertainty. The results of this study provide evidence of a non - uniform dayside thermal distribution for HD 209458b and show no evidence for measurable variability in eclipse depths thereby motivating and justifying the utilization of multi - epoch eclipse observations to gain the required precision to map the dayside temperature structure via eclipse mapping.

4.2 Introduction

Studying exoplanet atmospheres is challenging since we often are not able to spatially resolve them. Transiting exoplanets provide a unique opportunity to study exoplanet atmospheres in spite of this challenge. Disc integrated secondary eclipse observations provide valuable information on temperature, albedo, and chemical composition averaged over the entire hemisphere. Primary transits give a limb averaged atmospheric molecular spectrum and pressure - temperature profile. However, we must employ other novel techniques to begin to probe physical and chemical processes and structures at smaller scales. Temporal variability is one way to probe weather features and their their movements without spatially resolving them. Variability is also a tool to study portions of the atmosphere inaccessible via other observational techniques. Transmission spectroscopy observations in the near infrared typically probe millibar pressure levels high in the atmosphere. Processes deeper in the atmosphere are obscured due to the long path lengths of the transit geometry. Time varying changes in emission may be indicative of processes occurring deeper in the atmosphere and provide a unique opportunity to observe them.

Close-in giant planets (hot Jupiters) are unique objects with which to study atmospheric dynamics. They are assumed to be tidally locked based on their short orbital periods (¡5 days) and minimal separation from their host stars. As a result, they experience a constant radiative forcing on their permanent dayside. The combination of the rotation rate and radiative forcing of these planets are predicted to produce large scale weather structures unlike anything in our solar system.

There have been many efforts to model the circulation and temperature structure of hot Jupiters with many of these efforts based on the properties of the two most well studied targets, HD 189733b and HD 209458b (HD 189733b& HD 209). Simulations by Showman & Guillot (2002); Cho et al.

(2003) and Menou et al. (2003) predicted that the Rossby deformation radius and Rhines scale of hot Jupiters should be comparable to the planetary radius resulting in atmospheric dynamics comprised of a few jets and large scale polar vortices. They predicted that vortices would be large enough that their migration could have an affect on the observed eclipse depth as great as 20% in some cases. Later simulations by Showman et al. (2009) predicted far more stable atmospheric structures. Variability was predicted to be less than several percent for HD 189733b at 8 μm and the result of wave dynamics deep in the atmosphere rather than migrating vortices.

Agol et al. (2010a) observationally probed model predictions with a multi - epoch set of transit and eclipse observations of HD 189733b at 8 μm. The results of that work placed an upper limit on eclipse depth variability at 2.7%, effectively ruling out larger predictions. There have been few other attempts to study temporal variability due to the lack of multiple observations over a sufficient temporal baseline.

We choose as our targets for this study HD 189733b and HD 209458b both because of their suitability for observations with the *Spitzer* observatory and because they are the only targets with a large number of observations with a single instrument spanning a number of years. These two planets are the most well studied and characterized exoplanets to date. Both orbit bright stars, $K_{\rm mag}$ of 5.5 and 6.3 for HD 189733b and HD 209458b respectively, making them ideal targets for characterization and have previously observed secondary eclipse depths ¿1000 ppm in both warm *Spitzer* channels 1 and 2.

HD 189733b is arguably the most thoroughly studied exoplanet. It has been observed with photometric (e.g. Ehrenreich et al. 2007; Désert et al. 2009, 2011b) and spectroscopic (e.g. Gibson et al. 2012) transits as well as secondary eclipse (e.g. Charbonneau et al. 2008a; Agol et al. 2010a) and phase curve (Knutson et al. 2007, 2009, 2012) observations across a multitude of wavelengths. In addition to full orbit phase curves at multiple wavelengths, it is the only planet to have been mapped via the eclipse mapping technique (Majeau et al. 2012; de Wit et al. 2012; Rauscher et al. 2018). HD 209458b was the first transiting exoplanet discovered (Charbonneau et al. 2000). It has also been observed in both transit and eclipse geometries photometrically (e.g. Charbonneau et al. 2008b; Diamond-Lowe et al. 2014) and spectroscopically (e.g. Deming et al. 2013; Line et al. 2016) , as well as full orbit phase curve observations (Zellem et al. 2014).

The large amount of observational and theoretical effort invested into these two canonical hot Jupiters make them perfect choices for a study of this nature. There are eclipse observations from multiple programs spanning years from which to build the necessary temporal baseline. Additionally, their orbital properties are well studied and well constrained allowing for the detection of small signals in their lightcurves due to planetary thermal structure that can be clearly distinguished from other potential sources such as orbital eccentricity.

Understanding variability will be essential in current and future attempts to leverage multiple epoch observations to build precision for high resolution techniques such as eclipse mapping. Eclipse mapping (Majeau et al. 2012; de Wit et al. 2012) uses the deviations to the shape of ingress and egress caused by a non uniform dayside temperature distribution to create two dimensional thermal maps. In general, one needs $\sim$10 points over the ingress/egress with a precision of at least a 10th of the eclipse depth to achieve the necessary resolution to map hot Jupiters. The only way to achieve that precision with current observatories is to stack multiple observations. In the *James Webb Space Telescope (JWST)* era, observing time will be expensive and full orbit phase curves may prove too costly. However, mapping may be done much more efficiently with as little as two eclipse observations. Understanding temporal variability then is crucial in knowing if stacking multi-epoch observations is justifiable in that context. The observations considered here give the best current insight into orbit to orbit changes in hot Jupiter atmospheres.

4.3 Observations

Here we consider all existing secondary eclipse observations of HD 189733b and HD 209458b in channels 1 and 2 (3.6 or 4.5 μm bandpass) . The observations analyzed here are part of Programs 60021 (PI: H. Knutson), 10103 (PI: N. Lewis), 90186 (PI: K. Todorov), and 70100 (PI: M. Swain). The details of each Astronomical Observing Request (AOR) are displayed in Table 4.3 and 4.4.1.

All of the observations were carried out in sub-array mode (32×32 pixels, $39"\times39"$). Observations in Program 10103 utilize a 30 minute peak-up observation preceding them to stabilize the image on the detector 'sweet spot' and decreases the likelihood of a ramp in the data (Ingalls et al. 2012). Program 60021 observations are full orbit phase curves from which we extract the AORs containing the eclipse from the larger data set. Both HD 189733 and HD 209458 are bright targets with K_{mag} of 5.5 and 6.3 respectively. As a result, frame times for all of the observations are 0.1 seconds. The two exceptions are the observations of HD 209458b in channel 2 that were conducted with a 0.4 second frame time and the observations of HD 189733b from program 70100 that were conducted such that the stellar centroid was near the corner of the pixel so that a longer (0.4 s) exposure time could be used. This technique proved problematic in that the systematics were not easily corrected with existing techniques and, as a result, several of these observations were discarded from this study.

Table 4.1. Summary of Observations
HD 189733b

Program	AOR	Channel	Date
10103	50495232	1	1/7/14
10103	50494464	1	1/14/14
10103	50493696	1	1/25/14
10103	50493184	1	7/15/14
60021	41592320	1	12/28/10
60021	41591296	1	12/30/10
70100	40150528	1	11/24/10
70100	40151040	1	1/3/11
70100	40151296	1	6/23/11
70100	40152064	1	6/27/11
10103	50489344	2	1/12/14
10103	50488832	2	1/18/14
10103	50488576	2	7/13/14
10103	50488320	2	7/26/14
10103	50488064	2	8/11/14
60021	38390784	2	12/22/09

Table 4.1 (cont'd)

Program	AOR	Channel	Date
60021	38390016	2	12/24/09

4.4 Data Analysis Methods

4.4.1 Photometric Extraction

For each AOR we began with Basic Calibrated Data (BCD) available on the Spitzer Heritage Archive. Each BCD file contains a cube of 64 frames of 64×64 pixels. Each set of 64 images comes as a single FITS file with a time stamp corresponding to the start of the first image. We determine the time of each frame in the set by adding the appropriate multiple of the frame time to the time stamp of the first image. Each frame was corrected for bad pixels or NaN values by masking the invalid pixels. Each frame is background subtracted based on the median pixel value outside of a 10 x 10 pixel box around the stellar centroid. Pixel values in the background region that deviate from the mean by more than 5 σ are clipped and the median value remaining is taken to be the background. Stellar centroid positions for each frame are determined by a first moment center of mass calculation:

$$x_{\rm cen} = \frac{\sum_{j,k}(I_{jk}j)}{\sum_{j,k} I_{jk}}; \qquad y_{\rm cen} = \frac{\sum_{j,k}(I_{jk}k)}{\sum_{j,k} I_{jk}}. \tag{4.1}$$

We perform two-dimensional Gaussian Centroiding as well but find the first moment calculation to be more stable and provides less scatter in the extracted photometry.

Table 4.2. Summary of Observations
HD 209458b

Program	AOR	Channel	Date
60021	41629440	1	1/12/11
60021	41628416	1	1/15/11
90186	48013824	1	8/28/13
10103	50496512	1	1/19/14
10103	50496256	1	2/27/14
10103	50496000	1	2/6/14
10103	50495744	1	8/22/14
10103	50495488	1	8/29/14
10103	50494976	1	9/5/14
10103	50494208	1	9/27/14
10103	50493440	1	1/24/15
10103	50492928	1	1/28/15
10103	50490880	2	1/26/14
10103	50490624	2	2/2/14
10103	50490368	2	8/19/14
10103	50490112	2	8/26/14

Table 4.2 (cont'd)

Program	AOR	Channel	Date
10103	50489856	2	9/12/14
10103	50489088	2	1/7/14
90186	48014336	2	8/31/13
60021	38703616	2	1/21/10

The noise pixel parameter ($\tilde{\beta}$) (Lewis et al. 2013; Kilpatrick et al. 2017) is calculated for each frame as

$$\tilde{\beta} = \frac{\left(\sum P_i\right)^2}{\sum \left(P_i^2\right)}, \tag{4.2}$$

where each P_i is the response measured in each pixel across the frame. We also save the 5 x 5 array of background subtracted pixel values about the stellar centroid for each frame. Each array is normalized such that they sum to one. We then perform aperture photometry about the stellar centroid using the aperture_photometry function from the Astropy package Photutils. Circular apertures of fixed radii ranging from 1.8 - 2.8 pixels and variable radii apertures ranging from $\beta_{\text{pix}}\times$ {0.7...1.2} and $\beta_{\text{pix}}+$ {-0.6...1.4}. The resultant time series photometry is then filtered by removing any points that deviate by more than 3 σ from the median values of flux or x,y position.

4.4.2 Systematics Correction and Model Fitting

The intrapixel sensitivity variation (Ingalls et al. 2012), the change in measured flux as a function of stellar centroid position and methods of correction, are well documented (e.g. Ingalls et al. 2016; Kilpatrick et al. 2017). Here, we employ two independent methods of correction for this systematic variation; the Nearest Neighbors method (NNBR), otherwise known as Gaussian Kernel Regression with data (Lewis et al. 2013) and Pixel Level Decorrelation (PLD) (Deming et al. 2015).

Each eclipse fit was based on the model of Mandel & Agol (2002) for a uniform occultation implemented in python by the BATMAN package (Kreidberg 2015). The orbital, stellar, and planetary parameters listed in table 5.1 were used as input fixed parameters to the model. *Spitzer* IRAC data is known to have an exponential ramp in flux over the first 30–60 minutes of observing; however the peak-up technique has alleviated this problem to some extent (Kilpatrick et al. 2017; Ingalls et al. 2012). As a precaution, each data set was fit in several ways: without alteration, trimmed at 20 minutes from the beginning of the observation, and with an exponential ramp model of the form

$$R_{model} = 1 - a_1 \times e^{(-\frac{t}{a_2})}. \quad (4.3)$$

PLD has a quadratic visit long temporal variation included in all cases rather than the exponential ramp and combines the systematics and astrophysical models by a linear expression

$$\Delta S^t = \sum_{i=1}^{n} c_i \hat{P}_i^t + DE(t) + ft + gt^2 + h, \quad (4.4)$$

where the $\hat{P}_i^t$'s are the response of the i^{th} pixel in a 3×3 grid around the centroid of the image and $DE(t)$ is the eclipse model.

For each AOR the eclipse model and systematics model were combined and best fit values for all free parameters were determined using a non-linear, least squares fitting algorithm. The standard deviation of the normalized residuals (SDNR) was used as a metric for selecting the best fit out of the 30 different apertures for each AOR. The Bayesian Information Criterion (BIC) was used to determine the appropriate treatment between various trimming and ramp model options. We find that no trimming or exponential ramp are necessary in all cases of Channel 2 observations and the quadratic ramp with PLD is favored in all Channel 1 observations. The results from the best fit aperture were passed to a Markov Chain Monte Carlo implemented by emcee (Foreman-Mackey et al. 2013) to derive uncertainties of each free parameter. We use a number of walkers at least twice the number of free parameters and run for 10^5 steps per walker before testing for convergence using Gelman Rubin statistics with a threshold for acceptance of 1.1 (Gelman & Rubin 1992).

[]

Table 4.3. Ephemerides

Parameter	HD 189733b	HD 209458b
$T_\star$	5040±50	6065±50
$M_\star$ (M_{Sun})	0.806±0.048	1.131±0.026
$R_\star$ (R_{Sun})	0.756±0.018	1.155±0.015
M_p (M_{Jup})	1.144±0.056	0.690±0.024
R_p (R_{Jup})	1.138±0.027	1.359±0.015
$R_p/R_\star$	$0.024122\pm5.8\times10^{-5}$	$0.014607\pm2.4\times10^{-5}$
log(g)	3.339±0.03	2.969±0.0187
Period	$2.21857567\pm1.5\times10^{-7}$	$3.52474859\pm 3.8\times10^{-7}$
i (°)	85.7100±0.0023	86.710± 0.05
msin i	1.140 ±0.056	0.689±0.024
$a/R_\star$	8.84±0.27	8.81±0.186

4.5 Results

Here we present the best fit eclipse depths and center of eclipse times, along with their corresponding uncertainty, for each of the observations. The results presented in Table 4.4 are derived using the PLD method with a quadratic temporal term. No additional trimming or ramps are modeled. The best fit aperture was consistently a fixed radius aperture between 2.2 and 2.4 pixels. We include in Table 4.4 the standard deviation of the normalized residuals (SDNR) and the $\beta_{\rm red}$ factor, as defined in Gillon et al. (2010), as a measure of correlated noise remaining in the data after systematic corrections. Included in Figure 4.1 are representative fits for each of the two targets in each of the two channels with the systematics removed and binned at two minute intervals. In the case of HD 189733b, the best fit eclipse depths for the channel 2 observations exhibit a scatter of 102 ppm about a median depth of 1827 ppm and in channel 1 exhibit a scatter of 88 ppm about a median depth of 1481 ppm. For HD 209458b, the best fit eclipse depths for

Table 4.4. Results of Best Fit Eclipse Depth and Time

AOR	Eclipse Depth (ppm)	Eclipse Time O-C (min)	SDNR	$\beta_{\rm red}$
		HD 209458b Ch 2		
38703616	1370 ± 37	2.22 ± 1.04	0.003240	1.43
48014336	1401 ± 42	1.44 ± 0.83	0.003085	1.17
50489088	1424 ± 60	3.03 ± 0.90	0.003085	1.16
50490880	1380 ± 58	1.62 ± 0.79	0.003053	1.27
50490624	1443 ± 56	3.14 ± 0.82	0.003060	1.27
50490368	1417 ± 45	2.60 ± 0.96	0.003151	1.05
50490112	1420 ± 52	2.81 ± 0.72	0.003125	1.18
50489856	1424 ± 47	1.57 ± 0.65	0.003116	1.09
		HD 209458b Ch 1		
48013824	1050 ± 73	4.37 ± 1.61	0.004995	2.59
50496512	909 ± 60	1.48 ± 1.27	0.004873	1.99
50496000	1162 ± 77	3.38 ± 1.39	0.004834	1.96
50496256	1209 ± 67	2.81 ± 1.13	0.004805	1.95
50495744	845 ± 92	4.21 ± 1.84	0.005055	2.29
50495488	1008 ± 76	1.81 ± 1.37	0.004946	1.78
50494976	1049 ± 78	2.48 ± 1.30	0.004898	2.03
50494208	1209 ± 72	1.61 ± 1.36	0.0049606	2.03
50493440	1301 ± 76	2.20 ± 1.15	0.004983	1.87
50492928	994 ± 105	6.82 ± 2.61	0.004939	2.74
41629440	1216 ± 77	1.28 ± 2.32	0.006171	4.14
41628416	1128 ± 72	1.99 ± 2.72	0.006168	3.68
		HD 189733b Ch 2		
38390784	1812 ± 50	1.52 ± 0.69	0.004596	1.65
38390016	1806 ± 64	0.31 ± 0.97	0.004698	1.74

the channel 2 observations exhibit a scatter of 22 ppm about a median depth of 1406 ppm and in channel 1 exhibit a scatter of 131 ppm about a median depth of 1092 ppm.

Table 4.4 (cont'd)

AOR	Eclipse Depth (ppm)	Eclipse Time O-C (min)	SDNR	$\beta_{\rm red}$
50489344	1716 ± 55	0.96 ± 0.45	0.004631	1.06
50488832	1815 ± 61	-0.37 ± 0.61	0.004606	1.41
50488576	1984 ± 75	0.31 ± 0.64	0.004630	1.31
50488320	1774 ± 50	0.24 ± 0.55	0.004572	1.12
50488064	2016 ± 65	-0.02 ± 0.48	0.004654	1.00
		HD 189733b Ch 1		
41592320	1574 ± 305	1.40 ± 6.0	0.004228	4.55
41591296	1431 ± 86	0.29 ± 1.74	0.003382	2.13
40152064	1271 ± 310	0.16 ± 4.08	0.001708	3.76
50495232	1514 ± 105	-0.37 ± 1.35	0.003370	1.51
50494464	1473 ± 73	0.81 ± 0.93	0.003298	1.50
50493696	1498 ± 53	0.80 ± 0.67	0.003266	1.54
50493184	1491 ± 115	-0.74 ± 1.37	0.003306	1.85

As shown in Figures 4.2 and 4.3, the scatter in the data is consistent with the uncertainty in each measurement in all cases except for the channel 1 HD209 data. Given the number of observations at the achieved precision, we would expect the resultant eclipse depths to represent a sampling of a distribution represented by the shaded areas in Figures 4.2 and 4.3. The channel 1 observations of HD209, which exhibit more scatter than indicated by the error bars, is thought to be due to unresolved systematics. This is further supported by the larger values of $\beta_{\rm red}$ in channel 1 observations in comparison to channel 2.

4.5.1 Constraints on Temporal Variability

As a probe of periodic variability in the eclipse depths we calculate the absolute difference in eclipse depths for each pair of observations. The absolute difference is plotted against the time between observations. Small numbers of observations do not lend themselves to more thorough methods of detecting power at certain time scales such as Lomb-Scargle periodograms, however, this simple approach would show a spike in absolute difference at any relevant timescale. The apparent random scatter of the data points in Figure 4.4 does not indicate any periodic structure in any of the observations. Comparing the standard deviation and the magnitude of the eclipse depths

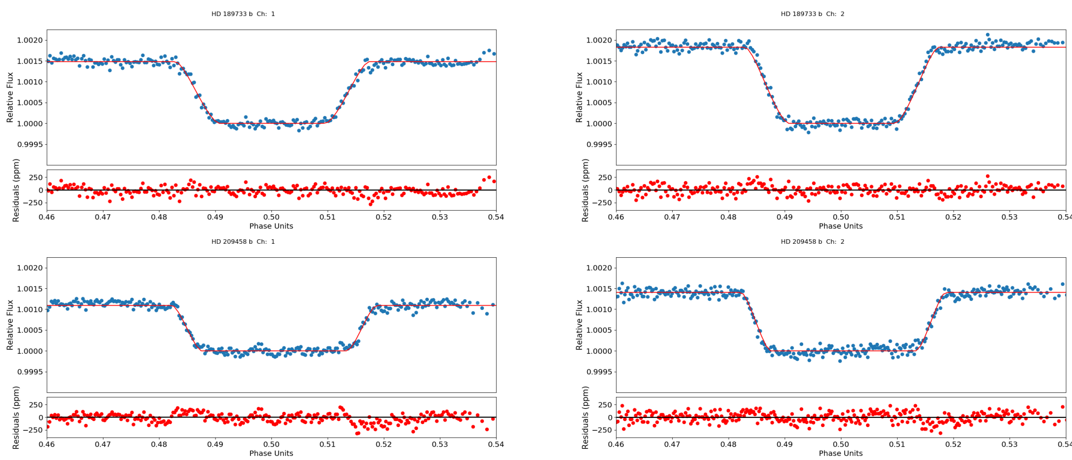

Figure 4.1 Each of the above panels shows the lightcurve after all data points for each planet/channel are binned to ∼1 minute bins with systematics removed. The best fit model based on the weighted averages as stated in Section 4.5 is plotted in red. The residuals from each individual fit are combined and binned at the same interval.

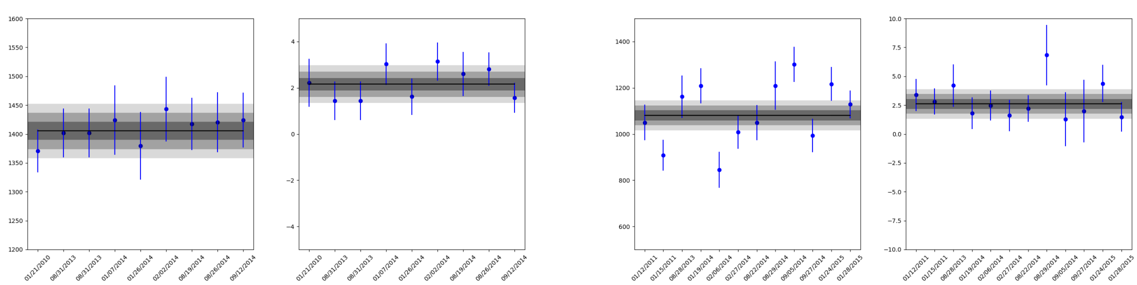

Figure 4.2 Eclipse Depths and timing for the 9 Ch 2 Eclipses (top) and the the 12 Ch 1 Eclipses (bottom) of HD 209458b with multiple methodologies. The shaded gray areas represent the 1,2 and 3 sigma areas of a distribution derived from the mean and uncertainty of the measurements as a whole.

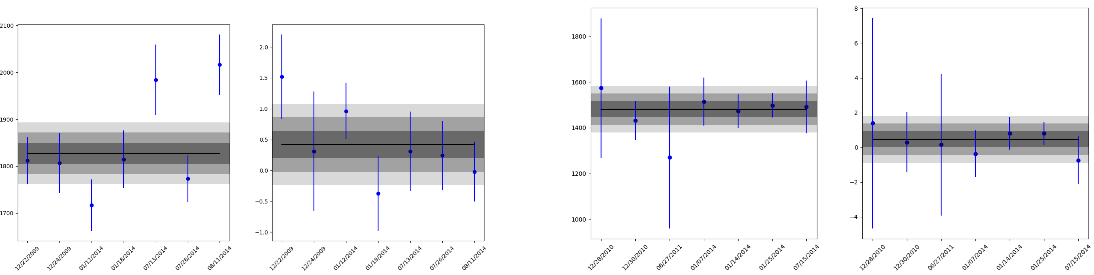

Figure 4.3 Eclipse Depths and timing for the 7 Ch 2 Eclipses (top) and the the 7 Ch 1 Eclipses (bottom) of HD 189733b with multiple methodologies. The shaded gray areas represent the 1,2 and 3 sigma areas of a distribution derived from the mean and uncertainty of the measurements as a whole.

allows us to constrain variability to less than (5.6% and 6.0%) and (12% and 1.6%) for channels (1,2) of HD 189733b and HD 209458b respectively.

4.5.2 Stellar Variability

Stellar variability in the form of spots or plages can affect the measured planetary transit signal, potentially altering one's interpretation of its atmospheric composition, particularly for bright targets with large transit signals (Pont et al. 2008; Silva-Valio 2008; Czesla et al. 2009; Wolter et al. 2009; Agol et al. 2010b; Berta et al. 2011; Carter et al. 2011; Désert et al. 2011a; Sing et al. 2011; Fraine et al. 2014; McCullough et al. 2014; Oshagh et al. 2014; Damasso et al. 2015; Barstow et al. 2015; Zellem et al. 2015, 2017; Cauley et al. 2017, 2018; Rackham et al. 2017, 2018, 2019; Morris et al. 2018). HD 189733 is an active K0 star which has been observed to vary by as much as $\pm$ 1.5% at visible wavelengths with a rotation period of 11.95 days (Knutson et al. 2012, and references within) whose variability potentially impacts the observed transit depth of the planet (McCullough et al. 2014; Knutson et al. 2012). Although the amplitudes of these variations are reduced as our Spitzer/IRAC observations are in the infrared (Oshagh et al. 2014; Rackham et al. 2017; Morris et al. 2018) and of eclipses (Zellem et al. 2017), we examine the amplitude of these changes in comparison to the scatter and uncertainty in our eclipse depth measurements.

We employ ground-based monitoring spanning the 2009 to 2014 observing seasons with the Tennessee State University 0.8 m Automated Photoelectric Telescope (APT) at Fairborn

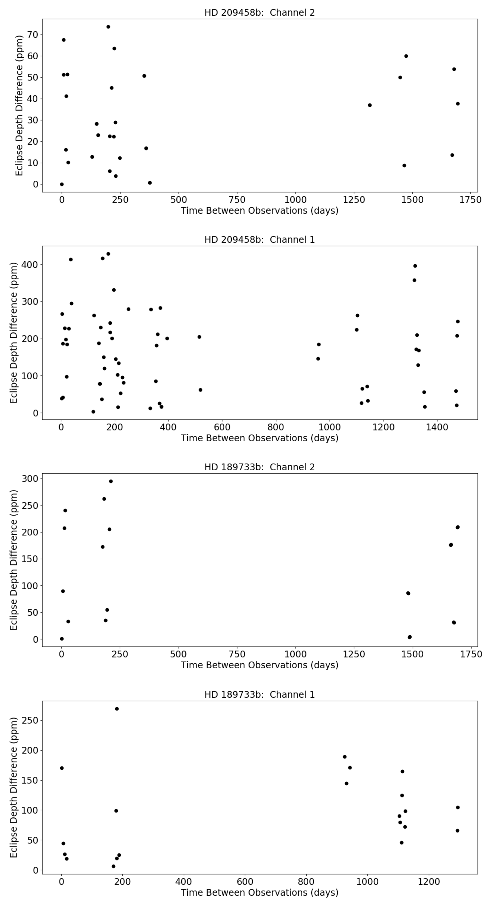

Figure 4.4 The absolute difference in eclipse depth for each pair of observations are plotted as a function of the time between observations. Any periodic variability would manifest as peaks in this plot. The data appears to be randomly scattered suggesting that any variability in the eclipse depths is likely due to precision limitations rather than any periodic variability in the astrophysical signal.

Observatory in southern Arizona (e.g., Henry 1999; Eaton et al. 2003, Fig. 4.5). However, most of our *Spitzer* /IRAC observations occur outside the APT observing season (Fig. 4.5). While previous studies have interpolated APT monitoring to their *Spitzer* observations (Knutson et al. 2012) using an activity model (Aigrain et al. 2012) to fit the APT data and interpolated it to their *Spitzer* observations, we conservatively take the peak-to-trough Strömgren b+y variability observed by APT from 2009 to 2014 (4.7%) and interpolate it to the infrared using the scaling presented in Knutson et al. (2012) (1.6%). Using Equation 7 in Zellem et al. (2017), we estimate the effect of HD 189733's variability on the observed eclipse depths and find that variability does not statistically impact HD 189733b's eclipse depths as the changes in its measured eclipse depths induced by variability are less than the measurement uncertainties of the eclipses themselves (Fig. 4.5).

4.6 Discussion

4.6.1 Model Predictions

Given that our assessment of atmospheric variability is in direct relation to the planet's atmospheric dynamics, we compare our *Spitzer* variability estimates to predictions from three-dimensional general circulation models (GCMs). In particular, we use GCM simulations of HD 189733b from Showman et al. (2009) and HD 209458b from Kataria et al. (2016), respectively, which utilize the Substellar and Planetary Radiation and Circulation (SPARC) model (Showman et al. 2009). The SPARC model couples the general circulation model maintained at the Massachusetts Institute of Technology (the MITgcm, Adcroft et al. (2004)) with a plane-parallel, two-stream version of the multi-stream radiation code developed by Marley & McKay (1999). Further details on these models are provided in Showman et al. (2009)), Kataria et al. (2016) and references therein.

Using the prescription described in Fortney et al. (2006)) and Showman et al. (2009), we compute simulated eclipse depths derived from our GCM results for each planet over a period of 1-2 Earth years (Figure 4.6). At each *Spitzer* bandpass, the simulations, on average, exhibit a

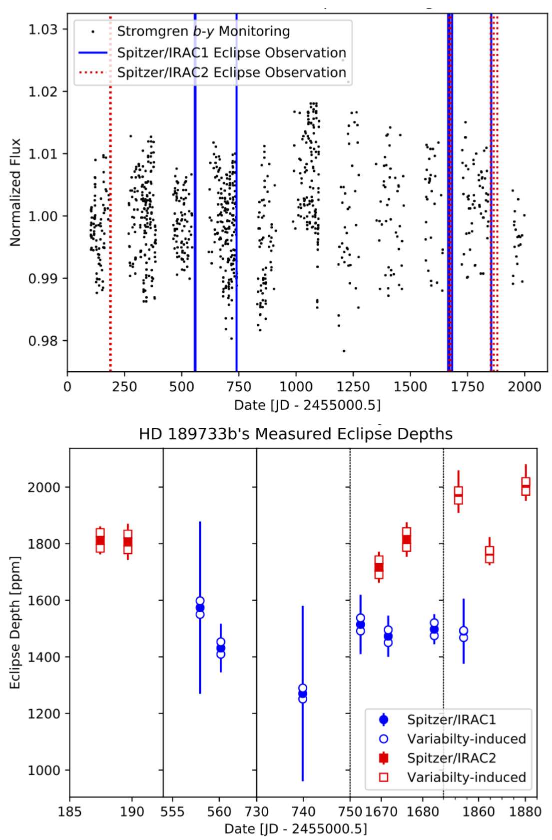

Figure 4.5 Top : HD 189733's stellar variability from the 2009–2014 observing seasons with our *Spitzer* /IRAC observations also indicated (IRAC1 in solid blue and IRAC2 in dotted red). $Bottom$: Conservatively using HD 189733's overall peak-to-trough variability (Top), we estimate its impact on the planet's eclipse depth using the prescriptions described in Knutson et al. (2012) and Zellem et al. (2017). We find that any variability-induced changes to HD 189733b's eclipse depths (empty blue diamonds for IRAC2 and empty red squares for IRAC2) fall within our measurement uncertainties. Therefore, HD 189733's stellar variability does not statistically impact our measured eclipse depths.

periodic variation in eclipse depth of 1-1.5 % over a period of ∼43 days for HD 189733b and a variation of 0.5-1 % over a period of ∼40 days for HD 209458b. This predicted variability is the result of a global sloshing mode or wave dynamics deep in the planetary atmosphere that leave only a small measurable effect at observable pressures Showman et al. (2009). Therefore, hot Jupiters such as these should exhibit low (∼1%) variability over timescales much longer than the planet's orbital period and smaller than the typical uncertainty in eclipse depth with current instruments.

The low observed atmospheric variability of HD 189733b and HD 209458b with *Spitzer* is in contrast to observations of brown dwarfs and solar system gas giants where temporal variability at infrared wavelengths has been observed at the 10-50% level (see review by Artigau 2018). The low level of observable infrared variability for hot Jupiters like HD 189733b and HD 209458b compared with brown dwarfs and solar system gas giants likely arises from differences in the relative strengths in radiative and advective processes taking place in their atmospheres. Because brown dwarfs are self-luminous and comparatively fast rotators (T_{orb} ~hrs), their circulation is dominated by multiple bands of jets and vortices (Showman et al. 2019). In contrast, the high stellar insolation and synchronous (and hence slower) rotation of hot Jupiters results in the emergence of strong day-night forcing that produce fast (~1 km/s) planetary-scale jets. The strong radiative forcing and global-scale circulation patterns in the observable portion of hot Jupiter atmospheres suppress small scale variations in the planet's thermochemical structure that would contribute to large-amplitude variations in the dayside flux from the planet.

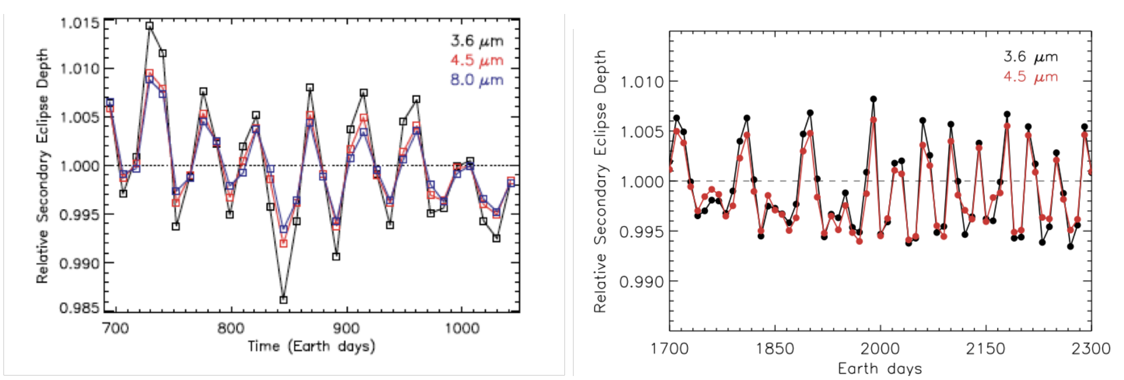

Figure 4.6 Model predictions of variability in eclipse depth orbit to orbit. The top panel is taken from Showman et al. (2009) and shows the predicted change in eclipse depth orbit to orbit for HD 189733b at 3.6, 4.5, and 8.0 μm. The bottom panel shows the predicted variation for HD 209458b at 3.6 and 4.5 μm. In both cases the eclipse depths are scaled by the mean eclipse depth to illustrate only the relative change.

4.6.2 Further Observational Probes of Variability

Our ability to probe variability in exoplanet atmospheres is currently limited by the available targets and observational facilities. It is important to remember that facilities like *Spitzer* were not originally designed for high-precision time-series observations. With hot Jupiter targets that orbit bright nearby host stars like HD 209458b and HD 189733b; per eclipse precisions on the order of 100 ppm can be achieved with *Spitzer*. Future observational facilities, such as *JWST* , will both improve the achievable precision on eclipse depth measurements and greatly expand the wavelengths over which they can be obtained (Beichman et al. 2014). Hot Jupiter models predict significant variations in temperature, chemistry, and circulation patterns as a function of pressure level in the atmosphere (e.g. Showman et al. 2009), which translates into a strong wavelength dependence in the predicted levels of observable variability (e.g. Lewis et al. 2014). The observations presented here at 3.6 and 4.5 μm for HD 209458b and HD 189733b are predicted to probe a fairly limited pressure range in the $\sim$1-100 mbar level of these planets atmospheres (e.g. Showman et al. 2009). Future observations of hot Jupiters at higher precision spanning a larger range of wavelengths as well as observations of cooler exoplanets will be critical for expanding our understanding of the physical processes driving variability, or the lack thereof, in exoplanet atmospheres.

4.6.3 Non-Uniform Disc

There is prior evidence of non-uniform thermal distributions in both of the targets studied here. The analysis of the full orbit phase curves of HD 189733b (Knutson et al. 2012) provide evidence for an eastward shift of the hottest portion of the planetary atmosphere with respect to the substellar point of 5.29 $\pm$ 0.59 and 2.98 $\pm$ 0.82 hours in channels 1 and 2 respectively. These offsets correspond to longitudinal offsets of 35° $\pm$ 4° and 20° $\pm$ 6°. Similarly, phase curve analysis of HD 209458b at 4.5 μm by Zellem et al. (2014) indicates an offset of 41° $\pm$ 6°.

Williams et al. (2006) and Rauscher et al. (2007) predicted that a non-uniform dayside temperature distribution will change the shape of ingress/egress in comparison to a uniformly

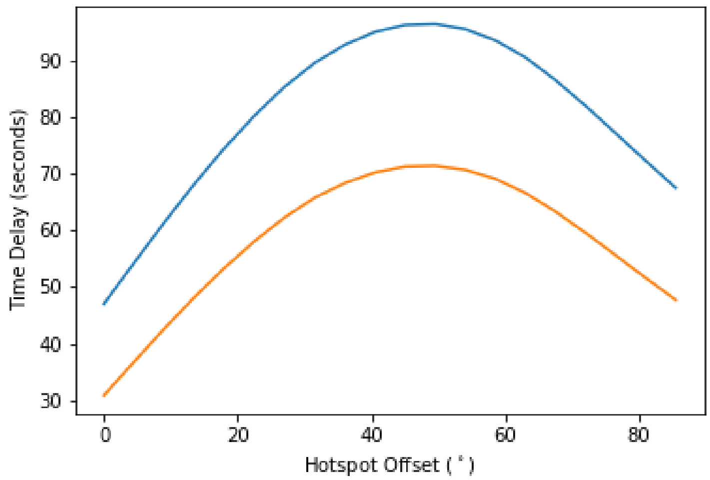

Figure 4.7 Apparent delay in center of eclipse time as a function of the offset of the hot spot (in degrees) for HD 209458b (blue) and HD 189733b (orange) at 4.5 μm. An offset hot spot causes changes to the shape of ingress/egress that will manifest as a delay in the eclipse timing when being fit with a uniform occultation model.

bright model. Also, as Williams et al. (2006) predicted and Agol et al. (2010a) observed, fitting the eclipse of a planet with a non-uniform dayside temperature distribution with a uniform occultation model will result in an apparent delay in the eclipse time as a result of these changes to the shape of ingress/egress when the timing of the eclipse is a free parameter. In Figures 4.2 and 4.3 we plot the difference between the center of eclipse time and what would be expected by assuming that the eclipse would occur at exactly one half of a period from the transit. HD 209458b consistently shows an offset in the eclipse time of 155 $\pm$ 25 seconds in Channel 1 and 129 $\pm$ 16 seconds in Channel 2. HD 189733b shows an offset of 28 $\pm$ 27 seconds in Channel 1 and 35 $\pm$ 13 seconds in Channel 2.

Figure 4.7 shows the magnitude of the effect of longitudinal offset on the observed center of eclipse time. We create a model planet with a hotspot of radius (0.5 R_{planet}) utilizing the python package SPIDERMAN (Louden & Kreidberg 2017). The global (out of hot spot) temperature is set to 1200 K and the hot spot temperature to 1700 K. Starting with the hot spot centered at the substellar point, we move the hotspot longitudinally in 1° increments and fit at each iteration with a uniform brightness model with center of eclipse time as a free parameter. We plot in Figure 4.7 the delay in eclipse time relative to the predicted time exactly one half period from transit. Note that some portion of apparent delay is present even in the 0° offset case. This is due to light travel time across the solar system ($\sim$ 45 sec. for HD 209). The offset of the maximum brightness observed in the phase curves would suggest that eclipse observations fit with a uniform model should exhibit an offset in eclipse timing of 40 and 60 seconds (Ch. 1 and 2) for HD 189733b and 90 seconds for HD 209458b channel 2 observations. The secondary eclipse fits presented here show strong agreement with the phase curve observations of HD 209458b. We are unable to confirm the phase curve offsets for HD 189733b with the precision attained with this set of observations.

As a further probe of non-uniformity, we refit the data while fixing the eclipse time to the expected value based on previous observations of epoch of transit and assuming a circular orbit. We combine the residuals of all the fits of each target in each channel to probe for any coherent deviations from the uniform model. Fig. 4.8 shows the stacked residuals from all of the channel 2 fits of HD 209. Here we see strong evidence for deviations in the shape of ingress/egress that could be caused by an eastward shifted hotspot. There are other factors that could also mimic this effect. The effect of eccentricity and shape of planet are explored in detail by de Wit et al. (2012). However, the precision with which the orbital properties of both of these canonical hot-Jupiters have been characterized allow many of factors to be ruled out or tight enough constraints to be placed on them to make a significant detection of non-uniformity likely in future eclipse mapping studies (Rauscher et al. 2018).

4.7 Conclusion

This analysis of multi - epoch secondary eclipse observations of the canonical hot Jupiters, HD 189733b and HD 209458b, finds no evidence for temporal variability greater than the precision of our observations. We expect variability in secondary eclipse depth to be driven by the dynamics of the atmosphere thus motivating comparison of observations to GCM predictions. The simulations, on average, exhibit a periodic variation in eclipse depth of 1-1.5 % for both planets at both 3.6 and

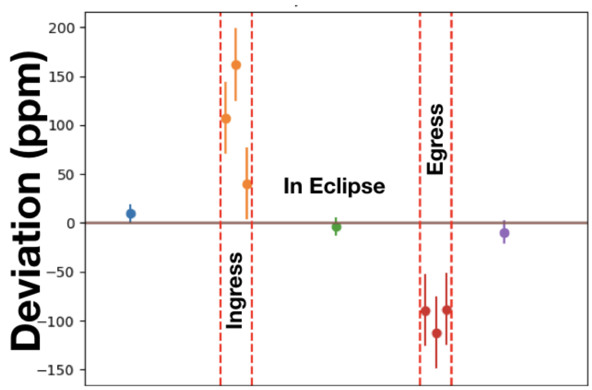

Figure 4.8 Here we stack the residuals from the best fit of each HD 209458b channel 2 observation with the time of mid eclipse fixed to coincide with phase 0.5 plus the transit time of light across the system. We bin them into 9 separate bins: one each for pre-eclipse, during eclipse, and post-eclipse and three each for ingress and egress. The structure shown in ingress/egress is similar to model predictions of deviations resulting from fitting a non-uniform dayside temperature distribution with a uniform occultation model.

4.5 μm. Based on the uncertainty in each measurement of secondary eclipse depth, we are able to constrain variability to less than (5.6% and 6.0%) and (12% and 1.6%) for channels (1,2) of HD 189733b and HD 209458b respectively. The lack of evidence of variability provides motivation and justification to combine multi - epoch observations to achieve the precision necessary to perform high spatial resolution techniques such as eclipse mapping. The apparent offset of the center of eclipse time evident in these observations provides further evidence for a non-uniform dayside temperature distribution for the planet HD 209458b. We compare the evidence for non - uniformity to previous analyses of full phase curve observations and find agreement with HD 209458b observations at 4.5 μm. The precision achieved by these observations when phase folding and stacking all like observations is enough to resolve deviations to ingress/egress caused by a non - uniform temperature distribution in at least the case of HD 209458b at 4.5 μm. This level of precision meets the requirements to utilize the eclipse mapping technique to produce spatially resolved, two dimensional maps of the planetary dayside thermal distribution.

4.8 Acknowledgements

This work was supported by NASA Headquarters under the NASA Earth and Space Science Fellowship Program under Grant Number 80NSSC17K0484. This work is based on observations made with the *Spitzer Space Telescope*, which is operated by the Jet Propulsion Laboratory, California Institute of Technology under a contract with NASA. We also acknowledge that part of this work was completed at the Space Telescope Science Institute (STScI) operated by AURA, Inc. This research has made use of the Exoplanet Orbit Database and the Exoplanet Data Explorer at exoplanets.org.

References

Adcroft, A., Hill, C., Campin, J.-M., Marshall, J., & Heimbach, P. 2004, in Seminar on Recent developments in numerical methods for atmospheric and ocean modelling, 6-10 September 2004, ECMWF (Shinfield Park, Reading: ECMWF), 139–150

Agol, E., Cowan, N. B., Knutson, H. A., Deming, D., Steffen, J. H., Henry, G. W., & Charbonneau, D. 2010a, ApJ, 721, 1861

—. 2010b, ApJ, 721, 1861

Aigrain, S., Pont, F., & Zucker, S. 2012, MNRAS, 419, 3147

Artigau, É. 2018, Variability of Brown Dwarfs, 94

Barstow, J. K., Aigrain, S., Irwin, P. G. J., Kendrew, S., & Fletcher, L. N. 2015, MNRAS, 448, 2546

Beichman, C., Benneke, B., Knutson, H., Smith, R., Lagage, P.-O., Dressing, C., Latham, D., Lunine, J., Birkmann, S., Ferruit, P., Giardino, G., Kempton, E., Carey, S., Krick, J., Deroo, P. D., Mandell, A., Ressler, M. E., Shporer, A., Swain, M., Vasisht, G., Ricker, G., Bouwman, J., Crossfield, I., Greene, T., Howell, S., Christiansen, J., Ciardi, D., Clampin, M., Greenhouse, M., Sozzetti, A., Goudfrooij, P., Hines, D., Keyes, T., Lee, J., McCullough, P., Robberto, M., Stansberry, J., Valenti, J., Rieke, M., Rieke, G., Fortney, J., Bean, J., Kreidberg, L., Ehrenreich, D., Deming, D., Albert, L., Doyon, R., & Sing, D. 2014, PASP, 126, 1134

Berta, Z. K., Charbonneau, D., Bean, J., Irwin, J., Burke, C. J., Désert, J.-M., Nutzman, P., & Falco, E. E. 2011, ApJ, 736, 12

Carter, J. A., Winn, J. N., Holman, M. J., Fabrycky, D., Berta, Z. K., Burke, C. J., & Nutzman, P. 2011, ApJ, 730, 82

Cauley, P. W., Kuckein, C., Redfield, S., Shkolnik, E. L., Denker, C., Llama, J., & Verma, M. 2018, AJ, 156, 189

Cauley, P. W., Redfield, S., & Jensen, A. G. 2017, AJ, 153, 217

Charbonneau, D., Brown, T. M., Latham, D. W., & Mayor, M. 2000, ApJ, 529, L45

Charbonneau, D., Knutson, H. A., Barman, T., Allen, L. E., Mayor, M., Megeath, S. T., Queloz, D., & Udry, S. 2008a, ApJ, 686, 1341

—. 2008b, ApJ, 686, 1341

Cho, J. Y.-K., Menou, K., Hansen, B. M. S., & Seager, S. 2003, ApJ, 587, L117

Czesla, S., Huber, K. F., Wolter, U., Schröter, S., & Schmitt, J. H. M. M. 2009, A&A, 505, 1277

Damasso, M., Biazzo, K., Bonomo, A. S., Desidera, S., Lanza, A. F., Nascimbeni, V., Esposito, M., Scandariato, G., Sozzetti, A., Cosentino, R., Gratton, R., Malavolta, L., Rainer, M., Gandolfi, D., Poretti, E., Zanmar Sanchez, R., Ribas, I., Santos, N., Affer, L., Andreuzzi, G., Barbieri, M., Bedin, L. R., Benatti, S., Bernagozzi, A., Bertolini, E., Bonavita, M., Borsa, F., Borsato, L., Boschin, W., Calcidese, P., Carbognani, A., Cenadelli, D., Christille, J. M., Claudi, R. U., Covino, E., Cunial, A., Giacobbe, P., Granata, V., Harutyunyan, A., Lattanzi, M. G., Leto, G., Libralato, M., Lodato, G., Lorenzi, V., Mancini, L., Martinez Fiorenzano, A. F., Marzari, F., Masiero, S., Micela, G., Molinari, E., Molinaro, M., Munari, U., Murabito, S., Pagano, I., Pedani, M., Piotto, G., Rosenberg, A., Silvotti, R., & Southworth, J. 2015, A&A, 575, A111

de Wit, J., Gillon, M., Demory, B.-O., & Seager, S. 2012, A&A, 548, A128

Deming, D., Knutson, H., Kammer, J., Fulton, B. J., Ingalls, J., Carey, S., Burrows, A., Fortney, J. J., Todorov, K., Agol, E., Cowan, N., Desert, J.-M., Fraine, J., Langton, J., Morley, C., & Showman, A. P. 2015, ApJ, 805, 132

Deming, D., Wilkins, A., McCullough, P., Burrows, A., Fortney, J. J., Agol, E., Dobbs-Dixon, I., Madhusudhan, N., Crouzet, N., Desert, J.-M., Gilliland, R. L., Haynes, K., Knutson, H. A., Line, M., Magic, Z., Mandell, A. M., Ranjan, S., Charbonneau, D., Clampin, M., Seager, S., & Showman, A. P. 2013, ApJ, 774, 95

Désert, J.-M., Charbonneau, D., Demory, B.-O., Ballard, S., Carter, J. A., Fortney, J. J., Cochran, W. D., Endl, M., Quinn, S. N., Isaacson, H. T., Fressin, F., Buchhave, L. A., Latham, D. W., Knutson, H. A., Bryson, S. T., Torres, G., Rowe, J. F., Batalha, N. M., Borucki, W. J., Brown, T. M., Caldwell, D. A., Christiansen, J. L., Deming, D., Fabrycky, D. C., Ford, E. B., Gilliland, R. L., Gillon, M., Haas, M. R., Jenkins, J. M., Kinemuchi, K., Koch, D., Lissauer, J. J., Lucas, P., Mullally, F., MacQueen, P. J., Marcy, G. W., Sasselov, D. D., Seager, S., Still, M., Tenenbaum, P., Uddin, K., & Winn, J. N. 2011a, ApJS, 197, 14

Désert, J.-M., Lecavelier des Etangs, A., Hébrard, G., Sing, D. K., Ehrenreich, D., Ferlet, R., & Vidal-Madjar, A. 2009, ApJ, 699, 478

Désert, J.-M., Sing, D., Vidal-Madjar, A., Hébrard, G., Ehrenreich, D., Lecavelier Des Etangs, A., Parmentier, V., Ferlet, R., & Henry, G. W. 2011b, A&A, 526, A12

Diamond-Lowe, H., Stevenson, K. B., Bean, J. L., Line, M. R., & Fortney, J. J. 2014, ApJ, 796, 66

Eaton, J. A., Henry, G. W., & Fekel, F. C. 2003, in Astrophysics and Space Science Library, Vol. 288, Astrophysics and Space Science Library, ed. T. D. Oswalt, 189

Ehrenreich, D., Hébrard, G., Lecavelier des Etangs, A., Sing, D. K., Désert, J.-M., Bouchy, F., Ferlet, R., & Vidal-Madjar, A. 2007, ApJ, 668, L179

Foreman-Mackey, D., Hogg, D. W., Lang, D., & Goodman, J. 2013, PASP, 125, 306

Fortney, J. J., Cooper, C. S., Showman, A. P., Marley, M. S., & Freedman, R. S. 2006, ApJ, 652, 746

Fraine, J., Deming, D., Benneke, B., Knutson, H., Jordán, A., Espinoza, N., Madhusudhan, N., Wilkins, A., & Todorov, K. 2014, Nature, 513, 526

Gelman, A. & Rubin, D. B. 1992, Statistical science, 457

Gibson, N. P., Aigrain, S., Pont, F., Sing, D. K., Désert, J.-M., Evans, T. M., Henry, G., Husnoo, N., & Knutson, H. 2012, MNRAS, 422, 753

Gillon, M., Lanotte, A., Barman, T., Miller, N., Demory, B.-O., Deleuil, M., Montalbán, J., Bouchy, F., Cameron, A. C., Deeg, H., et al. 2010, Astronomy & Astrophysics, 511, A3

Henry, G. W. 1999, PASP, 111, 845

Ingalls, J. G., Krick, J. E., Carey, S. J., Laine, S., Surace, J. A., Glaccum, W. J., Grillmair, C. C., & Lowrance, P. J. 2012, in SPIE Astronomical Telescopes+ Instrumentation, International Society for Optics and Photonics, 84421Y–84421Y

Ingalls, J. G., Krick, J. E., Carey, S. J., Laine, S., Surace, J. A., Glaccum, W. J., Grillmair, C. C., & Lowrance, P. J. 2012, in Proc. SPIE, Vol. 8442, Space Telescopes and Instrumentation 2012: Optical, Infrared, and Millimeter Wave, 84421Y

Ingalls, J. G., Krick, J. E., Carey, S. J., Stauffer, J. R., Lowrance, P. J., Grillmair, C. J., Buzasi, D., Deming, D., Diamond-Lowe, H., Evans, T. M., Morello, G., Stevenson, K. B., Wong, I., Capak, P., Glaccum, W., Laine, S., Surace, J., & Storrie-Lombardi, L. 2016, AJ, 152, 44

Kataria, T., Sing, D. K., Lewis, N. K., Visscher, C., Showman, A. P., Fortney, J. J., & Marley, M. S. 2016, ApJ, 821, 9

Kilpatrick, B. M., Kataria, T., Lewis, N. K., Zellem, R. T., Henry, G. W., Cowan, N. B., De Wit, J., Fortney, J. J., Knutson, H., Seager, S., Showman, A. P., & Tucker, G. S. 2019, arXiv e-prints

Kilpatrick, B. M., Lewis, N. K., Kataria, T., Deming, D., Ingalls, J. G., Krick, J. E., & Tucker, G. S. 2017, AJ, 153, 22

Knutson, H. A., Charbonneau, D., Allen, L. E., Fortney, J. J., Agol, E., Cowan, N. B., Showman, A. P., Cooper, C. S., & Megeath, S. T. 2007, Nature, 447, 183

Knutson, H. A., Charbonneau, D., Cowan, N. B., Fortney, J. J., Showman, A. P., Agol, E., Henry, G. W., Everett, M. E., & Allen, L. E. 2009, ApJ, 690, 822

Knutson, H. A., Lewis, N., Fortney, J. J., Burrows, A., Showman, A. P., Cowan, N. B., Agol, E., Aigrain, S., Charbonneau, D., Deming, D., Désert, J.-M., Henry, G. W., Langton, J., & Laughlin, G. 2012, ApJ, 754, 22

Kreidberg, L. 2015, PASP, 127, 1161

Lewis, N. K., Knutson, H. A., Showman, A. P., Cowan, N. B., Laughlin, G., Burrows, A., Deming, D., Crepp, J. R., Mighell, K. J., Agol, E., Bakos, G. Á., Charbonneau, D., Désert, J.-M., Fischer, D. A., Fortney, J. J., Hartman, J. D., Hinkley, S., Howard, A. W., Johnson, J. A., Kao, M., Langton, J., & Marcy, G. W. 2013, ApJ, 766, 95

Lewis, N. K., Showman, A. P., Fortney, J. J., Knutson, H. A., & Marley, M. S. 2014, ApJ, 795, 150

Line, M. R., Stevenson, K. B., Bean, J., Desert, J.-M., Fortney, J. J., Kreidberg, L., Madhusudhan, N., Showman, A. P., & Diamond-Lowe, H. 2016, AJ, 152, 203

Louden, T. & Kreidberg, L. 2017, SPIDERMAN: Fast code to simulate secondary transits and phase curves, Astrophysics Source Code Library

Majeau, C., Agol, E., & Cowan, N. B. 2012, ApJ, 747, L20

Mandel, K. & Agol, E. 2002, ApJ, 580, L171

Marley, M. S. & McKay, C. P. 1999, , 138, 268

McCullough, P. R., Crouzet, N., Deming, D., & Madhusudhan, N. 2014, ApJ, 791, 55

Menou, K., Cho, J. Y.-K., Seager, S., & Hansen, B. M. S. 2003, ApJ, 587, L113

Morris, B. M., Agol, E., Davenport, J. R. A., & Hawley, S. L. 2018, ApJ, 857, 39

Oshagh, M., Santos, N. C., Ehrenreich, D., Haghighipour, N., Figueira, P., Santerne, A., & Montalto, M. 2014, A&A, 568, A99

Pont, F., Knutson, H., Gilliland, R. L., Moutou, C., & Charbonneau, D. 2008, MNRAS, 385, 109

Rackham, B., Espinoza, N., Apai, D., López-Morales, M., Jordán, A., Osip, D. J., Lewis, N. K., Rodler, F., Fraine, J. D., Morley, C. V., & Fortney, J. J. 2017, ApJ, 834, 151

Rackham, B. V., Apai, D., & Giampapa, M. S. 2018, ApJ, 853, 122

—. 2019, AJ, 157, 96

Rauscher, E., Menou, K., Seager, S., Deming, D., Cho, J. Y.-K., & Hansen, B. M. S. 2007, ApJ, 664, 1199

Rauscher, E., Suri, V., & Cowan, N. B. 2018, AJ, 156, 235

Showman, A. P., Fortney, J. J., Lian, Y., Marley, M. S., Freedman, R. S., Knutson, H. A., & Charbonneau, D. 2009, ApJ, 699, 564

Showman, A. P. & Guillot, T. 2002, A&A, 385, 166

Silva-Valio, A. 2008, ApJ, 683, L179

Sing, D. K., Pont, F., Aigrain, S., Charbonneau, D., Désert, J.-M., Gibson, N., Gilliland, R., Hayek, W., Henry, G., Knutson, H., Lecavelier Des Etangs, A., Mazeh, T., & Shporer, A. 2011, MNRAS, 416, 1443

Williams, P. K. G., Charbonneau, D., Cooper, C. S., Showman, A. P., & Fortney, J. J. 2006, ApJ, 649, 1020

Wolter, U., Schmitt, J. H. M. M., Huber, K. F., Czesla, S., Müller, H. M., Guenther, E. W., & Hatzes, A. P. 2009, A&A, 504, 561

Zellem, R. T., Griffith, C. A., Pearson, K. A., Turner, J. D., Henry, G. W., Williamson, M. H., Ryleigh Fitzpatrick, M., Teske, J. K., & Biddle, L. I. 2015, ApJ, 810, 11

Zellem, R. T., Lewis, N. K., Knutson, H. A., Griffith, C. A., Showman, A. P., Fortney, J. J., Cowan, N. B., Agol, E., Burrows, A., Charbonneau, D., Deming, D., Laughlin, G., & Langton, J. 2014, ApJ, 790, 53

Zellem, R. T., Swain, M. R., Roudier, G., Shkolnik, E. L., Creech-Eakman, M. J., Ciardi, D. R., Line, M. R., Iyer, A. R., Bryden, G., Llama, J., & Fahy, K. A. 2017, ApJ, 844, 27

Chapter 5

Eclipse Mapping

Eclipse Mapping is, quite possibly, the most difficult and precise measurement ever made in characterizing exoplanet atmospheres. It requires resolving small changes to the shape of ingress and egress on minute timescales. The amplitude of the deviations vary depending on the asymmetry of the planetary brightness distribution, brightness temperature, and wavelength. For the targets in this study, the amplitudes were of a few hundred ppm. Achieving that level of precision per minute required about a dozen eclipse observations of each target in each channel. Co-fitting that number of observations, each with their own unique set of systematics, is challenging in methodology and in computation. The amount of data exceeded millions of data points and the computational time to iterate over brightness models grew intolerably long. Despite these challenges, I present a preliminary analysis of the combined eclipse observations for both targets in both channels. I present retrieved eclipse maps and discuss the comparison of those maps to model predictions. This work is preliminary and not yet published. I anticipate expanding a great deal on this initial effort in the future to include more models of brightness, combining eclipses with phase curves, exploring latitudinal information.

5.1 Introduction

The global circulation patterns in a planet's atmosphere control the transport of heat, chemical species, and cloud particles that have a profound effect on the optical and infrared spectra of these planets. Hot Jupiters are perfect candidates for refining models of atmospheric circulation. The radiative-convective boundary of hot Jupiters should occur at large optical depths (Showman et al. (2010)), further simplifying atmospheric models. The refinement of these models will allow us great insight into physical processes in temperature and pressure regimes unlike any in our solar system. Hot Jupiters have been the basis for a long list of GCM's including: Showman & Guillot (2002); Cooper & Showman (2005); Showman et al. (2009);Mayne et al. (2014); Dobbs-Dixon & Lin (2008); Dobbs-Dixon & Agol (2013); Menou & Rauscher (2010); Lewis et al. (2010); Heng et al. (2011); Thrastarson & Cho (2010); Perna et al. (2012); Rauscher & Kempton (2014). Many of the listed models are based upon the planetary parameters of HD 189733b.

Observers have previously found evidence for longitudinal thermal offsets through phase curve observations which suggest the presence of strong circulatory winds. However, to gain further insights into the fundamentally three-dimensional physical processes shaping exoplanet atmospheres, we must probe their three-dimensional thermal structure. Eclipse mapping is an observational tool that allows for the creation of brightness maps of the dayside of a planet's atmosphere that are resolved both in longitude and latitude (two dimensional). Eclipse Mapping was demonstrated in the analysis of HD 189733b performed by both Majeau et al. (2012), de Wit et al. (2012) and Rauscher et al. (2018) using *Spitzer* 8μm observations. During ingress/egress the planet is obscured by the limb of the host star at some angle based on inclination (Figure 5.1. The combination of these two 'slicings' of the planet yield a grid from which we can extract both longitudinal and latitudinal information. Eclipse mapping at a single wavelength paints only a two-dimensional picture of a planet's thermal structure, but when combined with maps at other wavelengths that probe different depths and molecular features, such as *Spitzer* IRAC 3.6 and 4.5 μm, the three-dimensional thermal structure of the planet can be revealed. These three-dimensional maps can then be used to compare with, and inform ,the wealth of three-dimensional general circulation models for hot-Jupiters. Here we extend the work done with HD 189733 at 8 μm to create three-dimensional brightness maps of the two 'benchmark' hot-Jupiters, HD 189733b and HD 209458b, at both 3.6 and 4.5 μm. Although we have achieved rough maps of the thermal

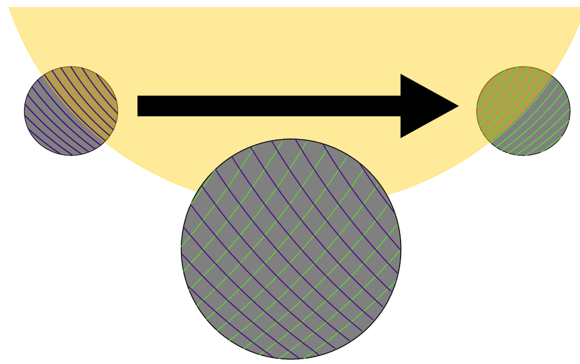

Figure 5.1 Eclipse mapping creates two orthogonal scans of the planet's dayside during eclipse ingress/egress as the planet is partially occulted by the limb of the star. Green/purple lines show to-scale representation of the spatial resolution achieved for two-minute temporal resolution of ingress/egress for HD 189733b.

distributions for both of these planets at 3.6 and 4.5 μm through phase curve observations, our goal is to go one step further and take a 'high-resolution snapshot' of their dayside atmospheres.

The first attempts to construct thermal maps of exoplanet atmospheres were achieved through phase curve observations of tidally-locked hot-Jupiters. The first phase curve observations covered a half orbit of the hot-Jupiter HD 189733b using the 8 μm bandpass of *Spitzer*. This infrared phase-curve for HD 189733b from Knutson et al. (2007) revealed that the hottest region of the planet is 30° east of the substellar point. This shift in the thermal profile of the planet is a clear indication of the presence of winds in the atmosphere of HD 189733b. Phase curves for several other close-in giant planets have also been obtained and all show varying degrees of thermal homogenization by winds. Although phase curve measurements have given us a great deal of insight into day/night temperature gradients and the transport of heat away from the substellar longitude by winds, they still paint an incomplete picture when compared with the global flow patterns observed in general circulation models (GCMs) for hot-Jupiters. When the 8 μm phase curve was combined with the multiple planetary eclipses at 8 μm first presented in Agol et al. (2010) a significantly clearer picture of the thermal structure of HD 189733b near the 8 μm photosphere emerged. By mapping the deviations in the eclipse shape from that for a uniformly bright disk, both de Wit et al. (2012) and Majeau et al. (2012) were able to not only better constrain the longitude range associated with the peak in the planetary flux (uncertainty reduced from 30° to 4° assuming a circular orbit), but also to detect a hint of a possible shift in thermal 'hotspot' away from being centered on the planet's equator. The combined information from the 8 μm phase curve and eclipses of HD 189733b still do not give a complete understanding of the underlying physical processes in the planet's atmosphere. Further phase curve observations by Knutson et al. (2012) at 3.6 and 4.5 μm revealed that although the standard hot-Jupiter GCMs could readily explain the 8 μm phase curve, additional atmospheric processes were shaping the 3.6 and 4.5 μm phase curves.

5.2 Observations

Here we consider all existing secondary eclipse observations of HD 189733b and HD 209458b in channels 1 and 2 (3.6 or 4.5 μm bandpass). The observations analyzed here are part of Programs 60021 (PI: H. Knutson) and 10103 (PI: N. Lewis), 90186 (PI: K. Todorov), and 70100 (PI: M. Swain). This same set of observations were analyzed in Kilpatrick et al. (2019) and the details of each Astronomical Observing Request (AOR) are presented there. All of the observations were carried out in sub-array mode (32×32 pixels, $39" \times 39"$). Observations in Program 10103 utilize a 30 minute peak-up observation preceding them to stabilize the image on the detector 'sweet spot' and decreases the likelihood of a ramp in the data (Ingalls et al. 2012). Program 60021 observations are full orbit phase curves from which we extract the AORs containing the eclipse from the larger data set. We include the entirety of the full orbit phase curve when co-fitting the eclipses and phase curves simultaneously.

This set of observations are unique in that they are a multi-epoch set spanning several years (Table 4.3 and 4.4.1. In Kilpatrick et al. (2019) we found no indications of temporal variability greater than the precision of our data. Given this result, combining theses multi-epoch observations will allow us to gain the precision needed to meet our goals.

5.3 Methods

5.3.1 Photometric Extraction

For each AOR we began with Basic Calibrated Data (BCD) available on the Spitzer Heritage Archive. Each BCD file contains a cube of 64 frames of 64×64 pixels. Each set of 64 images comes as a single FITS file with a time stamp corresponding to the start of the first image. We determine the time of each frame in the set by adding the appropriate multiple of the frame time to the time stamp of the first image. Each frame was corrected for bad pixels or NaN values by masking the invalid pixels. Each frame is background subtracted based on the median pixel value outside of a 10 x 10 pixel box around the stellar centroid. Pixel values in the background region that deviate from the mean by more than 5 σ are clipped and the median value remaining is taken to be the background. Stellar centroid positions for each frame are determined by a first moment center of mass calculation.

The noise pixel parameter ($\tilde{\beta}$) (Lewis et al. 2013; Kilpatrick et al. 2017) is calculated for each frame as

$$\tilde{\beta} = \frac{(\sum P_i)^2}{\sum (P_i^2)}, \tag{5.1}$$

where each P_i is the response measured in each pixel across the frame. We also save the 5 x 5 array of background subtracted pixel values about the stellar centroid for each frame. Each array is normalized such that they sum to one. We then perform aperture photometry about the stellar centroid using the aperture_photometry function from the Astropy package Photutils. Circular apertures of fixed radii ranging from 1.8 - 2.8 pixels and variable radii apertures ranging from $\beta_{\text{pix}} \times$ {0.7...1.2} and $\beta_{\text{pix}} +$ {-0.6...1.4}. The resultant time series photometry is then filtered by removing any points that deviate by more than 3 σ from the median values of flux or x,y position.

5.3.2 Systematics Correction

Here, we employ the Nearest Neighbors method (NNBR), otherwise known as Gaussian Kernel Regression with data (Lewis et al. 2013; Kilpatrick et al. 2017, 2019) for correcting the intrapixel sensitivity variation (Ingalls et al. 2012). NNBR corrects each data point (i) in the light curve is corrected by linking it with its 50 nearest neighbors j by distance:

$$r_{i,j} = \sqrt{a(x_i - x_j)^2 + b(y_j - y_i)^2 + c(\tilde{\beta}_j^{\frac{1}{2}} - \tilde{\beta}_i^{\frac{1}{2}})^2}. \tag{5.2}$$

Each nearest neighbor was weighted with a Gaussian smoothing kernel $K_i(j) =$

$$exp\left(-\frac{(x_j - x_i)^2}{2\sigma_{x,i}^2} - \frac{(y_j - y_i)^2}{2\sigma_{y,i}^2} - \frac{(\tilde{\beta}_j^{\frac{1}{2}} - \tilde{\beta}_i^{\frac{1}{2}})^2}{2\sigma_{\tilde{\beta}_j^{\frac{1}{2}},i}^2}\right), \tag{5.3}$$

where x and y are the stellar centroid locations on the detector and the three-dimensional widths of the smoothing kernel are controlled by the σ terms that adjust depending on the density of the nearest neighbors.

The corrected relative flux value for any photometric point F_i with centroid position (x_i, y_i) and uncorrected flux value $F_{0,i}$ then becomes

$$F_i = \frac{F_{0,i}}{W_i(x_i, y_i)}, \tag{5.4}$$

where

$$W_i(x_i, y_i) = \frac{\sum_j F_{0,j} K_i(j)}{\sum_j K_i(j)}. \tag{5.5}$$

W_i(x_i, y_i) is summed over the 50 nearest neighbors (those with the smallest $r_{i,j}$ values).

[]

Spitzer IRAC data is also known to have an exponential ramp in flux over the first 30–60 minutes of observing; however the peak-up technique has alleviated this problem to some extent (Kilpatrick et al. 2017; Ingalls et al. 2016). In previous work (Kilpatrick et al. 2019), each data

Table 5.1. Ephemerides

Parameter	HD 189733b	HD 209458b
$T_\star$	5040±50	6065±50
$M_\star$ (M_{Sun})	0.806±0.048	1.131±0.026
$R_\star$ (R_{Sun})	0.756±0.018	1.155±0.015
M_p (M_{Jup})	1.144±0.056	0.690±0.024
R_p (R_{Jup})	1.138±0.027	1.359±0.015
$R_p/R_\star$	$0.024122\pm5.8\times10^{-5}$	$0.014607\pm2.4\times10^{-5}$
log(g)	3.339±0.03	2.969±0.0187
Period	$2.21857567\pm1.5\times10^{-7}$	$3.52474859\pm 3.8\times10^{-7}$
i (°)	85.7100±0.0023	86.710± 0.05
msin i	1.140 ±0.056	0.689±0.024
$a/R_\star$	8.84±0.27	8.81±0.186

set was fit in several ways: without alteration, trimmed at 20 minutes from the beginning of the observation, and with an exponential ramp model of the form

$$R_{model} = 1 - a_1 \times e^{(-\frac{t}{a_2})}. \tag{5.6}$$

We find that in observations that have utilized the peak up technique that the 4.5μm observations require no alteration or ramp and the 3.6 μm benefit from the addition of an exponential ramp.

5.3.3 Astrophysical Model

The eclipse model was derived from the three parameter bightness model described in Zhang & Showman (2017) and implemented by Spiderman (Louden & Kreidberg 2017). The Zhang and Showman (Z+S) model creates a global brightness mmodel based upon three parameters, the ratio of radiative to advective timescales (ξ), the night side temperature (T_{night}), and the day/night temperature difference (ΔT). Spiderman then produces a lightcurve based on the brightness model.

We fit by iterating over different values for the model parameters and comparing the resulting lightcurve to the data. The orbital, stellar, and planetary parameters listed in table 5.1 were used as input fixed parameters to the model.

5.3.4 Combination of Models and Observations

We consider the observations of each planet, in each channel, as a combined set. At each iteration in the fitting process, we produce one astrophysical model for the set. That model is then used to apply the systematics correction to the lightcurve from each relevant AOR. Each, raw, uncorrected lightcurve is first divided by the astrophysical model and ramp model to leave only the intrapixel variations. For each lightcurve, with it's own set of nearest neighbors and gaussian weights, the systematics model is calculated using the procedure shown in Equations 5.4 and 5.5. The systematics model, ramp model and Astrophysical Model for each AOR are combined multiplicatively and compared to the observational data. Residuals and/or log likelihood are summed over each AOR and returned to determine best fit parameters.

We determine initial best fit values for all free parameters using a non linear least squares fitting algorithm. The results from the best fit were passed to a Markov Chain Monte Carlo implemented by emcee (Foreman-Mackey et al. 2013) to derive uncertainties of each free parameter. We use a number of walkers at least twice the number of free parameters and run for 10^5 steps per walker before testing for convergence using Gelman Rubin statistics with a threshold for acceptance of 1.1 (Gelman & Rubin 1992).

5.4 Results

The results presented here are preliminary and include only the analysis of the secondary eclipse observations (i.e. they do not include the phase curve observations). There are many variations of brightness model that can be used to create model lightcurves for fitting. In this preliminary

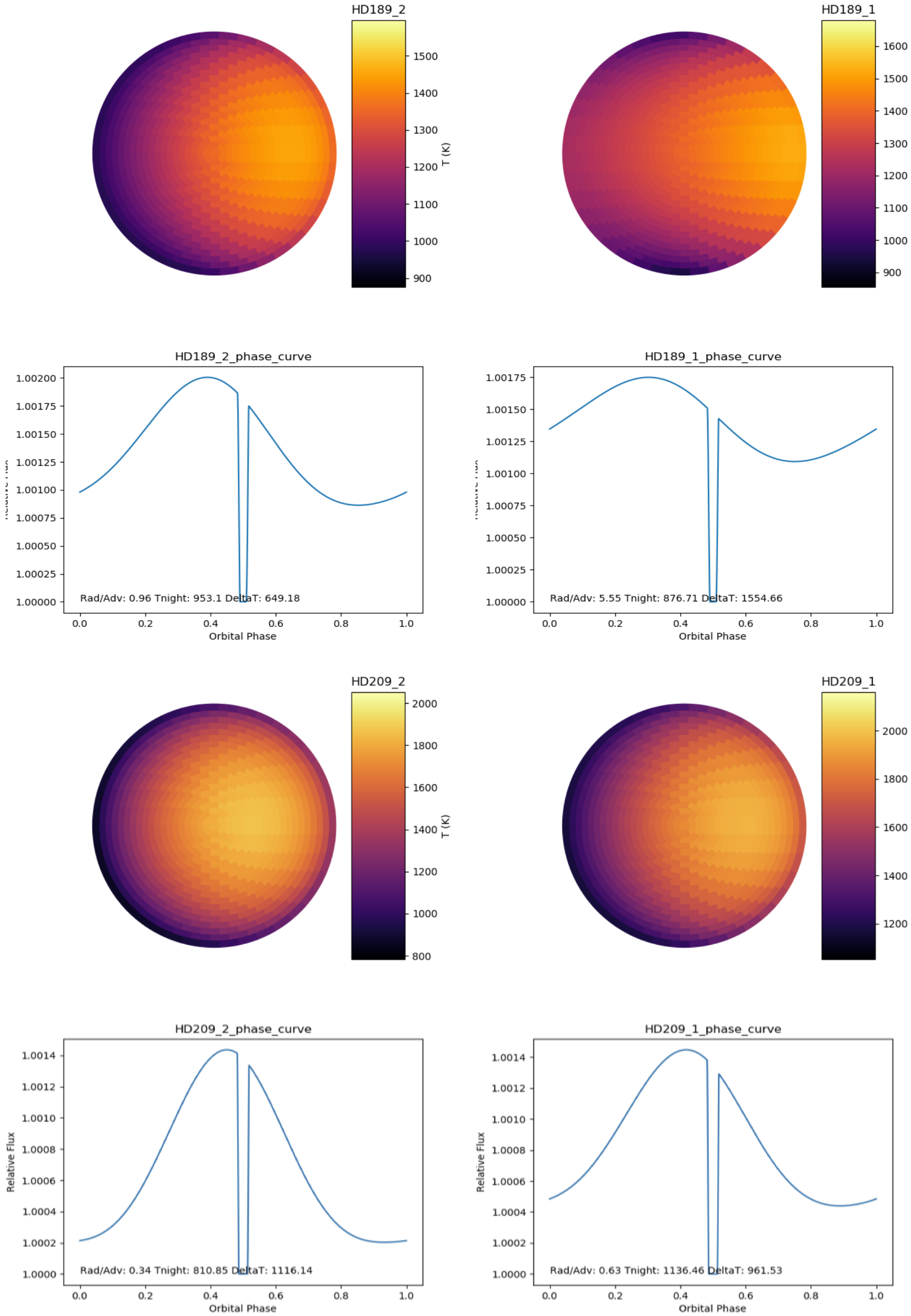

Figure 5.2 Retrieved temperature maps and phase curves for HD 189733b (top) and HD 209458b (bottom). Observations at 4.5μm are in the left column and 3.6μm are in the right column.

analysis we have only considered the Zhang and Showman brightness model. As such, we present a best fit value for each of the three Z+S parameters(ξ, T_{night}, ΔT).

5.4.1 HD 209458b

For HD 209458b we find best fit values for $\xi = 0.00 \pm 0.2$, $T_{\rm night} = 500$ K ± 231 K, and ΔT$= 1293 \pm 412$ K at 3.6 μm. Retrieving a phase curve observation from these parameters produce a lightcurve with peak flux offset of ∼45° and an amplitude of ∼60%. At 4.5 μm we find best fit values for $\xi = 0.34 \pm 0.11$, $T_{\rm night} = 810$ K ± 231 K, and ΔT$= 1116 \pm 321$ K. These parameters correspond to a phase curve with a peak offset of 25° and an amplitude of ∼80%. The brightness models and corresponding best fit parameters are shown in Figure 5.2.

5.4.2 HD 189733b

For HD 189733b we find best fit values for $\xi = 0.98 \pm 0.26$, $T_{\rm night} = 953$ K ± 385 K, and ΔT$= 649 \pm 312$ K at 3.6 μm. Retrieving a phase curve observation from these parameters produce a lightcurve with peak flux offset of ∼30° and an amplitude of ∼60%. At 4.5 μm we find best fit values for $\xi = 0.34 \pm 0.11$, $T_{\rm night} = 810$ K ± 231 K, and ΔT$= 1116 \pm 321$ K. These parameters correspond to a phase curve with a peak offset of 15° and an amplitude of ∼80%. The brightness models and corresponding best fit parameters are shown in Figure 5.2.

5.5 Discussion

5.5.1 Comparison of Observations to Models

Given that our 2D maps are in direct relation to the planet's atmospheric dynamics, we compare our Ch1 and Ch2 *Spitzer* eclipse maps to predictions from three-dimensional general circulation models (GCMs). In particular, we use GCM simulations of HD 189733b from Showman et al. (2009) and HD 209458b from Kataria et al. (2016), respectively, which utilize the Substellar and Planetary Radiation and Circulation (SPARC) model (Showman et al. 2009). The SPARC model couples the general circulation model maintained at the Massachusetts Institute of Technology (the MITgcm, Adcroft et al. (2004)) with a plane-parallel, two-stream version of the multi-stream

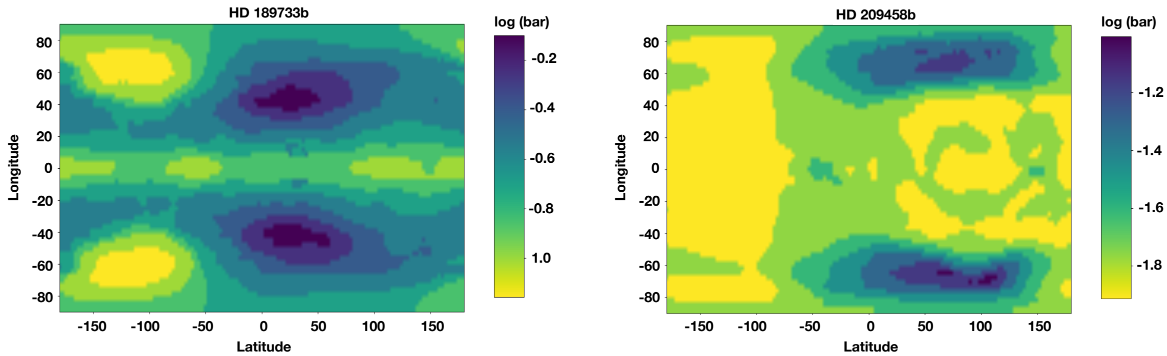

Figure 5.3 The pressure level accessed in by *Spitzer* channel 1 for HD 189733b (left) and HD 209458b (left).

radiation code developed by Marley & McKay (1999). Further details on these models are provided in (Showman et al. 2009; Kataria et al. 2016, and references within).

Eclipse mapping allows us to directly compare retrieved maps to GCM outputs at relevant pressure levels. However, given the broad band nature of *Spitzer* photometry, a single map spans a range of pressures. We compute latitude-longitude maps of the $\tau = 1$ pressure level, i.e., the pressure level accessed within each *Spitzer* bandpass (Figure 5.3). These include the effects of equilibrium condensate clouds (Ackerman & Marley 2001). It is evident that the pressures probed with *Spitzer* observations are related to day-to-night and equator-to-pole temperature structure, which is shaped by the atmospheric dynamics. For the case of HD189733b, broadly speaking, the hotter dayside accesses much deeper pressures ($\sim$150-600 mbar) than the colder nightside ($\lesssim$150 mbar). However, the pressures accessed are not uniform on either the dayside or nightside. For one, the super-rotation in HD 189733b's atmosphere plays a role in setting the pressures probed at the equator–they are fairly uniform from dayside to nightside. On the dayside, there are regions near $\sim \pm 40°$ where the pressures accessed are slightly deeper than at the equator. On the nightside, there are regions near the poles that access shallower pressures than the equator.

In comparison, observations of HD 209458b access a shallower and narrower range of pressures ($\sim$15-100 mbar) than HD 189733b. This is not a surprise, as the planet is hotter overall, and hence its photosphere is much higher in the atmosphere. The dayside hotspot is also broader from equator-to-pole due to HD 209458b's slower rotation rate, and therefore the $\tau = 1$ pressure level is more consistent with latitude.

In the following sections we utilize the Figure 5.3 to choose a representative pressure level to compare GCM outputs to our retrieved maps.

HD 209458b

Previous observations (Agol et al. 2010; Zellem et al. 2014; Kilpatrick et al. 2019) have shown evidence for, and models have predicted (Showman & Guillot 2002; Showman et al. 2009), an eastward shift of the peak of thermal emission from the sub-stellar point. The analysis of this same set of observations presented in Kilpatrick et al. (2019) showed that the 4.5 μm observations of HD 209458b were of the highest quality and had the strongest evidence for an offset hotspot. We find the eclipse mapping results presented here to be in broad agreement with both theoretical predictions and previous observations. The peak offset and amplitude of the retrieved phase curve (Figure 5.2 agree to within uncertainty with the best fit values presented from the phase curve alone in Zellem et al. (2014).

The channel 1, 3.6 μm, observations exhibited a larger than expected scatter in eclipse depths and much larger β_{red} values in comparison to channel 2. We suspect channel 1 observations still exhibit correlated noise due to unresolved systematics thus limiting their precision. Further, we can only compare our result to theoretical predictions, in this case, since we do not have a previously published phase curve analysis. At temperatures above $\sim$1500 K we would expect CO/CO_2 to be the dominant carbon bearing molecules in comparison to CH_4. In this scenario we would expect observations at 3.6μm to probe deeper regions of the atmosphere than at 4.5μm where ξ should be increasing resulting in a greater hotspot offset and more uniform longitudinal temperature distribution. Our retrieved maps and phase curves confirm these predictions.

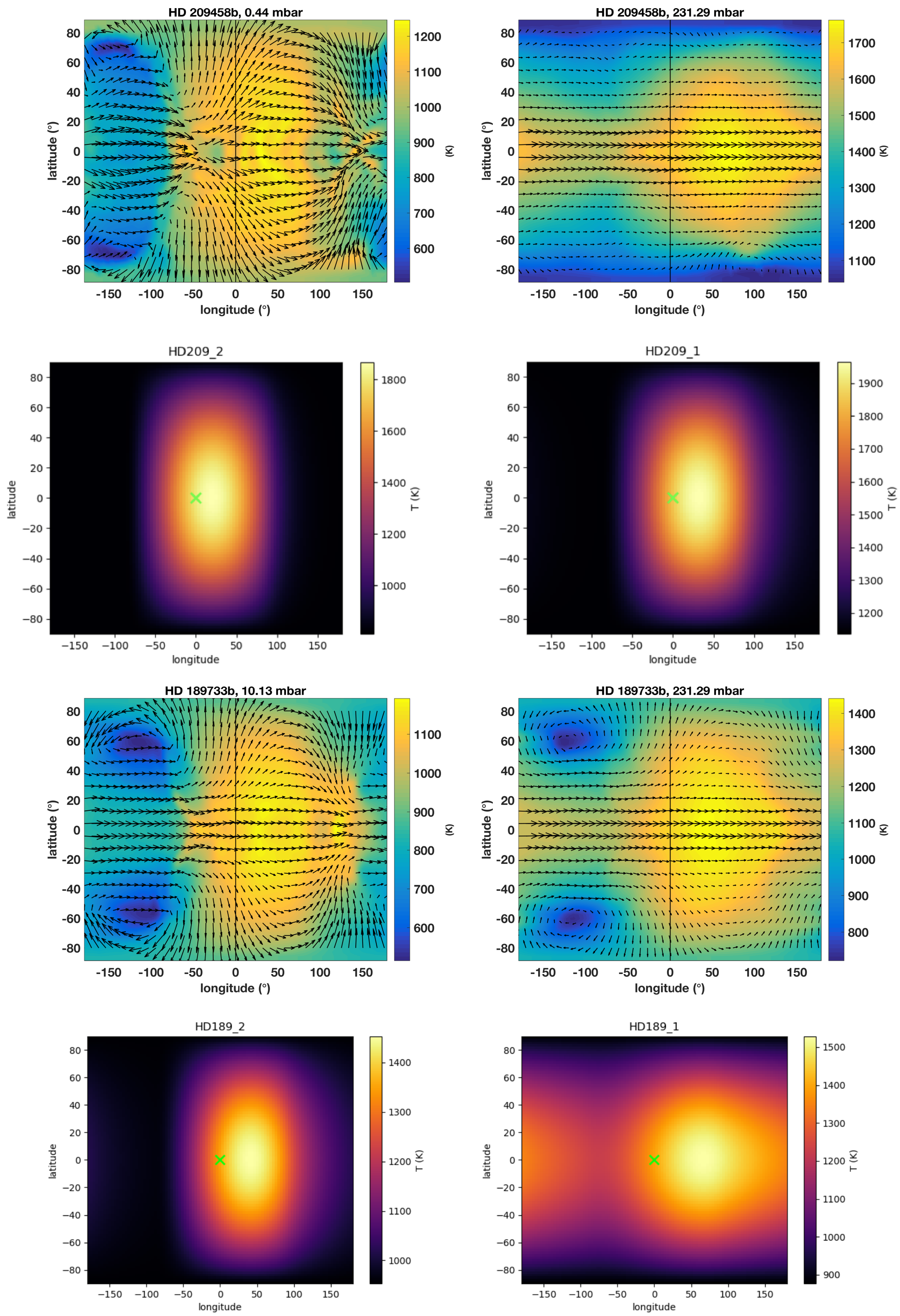

Figure 5.4 Top row: GCM outputs for HD 209458b at representative pressure levels for observations at 4.5 μm (left) and 3.6 μm (right). Second row: Mercator projections of the retrieved brightness maps for comparison. This patttern is repeated for rows three and four with HD 189733b as the target.

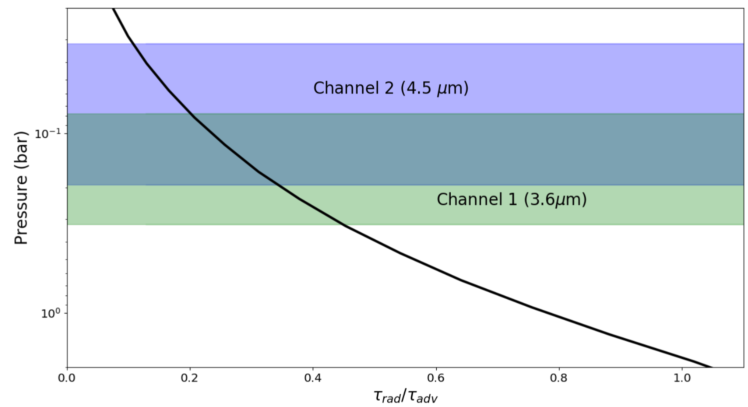

Figure 5.5 Model predictions for the ratio of radiative to advective timescales (τ_{rad}/τ_{adv}) as a function of pressure. The observations considered here with *Spitzer* channels 1 (green) and 2 (blue) probe pressurse where τ_{rad}/τ_{adv} should be less than 0.5.

HD 189733b

Comparisons of HD 189733b retrieved maps provide broad agreement with theoretical predictions at first glance, however, a closer look reveals potential problems. The general trend of seeing a greater hotspot offset in channel 2 than channel 1 is present in the results as well as the reduction in phase curve amplitude in channel 1 in comparison to channel 2. However, the combination of parameters used by Spiderman to replicate the shape are, perhaps, unphysical. The best fit value for ξ, the ratio of radiative to advective time scales, is 0.98 and 5.55 in channels 1 and 2 respectively. Figure 5.5 shows model predictions for ξ over the range of pressures accessed in these observations. The values of ξ retrieved from this study seem spurious are and likely due to a degeneracy in the solution. Further evaluation of this data priors on the values of ξ or different brightness models could possible show more agreement.

5.5.2 Mapping with JWST

Eclipse mapping is expected to be a major component of *JWST* observational efforts to constrain the 3D atmospheric processes of transiting exoplanets. The precision attainable with *JWST* will make eclipse mapping feasible in as few as one or two eclipses in many cases. Mapping with *JWST* will require much less observational time than full-orbit phase curves, making the observations more time-efficient. Furthermore, spectroscopic eclipse maps will provide 3D, not 2D, constraints on the winds, temperature, composition and chemistry of exoplanets over a wide parameter space. Already, planned *JWST* Early-Release Science (ERS) and Guaranteed Time Observations (GTO) programs will likely be able to perform spectroscopic eclipse mapping, including for HD 189733b. For example, the *JWST*-ERS Transiting Exoplanet Program (PI: Batalha) aims to perform spectroscopic eclipse mapping of the ultra-short hot Jupiter WASP-43b with *JWST*/MIRI (Bean et al. 2018). Eclipse observations of HD 189733b from the *JWST* GTO Program #1185 with *JWST*/NIRCam may be precise enough for spectroscopic eclipse mapping (Schlawin et al. 2018).

References

Ackerman, A. S. & Marley, M. S. 2001, ApJ, 556, 872

Adcroft, A., Hill, C., Campin, J.-M., Marshall, J., & Heimbach, P. 2004, in Seminar on Recent developments in numerical methods for atmospheric and ocean modelling, 6-10 September 2004, ECMWF (Shinfield Park, Reading: ECMWF), 139–150

Agol, E., Cowan, N. B., Knutson, H. A., Deming, D., Steffen, J. H., Henry, G. W., & Charbonneau, D. 2010, ApJ, 721, 1861

Bean, J. L., Stevenson, K. B., Batalha, N. M., Berta-Thompson, Z., Kreidberg, L., Crouzet, N., Benneke, B., Line, M. R., Sing, D. K., Wakeford, H. R., Knutson, H. A., Kempton, E. M.-R., Désert, J.-M., Crossfield, I., Batalha, N. E., de Wit, J., Parmentier, V., Harrington, J., Moses, J. I., Lopez-Morales, M., Alam, M. K., Blecic, J., Bruno, G., Carter, A. L., Chapman, J. W., Decin, L., Dragomir, D., Evans, T. M., Fortney, J. J., Fraine, J. D., Gao, P., García Muñoz, A., Gibson, N. P., Goyal, J. M., Heng, K., Hu, R., Kendrew, S., Kilpatrick, B. M., Krick, J., Lagage, P.-O., Lendl, M., Louden, T., Madhusudhan, N., Mandell, A. M., Mansfield, M., May, E. M., Morello, G., Morley, C. V., Nikolov, N., Redfield, S., Roberts, J. E., Schlawin, E., Spake, J. J., Todorov, K. O., Tsiaras, A., Venot, O., Waalkes, W. C., Wheatley, P. J., Zellem, R. T., Angerhausen, D., Barrado, D., Carone, L., Casewell, S. L., Cubillos, P. E., Damiano, M., de Val-Borro, M., Drummond, B., Edwards, B., Endl, M., Espinoza, N., France, K., Gizis, J. E., Greene, T. P., Henning, T. K., Hong, Y., Ingalls, J. G., Iro, N., Irwin, P. G. J., Kataria, T., Lahuis, F., Leconte, J., Lillo-Box, J., Lines, S., Mancini, L., Marchis, F., Mayne, N., Palle, E., Roudier, G., Shkolnik, E. L., Southworth, J., Teske, J., Tinetti, G., Tremblin, P., Tucker, G. S., vanBoekel, R., Waldmann, I. P., Weaver, I. C., & Zingales, T. 2018, ArXiv e-prints

Cooper, C. S. & Showman, A. P. 2005, ApJ, 629, L45

de Wit, J., Gillon, M., Demory, B.-O., & Seager, S. 2012, A&A, 548, A128

Dobbs-Dixon, I. & Agol, E. 2013, MNRAS, 435, 3159

Dobbs-Dixon, I. & Lin, D. N. C. 2008, ApJ, 673, 513

Foreman-Mackey, D., Hogg, D. W., Lang, D., & Goodman, J. 2013, PASP, 125, 306

Gelman, A. & Rubin, D. B. 1992, Statistical science, 457

Heng, K., Menou, K., & Phillipps, P. J. 2011, MNRAS, 413, 2380

Ingalls, J. G., Krick, J. E., Carey, S. J., Laine, S., Surace, J. A., Glaccum, W. J., Grillmair, C. C., & Lowrance, P. J. 2012, in SPIE Astronomical Telescopes+ Instrumentation, International Society for Optics and Photonics, 84421Y–84421Y

Ingalls, J. G., Krick, J. E., Carey, S. J., Laine, S., Surace, J. A., Glaccum, W. J., Grillmair, C. C., & Lowrance, P. J. 2012, in Proc. SPIE, Vol. 8442, Space Telescopes and Instrumentation 2012: Optical, Infrared, and Millimeter Wave, 84421Y

Ingalls, J. G., Krick, J. E., Carey, S. J., Stauffer, J. R., Lowrance, P. J., Grillmair, C. J., Buzasi, D., Deming, D., Diamond-Lowe, H., Evans, T. M., Morello, G., Stevenson, K. B., Wong, I., Capak, P., Glaccum, W., Laine, S., Surace, J., & Storrie-Lombardi, L. 2016, AJ, 152, 44

Kataria, T., Sing, D. K., Lewis, N. K., Visscher, C., Showman, A. P., Fortney, J. J., & Marley, M. S. 2016, ApJ, 821, 9

Kilpatrick, B. M., Kataria, T., Lewis, N. K., Zellem, R. T., Henry, G. W., Cowan, N. B., De Wit, J., Fortney, J. J., Knutson, H., Seager, S., Showman, A. P., & Tucker, G. S. 2019, arXiv e-prints

Kilpatrick, B. M., Lewis, N. K., Kataria, T., Deming, D., Ingalls, J. G., Krick, J. E., & Tucker, G. S. 2017, AJ, 153, 22

Knutson, H. A., Charbonneau, D., Allen, L. E., Fortney, J. J., Agol, E., Cowan, N. B., Showman, A. P., Cooper, C. S., & Megeath, S. T. 2007, Nature, 447, 183

Knutson, H. A., Lewis, N., Fortney, J. J., Burrows, A., Showman, A. P., Cowan, N. B., Agol, E., Aigrain, S., Charbonneau, D., Deming, D., Désert, J.-M., Henry, G. W., Langton, J., & Laughlin, G. 2012, ApJ, 754, 22

Lewis, N. K., Knutson, H. A., Showman, A. P., Cowan, N. B., Laughlin, G., Burrows, A., Deming, D., Crepp, J. R., Mighell, K. J., Agol, E., Bakos, G. Á., Charbonneau, D., Désert, J.-M., Fischer, D. A., Fortney, J. J., Hartman, J. D., Hinkley, S., Howard, A. W., Johnson, J. A., Kao, M., Langton, J., & Marcy, G. W. 2013, ApJ, 766, 95

Lewis, N. K., Showman, A. P., Fortney, J. J., Marley, M. S., Freedman, R. S., & Lodders, K. 2010, ApJ, 720, 344

Louden, T. & Kreidberg, L. 2017, SPIDERMAN: Fast code to simulate secondary transits and phase curves, Astrophysics Source Code Library

Majeau, C., Agol, E., & Cowan, N. B. 2012, ApJ, 747, L20

Marley, M. S. & McKay, C. P. 1999, , 138, 268

Mayne, N. J., Baraffe, I., Acreman, D. M., Smith, C., Browning, M. K., Skålid Amundsen, D., Wood, N., Thuburn, J., & Jackson, D. R. 2014, A&A, 561, A1

Menou, K. & Rauscher, E. 2010, ApJ, 713, 1174

Perna, R., Heng, K., & Pont, F. 2012, ApJ, 751, 59

Rauscher, E. & Kempton, E. M. R. 2014, ApJ, 790, 79

Rauscher, E., Suri, V., & Cowan, N. B. 2018, AJ, 156, 235

Schlawin, E., Greene, T. P., Line, M., Fortney, J. J., & Rieke, M. 2018, AJ, 156, 40

Showman, A. P., Cho, J. Y.-K., & Menou, K. 2010, Atmospheric Circulation of Exoplanets, ed. S. Seager, 471–516

Showman, A. P., Fortney, J. J., Lian, Y., Marley, M. S., Freedman, R. S., Knutson, H. A., & Charbonneau, D. 2009, ApJ, 699, 564

Showman, A. P. & Guillot, T. 2002, A&A, 385, 166

Thrastarson, H. T. & Cho, J. Y. 2010, ApJ, 716, 144

Zellem, R. T., Lewis, N. K., Knutson, H. A., Griffith, C. A., Showman, A. P., Fortney, J. J., Cowan, N. B., Agol, E., Burrows, A., Charbonneau, D., Deming, D., Laughlin, G., & Langton, J. 2014, ApJ, 790, 53

Zhang, X. & Showman, A. P. 2017, ApJ, 836, 73

Chapter 6

Observing Exoplanets in the Near-Infrared from a High Altitude Balloon Platform

The previous chapters of this dissertation have focused entirely on space based observatories. However, it was the idea to perform these same type of measurements from a balloon based platform that first piqued my interest and got me into this field. In this chapter I will present the science case for observing full orbit phase curves from a long duration balloon platform. The material presented here was based upon the science case for several iterations of proposals to NASA's ROSES APRA program. I managed the science case of these proposals in collaboration with co-authors. I will present limited discussion of the instrument and instrument performance; however, further details on the technical aspect of the observatory can be found in Tucker et al. (2018) and Nagler et al. (2019).

6.1 Introduction

Efforts to characterize exoplanet atmospheres have largely relied on space-based observatories such as the *Spitzer Space Telescope (Spitzer)* and *Hubble Space Telescope* (*HST*) to remove the influence of Earth's atmosphere and achieve the highest levels of spectrophotometric precision. However, for close-in exoplanets ($a < 0.1$ AU) – the best candidates for atmospheric characterization – neither *HST* nor *Spitzer* has the spectral coverage in the near-infrared (NIR) required to unambiguously map the temperature profile and chemical composition of a planet's atmosphere. Looking ahead, the James Webb Space Telescope (*JWST*) will not be able to access the very brightest targets that are best suited for global atmospheric characterization.

We proposed to develop and fly the EXoplanet Climate Infrared TElescope (EXCITE). EXCITE is a balloon-borne spectrograph that will address the limitations of current space-based NIR observatories while complementing and maximizing the science return of *JWST*. With a 0.5 m-class telescope, EXCITE will measure spectroscopic phase curves of bright, short-period extrasolar giant planets (EGPs, or "hot Jupiters") across the $1-4$ μm range. We will continuously observe each target for a full orbital period and use the resulting phase-resolved spectroscopy to map the planet's temperature profile and chemical composition as a function of longitude. EXCITE will be unique in its capability to provide spectroscopic phase curves for many bright EGPs over a spectral range that covers the peak in the planet's spectral energy distribution (SED). These data, combined with state-of-the-art 3D general circulation models (GCMs), will be used to study the atmospheric dynamics and chemistry in strongly-irradiated planets. This comparison of 3D GCMs to high quality data from EXCITE will enable us to refine the models and improve their predictive power when applied to datasets from future space telescopes like *JWST* and *ARIEL*.

For EGPs, the $1-4$ μm range contains both the peak of the planet's SED and spectral features from a number of key atmospheric components such as H_2O, CO_2, CO, CH_4, TiO and VO. The interpretation of phase curves at one or two *Spitzer* wavelengths (3.6 and/or 4.5 μm) or over the narrow range covered by *HST* (1.1–1.7 μm) is ambiguous because both the bolometric flux and the SED vary around the planet, *e.g.*, the night side of the planet can appear dark at *HST* wavelengths either because the total flux is low or because there is strong absorption at these wavelengths. By observing through the peak of the SED, EXCITE will resolve this degeneracy and unambiguously measure the planet's global energy budget.

Flying on a long duration balloon (LDB), EXCITE will be the first dedicated instrument for exoplanet atmospheric characterization. EXCITE will observe from the upper stratosphere, where Earth's residual atmosphere is stable to a level which is not available to ground or airplane

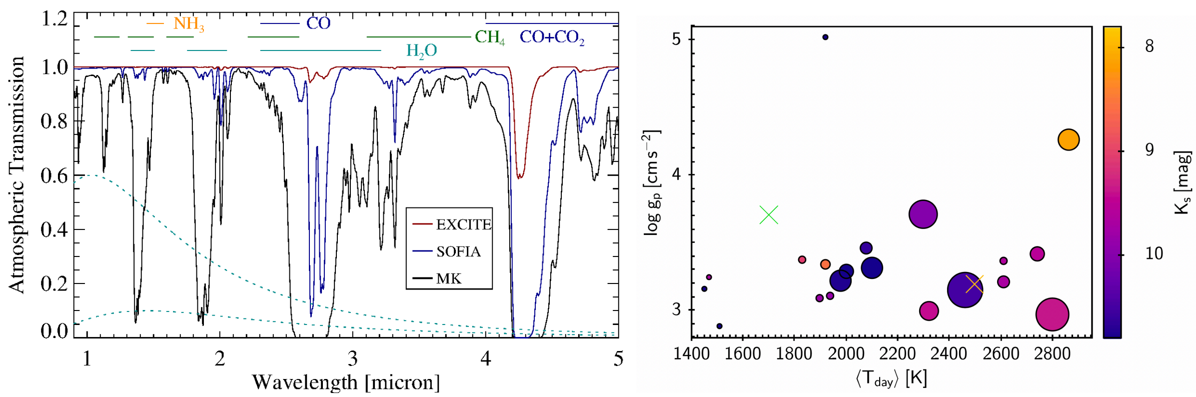

Figure 6.1 Left: The advantage of observing from the upper stratosphere, where Earth's residual atmosphere is stable and nearly transparent. Wavelengths of key molecular features for exoplanet atmosphere studies are indicated. Dotted lines are arbitrarily-scaled black body spectra at 1,800 K and 2,800 K, *i.e.*, typical day-side temperatures for our targets. Right: EXCITE will sample a vast physical parameter space. Shown are properties of targets visible in a single Antarctic LDB flight. Many more targets will be discovered by the Transiting Exoplanet Survey Satellite (*TESS*). Planets in this plot with low surface gravities ($\log g_p$) are also suitable targets for study using transmission spectroscopy (*e.g.*, with *JWST*). The crosses shows the properties of WASP-43b and WASP-103b, the only planets for which phase-resolved spectroscopy has been published Stevenson et al. (2014); Kreidberg et al. (2018).

instrumentation (Fig. 6.1). The instrument is capable of moderate resolution spectroscopy ($R \sim 50$) in the $1-4$ μm band with enough sensitivity and sufficient control of systematics to detect phase curve amplitude and offset over a range of atmospheric pressure levels. It will also detect key molecular signatures over a band which has not been previously exploited. EXCITE will be built using mostly off-the-shelf components, reducing risk and enabling us to build an instrument that will deliver cutting-edge results for only moderate cost.

6.2 Science Goals

The primary goal of EXCITE is to measure spectroscopic phase curves that constrain the global energy budget and circulation in hot Jupiters. Because each phase curve probes multiple wavelengths, and therefore pressures, these observations will map out the exoplanet's longitudinal heat distributions and vertical atmospheric structures. Considerable effort has gone into modeling the global circulation of hot Jupiters (e.g., Showman & Guillot 2002; Cooper & Showman 2005;

Cho et al. 2008; Showman et al. 2009; Langton & Laughlin 2007; Dobbs-Dixon et al. 2010; Menou & Rauscher 2009; Rauscher & Menou 2010; Lewis et al. 2010; Heng et al. 2011; Perna et al. 2012; Showman et al. 2013; Kataria et al. 2013; Lewis et al. 2014; Zhang & Showman 2017; Mayne et al. 2017; Drummond et al. 2018; Lines et al. 2018), but there is still very little spectroscopic data that can be used to study their global atmospheric properties.

A dedicated instrument optimized for exoplanet spectroscopy is the only way to obtain data of the quantity and quality needed to substantially advance our understanding of hot Jupiter climates (Fig. 6.1).

Although there exists a large sample of known exoplanets, not all exoplanets are suitable for atmospheric characterization studies. The signal size from the planet is always small compared to the signal from the host star ($\sim 10^{-4}$ or less), so bright targets are needed for detailed study. Planets that transit their host star as seen from Earth present the best opportunity for atmospheric characterization through transmission, emission, and phase curve observations. The masses and radii of transiting planets are known to good accuracy from the analysis of the transit light curve and the orbital radial velocity curve of the host star. With orbital periods $\lesssim 3$ days, hot Jupiters are tidally-locked, so there is strong temperature contrast between the permanent "day-side" hemisphere that is irradiated by the host star and the dark "night-side". Such targets are well suited for atmospheric characterization.

The orbit of the planet about the host star produces a time-varying signal in the apparent flux (as the observer views the day and night sides of the planet) that is some fraction of the planet-star flux ratio. As the planet transits its host star, starlight is filtered through the planetary atmosphere resulting in transmission spectra that can constrain the planet's atmospheric composition. However, transits alone paint an incomplete picture of the planetary atmosphere as they only probe the atmospheric region near the limb of the planet at relatively low pressures. When the planet passes behind its host star as seen from Earth (eclipse), day-side thermal emission measurements can be made that add additional information about atmospheric composition, vertical thermal structure, and circulation processes. Still, eclipse observations provide a hemispheric average of only the planet's day-side properties.

Phase curve observations measure the emitted flux of a planetary atmosphere across all longitudes, effectively enabling us to study how atmospheric properties vary with temperature for a fixed elemental composition and gravity Parmentier & Crossfield (2017). The amplitude of phase curve variations in the NIR constrain the efficiency with which the planet recirculates energy from its permanent day side to its night side (e.g., Cowan & Agol 2011b). The phase at which the peak of the phase curve occurs measures the offset of the brightest point on the planet from the sub-stellar point and indicates the relative strength of radiative and dynamical timescales in the planet's atmosphere (e.g., Showman et al. 2009; Cowan & Agol 2011a). Phase curve observations provided the first clear indication of the presence of strong winds in exoplanetary atmospheres Knutson et al. (2007). The overall shape of the phase curve can reveal chemical gradients in the planet's atmosphere (e.g., Knutson et al. 2012; Lewis et al. 2014). The presence of a coupling between magnetic field and the ions in very hot planets can produce magnetically driven oscillations in the jet, which can only be seen through phase curves Rogers & Komacek (2014); Armstrong et al. (2016); Rogers (2017); Hindle et al. (2019).

The synergy between spectroscopic phase curve measurements and transit/eclipse spectroscopy is a key strength of EXCITE. Spectroscopic phase curve observations are especially powerful as they probe a wide range of pressure levels in the planet's atmosphere as the atmosphere's opacity changes as a function of wavelength. Comparisons of phase curves measured at a range of wavelengths reveal how the relevant radiative, chemical, and dynamical timescales vary as a function of atmospheric pressure, and therefore altitude. In addition to spectroscopic phase curve observations, EXCITE will naturally observe secondary eclipses and transits. Measuring the planetary phase curve allows us to constrain the global and spatially resolved energy budget of the planet, whereas transit/eclipse spectroscopy will provide the chemical bulk-compositions at the day side and the terminator as well as a direct measurement of the vertical temperature profile of the atmosphere at the day side. By observing through the peak of the exoplanet's SED (~ 2 μm), EXCITE can directly constrain the global energy budget and circulation patterns that result from the extreme irradiation of hot Jupiters. Furthermore, we can explore how the bulk chemistry and dynamics of exoplanets vary with increasing equilibrium temperature and surface gravity. This will further enable us to make links between exoplanets and brown dwarfs, which can have similar equilibrium temperatures, but much higher surface gravities, than their planetary counterparts.

EXCITE will advance our understanding of the diversity of hot Jupiters and the differences in the physics and chemistry of their atmospheres, particularly with respect to cloud formation and distribution. In the 1,300 K – 3,000 K equilibrium temperature range, Brown Dwarfs are classified into three main classes (M, L and T), each of them divided into a dozen subclasses. The M to L transition is marked by the disappearance of the titanium oxide absorption bands while the L to T transition is driven by the disappearance of silicate clouds. Although hot Jupiters share the same range of equilibrium temperature as Brown Dwarfs, and probably have a similar chemical composition, they have always been considered as a single class of objects. Tentative evidence of transitions similar to the M/L and L/T Brown Dwarf transitions have been discovered in the past years, but no definitive conclusion has been put forward, mainly because current observations are too narrow in wavelength or in parameter space. By performing a broad survey in equilibrium temperature, EXCITE will confirm the presence of these transitions and determine with better precision at what temperature they happen. EXCITE will define a first spectral classification for hot Jupiters.

Evidence of a L/T-like transition has recently been found by analyzing the phase curves obtained by *Kepler* in the optical bandpass. These observations show a prevalence of clouds in the western part of the dayside atmosphere of hot Jupiters, away from the hot spot (Demory et al. 2013; Esteves et al. 2015; Angerhausen et al. 2015; Hu et al. 2015; Shporer & Hu 2015; Webber et al. 2015; Shporer 2017; Stevenson et al. 2017; Mendonça et al. 2018). Such a prevalence of inhomogeneously cloudy daysides can be understood if planets of different equilibrium temperature possess clouds of different chemical composition (Parmentier et al. 2016). In particular silicate clouds are expected to disappear in planets cooler than 1,600K. Such a

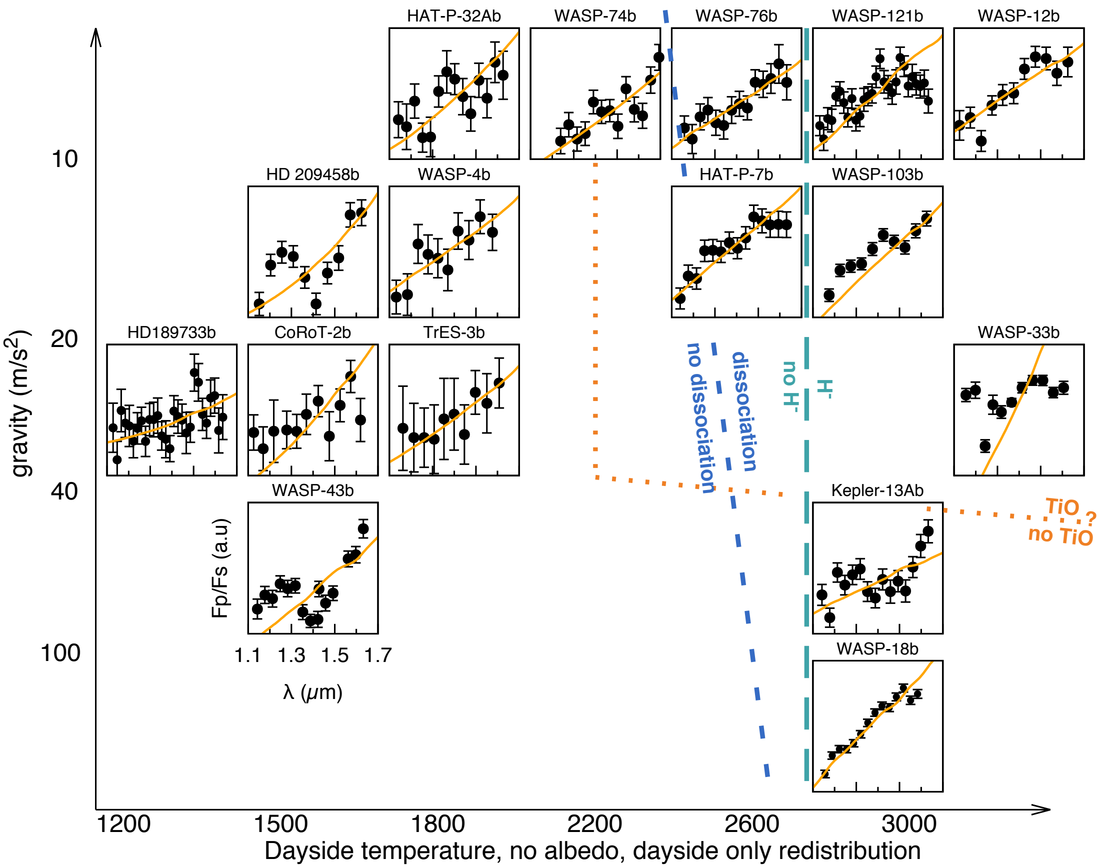

Figure 6.2 Previous secondary eclipse observations with WFC3 show an assortment of results including features in both absorption and emission as well as featureless blackbodies. Recent theory attempts to explain featureless ultra-hot planets via water dissociation but is not yet fully tested. The diversity of spectra at lower temperatures could be the result of a number of different processes and need to be explored in breadth to uncover the patterns.

variation of the cloud composition with equilibrium temperature is expected to produce large variations in the mid-IR phase curve offset as a function of equilibrium temperature. EXCITE will confirm the disappearance of silicate clouds by sampling the large variation in phase curve offset predicted between 1,400 K and 1,800 K.

Theory predicts that hot Jupiters with temperatures greater than 2000 K should have thermal inversions and molecular features in emission, while hot Jupiters at cooler temperatures (<1750 K) should have non-inverted atmospheres and large absorption features (Fortney et al. 2008).

Observationally, we have seen a diversity of thermal emission spectra (see Figure 6.2). Many cooler planets do show prominent absorption features (e.g. Kreidberg et al. 2014; Stevenson et al.

2014; Line et al. 2016) and some hotter planets do indeed show emission features indicative of thermal inversions, albeit with weaker strengths than was predicted (e.g. Haynes et al. 2015; Evans et al. 2017). Still, others show featureless, blackbody-like spectra (e.g. Swain et al. 2013; Cartier et al. 2017). Given the current data, it is still unclear where these transitions take place and what physical processes are governing them because there are planets that strongly deviate from the model predictions. Fortney et al. (2008) predicts the transition will take place $\sim$ 1800 K if gas phase TiO and VO are the absorbers responsible for the inversion. Providing a constraint on the temperature at which the transition takes place will provide evidence, one way or the other, whether that assumption is true.

Recent work (*e.g.*, Arcangeli et al. 2018; Kreidberg et al. 2018; Lothringer et al. 2018; Parmentier et al. 2018; Kitzmann et al. 2018; Bell & Cowan 2018; Komacek & Tan 2018) has shown that many molecular species (*e.g.*, H_2, H_2O, TiO, VO) should dissociate on the planet day-side for very hot planets ($T_{eq} \sim 2200$ K), but recombine on the night-side. H^- becomes an important opacity source on the day-side between 1 and 1.5 μm. As a consequence, the $1-2$ μm day-side spectrum closely resembles a blackbody spectrum with a reduced water feature due to dissociation and presence of H^- opacity in the water gaps. This limits the information that can be derived from short wavelength spectra. One molecule that does not dissociate until even higher temperatures is CO. As a result, at wavelengths longer than 2 μm there are strong features to be observed in emission spectra: the CO feature at ~ 2.5 μm and the resurgence of H_2O because of the higher opacity and the lack of absorption from H^-. EXCITE's broad spectral coverage maximizes the information that can be derived from a spectroscopic phase curve.

6.3 Experimental Approach

Despite the wealth of information contained in infrared phase curves, only a handful of such observations are present in the literature (Cowan et al. 2012; Knutson et al. 2012; Maxted et al. 2013; Lewis et al. 2013; Zellem et al. 2014; Stevenson et al. 2014, 2017; Kreidberg et al. 2018).

Table 6.1 Comparison of instruments that operate in the $1-4$ μm band.

Instrument	Wavelength Coverage	Notes
EXCITE	$1-4$ μm	Dedicated observatory. Obtains phase curves through peak of planet's SED in single, continuous observations.
HST/WFC3	$1.1-1.7$ μm	Shared observatory. Required ~ 60 orbits to measure a single spectroscopic phase curve. Limited bandpass.
Spitzer/IRAC	3.6 μm, 4.5 μm	Shared observatory. Instrument will go offline in 2020.
JWST/NIRSpec	$1-5$ μm	Shared observatory. Cannot access targets brighter than 9.83 J magnitude, thus excluding the best EGPs.
ARIEL	$1.95-7.80$ μm	Shared observatory. Will not launch until 2028.

These observations are costly and difficult to obtain with general-user instruments. There are only two spectroscopic phase curve measurements in the literature Stevenson et al. (2014); Kreidberg et al. (2018); the first required ~ 60 *HST* orbits to measure a single exoplanet orbit, and the second required 46 hours of *HST* time and 60 hours of *Spitzer* time to do the same. The observed planets have orbital periods of under 22 hours.

As the observing histories of both *HST* and *Spitzer* have shown, the long-duration stares required for phase curve observations are seen as too burdensome for the limited, and shared, resources of space observatories. As a result, we cannot rely on *JWST* for these measurements Parmentier & Crossfield (2017). Rather, a purpose-built instrument is needed.

Unlike multi-use space-based missions with spectroscopic instruments such as *HST* and *JWST*, EXCITE is designed specifically to measure the broadband spectra of exoplanets over the $1-4$ μm band in a single orbital period observation. Table 6.1 summarizes EXCITE's experimental approach and compares it to current and future space-based instruments that operate in the $1-4$ μm band. Among these instruments, only the *NIRSpec* prism and *ARIEL* can cover the 1–4 μm wavelength range in a single observation. However, the *NIRSpec* prism is unable to access targets brighter than 9.83 J magnitude (Nielsen et al. 2016), thus excluding both the best targets for atmospheric characterization and new bright systems *TESS* Sullivan et al. (2015) will discover. *ARIEL* is likely to perform phase-resolved spectroscopy, but it will not launch until 2028. Multiple visits with *JWST* using multiple instruments can be used to build up the spectroscopic phase curve over the 1–4 μm wavelength range, but this expensive and time-consuming option is a poor use of the time available. Much better is using EXCITE to observe 1–4 μm at low resolution and *JWST* to observe selected features at high resolution, thereby maximizing the exoplanet science that can be done with precious *JWST* time.

References

Angerhausen, D., DeLarme, E., & Morse, J. A. 2015, PASP, 127, 1113

Arcangeli, J., Désert, J.-M., Line, M. R., Bean, J. L., Parmentier, V., Stevenson, K. B., Kreidberg, L., Fortney, J. J., Mansfield, M., & Showman, A. P. 2018, ApJ, 855, L30

Armstrong, D. J., de Mooij, E., Barstow, J., Osborn, H. P., Blake, J., & Saniee, N. F. 2016, Nature Astronomy, 1, 0004

Bell, T. J. & Cowan, N. B. 2018, ApJ, 857, L20

Cartier, K. M. S., Beatty, T. G., Zhao, M., Line, M., Ngo, H., Mawet, D., Stassun, K. G., Wright, J. T., Kreidberg, L., Fortney, J., & Knutson, H. 2017, AJ, 153, 34

Cho, J. Y.-K., Menou, K., Hansen, B. M. S., & Seager, S. 2008, ApJ, 675, 817

Cooper, C. S. & Showman, A. P. 2005, ApJ, 629, L45

Cowan, N. B. & Agol, E. 2011a, ApJ, 726, 82

—. 2011b, ApJ, 729, 54

Cowan, N. B., Machalek, P., Croll, B., Shekhtman, L. M., Burrows, A., Deming, D., Greene, T., & Hora, J. L. 2012, ApJ, 747, 82

Demory, B.-O., de Wit, J., Lewis, N., Fortney, J., Zsom, A., Seager, S., Knutson, H., Heng, K., Madhusudhan, N., Gillon, M., Barclay, T., Desert, J.-M., Parmentier, V., & Cowan, N. B. 2013, ApJ, 776, L25

Dobbs-Dixon, I., Cumming, A., & Lin, D. N. C. 2010, ApJ, 710, 1395

Drummond, B., Mayne, N. J., Baraffe, I., Tremblin, P., Manners, J., Amundsen, D. S., Goyal, J., & Acreman, D. 2018, ArXiv e-prints

Esteves, L. J., De Mooij, E. J. W., & Jayawardhana, R. 2015, ApJ, 804, 150

Evans, T. M., Sing, D. K., Kataria, T., Goyal, J., Nikolov, N., Wakeford, H. R., Deming, D., Marley, M. S., Amundsen, D. S., Ballester, G. E., Barstow, J. K., Ben-Jaffel, L., Bourrier, V., Buchhave, L. A., Cohen, O., Ehrenreich, D., García Muñoz, A., Henry, G. W., Knutson, H., Lavvas, P., Lecavelier Des Etangs, A., Lewis, N. K., López-Morales, M., Mandell, A. M., Sanz-Forcada, J., Tremblin, P., & Lupu, R. 2017, Nature, 548, 58

Fortney, J. J., Lodders, K., Marley, M. S., & Freedman, R. S. 2008, ApJ, 678, 1419

Haynes, K., Mandell, A. M., Madhusudhan, N., Deming, D., & Knutson, H. 2015, ApJ, 806, 146

Heng, K., Menou, K., & Phillipps, P. J. 2011, MNRAS, 413, 2380

Hindle, A. W., Bushby, P. J., & Rogers, T. M. 2019, ApJ, 872, L27

Hu, R., Demory, B.-O., Seager, S., Lewis, N., & Showman, A. P. 2015, ApJ, 802, 51

Kataria, T., Showman, A. P., Lewis, N. K., Fortney, J. J., Marley, M. S., & Freedman, R. S. 2013, ApJ, 767, 76

Kitzmann, D., Heng, K., Rimmer, P. B., Hoeijmakers, H. J., Tsai, S.-M., Malik, M., Lendl, M., Deitrick, R., & Demory, B.-O. 2018, ApJ, 863, 183

Knutson, H. A., Charbonneau, D., Allen, L. E., Fortney, J. J., Agol, E., Cowan, N. B., Showman, A. P., Cooper, C. S., & Megeath, S. T. 2007, Nature, 447, 183

Knutson, H. A., Lewis, N., Fortney, J. J., Burrows, A., Showman, A. P., Cowan, N. B., Agol, E., Aigrain, S., Charbonneau, D., Deming, D., Désert, J.-M., Henry, G. W., Langton, J., & Laughlin, G. 2012, ApJ, 754, 22

Komacek, T. D. & Tan, X. 2018, Research Notes of the American Astronomical Society, 2, 36

Kreidberg, L., Bean, J. L., Désert, J.-M., Line, M. R., Fortney, J. J., Madhusudhan, N., Stevenson, K. B., Showman, A. P., Charbonneau, D., McCullough, P. R., Seager, S., Burrows, A., Henry, G. W., Williamson, M., Kataria, T., & Homeier, D. 2014, ApJ, 793, L27

Kreidberg, L., Line, M. R., Parmentier, V., Stevenson, K. B., Louden, T., Bonnefoy, M., Faherty, J. K., Henry, G. W., Williamson, M. H., Stassun, K., Beatty, T. G., Bean, J. L., Fortney, J. J., Showman, A. P., Désert, J.-M., & Arcangeli, J. 2018, AJ, 156, 17

Langton, J. & Laughlin, G. 2007, ApJ, 657, L113

Lewis, N. K., Knutson, H. A., Showman, A. P., Cowan, N. B., Laughlin, G., Burrows, A., Deming, D., Crepp, J. R., Mighell, K. J., Agol, E., Bakos, G. Á., Charbonneau, D., Désert, J.-M., Fischer, D. A., Fortney, J. J., Hartman, J. D., Hinkley, S., Howard, A. W., Johnson, J. A., Kao, M., Langton, J., & Marcy, G. W. 2013, ApJ, 766, 95

Lewis, N. K., Showman, A. P., Fortney, J. J., Knutson, H. A., & Marley, M. S. 2014, ApJ, 795, 150

Lewis, N. K., Showman, A. P., Fortney, J. J., Marley, M. S., Freedman, R. S., & Lodders, K. 2010, ApJ, 720, 344

Line, M. R., Stevenson, K. B., Bean, J., Desert, J.-M., Fortney, J. J., Kreidberg, L., Madhusudhan, N., Showman, A. P., & Diamond-Lowe, H. 2016, AJ, 152, 203

Lines, S., Mayne, N. J., Boutle, I. A., Manners, J., Lee, G. K. H., Helling, C., Drummond, B., Amundsen, D. S., Goyal, J., Acreman, D. M., Tremblin, P., & Kerslake, M. 2018, ArXiv e-prints

Lothringer, J. D., Barman, T., & Koskinen, T. 2018, ApJ, 866, 27

Maxted, P. F. L., Anderson, D. R., Doyle, A. P., Gillon, M., Harrington, J., Iro, N., Jehin, E., Lafrenière, D., Smalley, B., & Southworth, J. 2013, MNRAS, 428, 2645

Mayne, N. J., Debras, F., Baraffe, I., Thuburn, J., Amundsen, D. S., Acreman, D. M., Smith, C., Browning, M. K., Manners, J., & Wood, N. 2017, A&A, 604, A79

Mendonça, J. M., Malik, M., Demory, B.-O., & Heng, K. 2018, ArXiv e-prints

Menou, K. & Rauscher, E. 2009, ApJ, 700, 887

Nagler, P. C., Edwards, B., Kilpatrick, B., Lewis, N. K., Maxted, P., Barth Netterfield, C., Parmentier, V., Pascale, E., Sarkar, S., Tucker, G. S., & Waldmann, I. 2019, arXiv e-prints, arXiv:1903.09718

Nielsen, L. D., Ferruit, P., Giardino, G., Birkmann, S., García Muñoz, A., Valenti, J., Isaak, K., Alves de Oliveira, C., Böker, T., Lützgendorf, N., Rawle, T., & Sirianni, M. 2016, in Proc. SPIE, Vol. 9904, Society of Photo-Optical Instrumentation Engineers (SPIE) Conference Series, 99043O

Parmentier, V. & Crossfield, I. J. M. 2017, Exoplanet Phase Curves: Observations and Theory, 116

Parmentier, V., Fortney, J. J., Showman, A. P., Morley, C., & Marley, M. S. 2016, ApJ, 828, 22

Parmentier, V., Line, M. R., Bean, J. L., Mansfield, M., Kreidberg, L., Lupu, R., Visscher, C., Désert, J.-M., Fortney, J. J., Deleuil, M., Arcangeli, J., Showman, A. P., & Marley, M. S. 2018, A&A, 617, A110

Perna, R., Heng, K., & Pont, F. 2012, ApJ, 751, 59

Rauscher, E. & Menou, K. 2010, ApJ, 714, 1334

Rogers, T. M. 2017, Nature Astronomy, 1, 0131

Rogers, T. M. & Komacek, T. D. 2014, ApJ, 794, 132

Showman, A. P., Fortney, J. J., Lewis, N. K., & Shabram, M. 2013, ApJ, 762, 24

Showman, A. P., Fortney, J. J., Lian, Y., Marley, M. S., Freedman, R. S., Knutson, H. A., & Charbonneau, D. 2009, ApJ, 699, 564

Showman, A. P. & Guillot, T. 2002, A&A, 385, 166

Shporer, A. 2017, ArXiv e-prints

Shporer, A. & Hu, R. 2015, AJ, 150, 112

Stevenson, K. B., Désert, J.-M., Line, M. R., Bean, J. L., Fortney, J. J., Showman, A. P., Kataria, T., Kreidberg, L., McCullough, P. R., Henry, G. W., Charbonneau, D., Burrows, A., Seager, S., Madhusudhan, N., Williamson, M. H., & Homeier, D. 2014, Science, 346, 838

Stevenson, K. B., Line, M. R., Bean, J. L., Désert, J.-M., Fortney, J. J., Showman, A. P., Kataria, T., Kreidberg, L., & Feng, Y. K. 2017, AJ, 153, 68

Sullivan, P. W., Winn, J. N., Berta-Thompson, Z. K., Charbonneau, D., Deming, D., Dressing, C. D., Latham, D. W., Levine, A. M., McCullough, P. R., Morton, T., Ricker, G. R., Vanderspek, R., & Woods, D. 2015, ApJ, 809, 77

Swain, M., Deroo, P., Tinetti, G., Hollis, M., Tessenyi, M., Line, M., Kawahara, H., Fujii, Y., Showman, A. P., & Yurchenko, S. N. 2013, , 225, 432

Tucker, G. S., Nagler, P., Butler, N., Kilpatrick, B., Korotkov, A., Lewis, N., Maxted, P. F. L., Miko, L., Netterfield, C. B., Pascale, E., Patience, J., Scowen, P., Parmentier, V., Waldmann, I., & Wen, Y. 2018, in Society of Photo-Optical Instrumentation Engineers (SPIE) Conference Series, Vol. 10702, Ground-based and Airborne Instrumentation for Astronomy VII, 107025G

Webber, M. W., Lewis, N. K., Marley, M., Morley, C., Fortney, J. J., & Cahoy, K. 2015, ApJ, 804, 94

Zellem, R. T., Lewis, N. K., Knutson, H. A., Griffith, C. A., Showman, A. P., Fortney, J. J., Cowan, N. B., Agol, E., Burrows, A., Charbonneau, D., Deming, D., Laughlin, G., & Langton, J. 2014, ApJ, 790, 53

Zhang, X. & Showman, A. P. 2017, ApJ, 836, 73

Chapter 7

Conclusions and Future Work

7.1 Conclusions

The mission in studying exoplanets is to answer a set of fundamental questions:

- What kinds of planetary systems orbit other stars in our galaxy?
- How common are solar systems like our own?
- What are exoplanets like?
- Are we alone?

I have sought out the answers to these questions by studying the bulk compositions, energy budgets, and atmospheres of exoplanets as probes of planetary formation, planetary diversity, and the search for habitability. My research has employed a multi-faceted approach to the characterization of exoplanet atmospheres. I have utilized a number of observational techniques and theoretical frameworks to explore atmospheric composition and structure at every region of the planetary atmospheres. I have placed an emphasis on ensuring robustness of scientific results by analyzing data with multiple methodologies and engaging diverse cross sections of the community in collaboration.

My work will serve as a benchmark for further high resolution mapping with future observatories. *JWST* will provide high precision spectroscopic data over wider wavelength ranges that will provide observers an opportunity to develop techniques to achieve high resolution pictures of thermal distributions. The techniques I am refining now will enable *JWST* to probe thermal distributions by extracting information from as little as a single secondary eclipse rather than investing days of continuous observations into full orbit phase curves. Multiple programs, including both Guaranteed Time Observer (GTO) and Early Release Science (Co-I: Kilpatrick), will perform observations aimed at providing higher resolution three dimensional maps by mapping exoplanet atmospheres spectroscopically.

7.2 Future Work

I plan to continue to employ a wide variety of observational techniques while developing a comprehensive data interpretation framework to synergistically provide a three dimensional view of atmospheric chemistry and structure. I will develop a framework in which to facilitate the comprehensive analysis of these observations by producing synthesized observations of model atmospheres with both non uniform thermal distributions and cloud cover across multiple instruments and observing strategies. Currently, a broad range of observational methodologies are often employed with a variety of instruments and observatories and analyzed independently of each other. We will only realize the full potential of these observations and achieve a complete picture of an exoplanetary atmosphere by combining the analysis of many methods simultaneously. Bringing to bear the synergy of multiple methodologies is key to achieving a comprehensive understanding of the chemistry and physics at work in exoplanet atmospheres.

It is imperative that as we await the observatories of the future we continue to refine our observational techniques while also developing the analysis frameworks necessary to comprehensively consider all of the information available. It is also equally as important that we remove unnecessary barriers to performing science by making tools available to the broader community. Developing open source community tools now will enable a more diverse group of researchers to ‘hit the ground running’ as new observatories come online and new data becomes available.

Appendix A

Posterior Distributions of Retrievals of the Atmospheric Composition of WASP-63b

Here we present the retrieval results as described in Section 3.4 from Kilpatrick et al. (2018). We present the pairs plots and fit to the observations in each case. In the case of the Line and Waldmann results we show both the thermochemically-consistent run along with the free retrieval for comparison.

A.1 Blecic & Cubillos

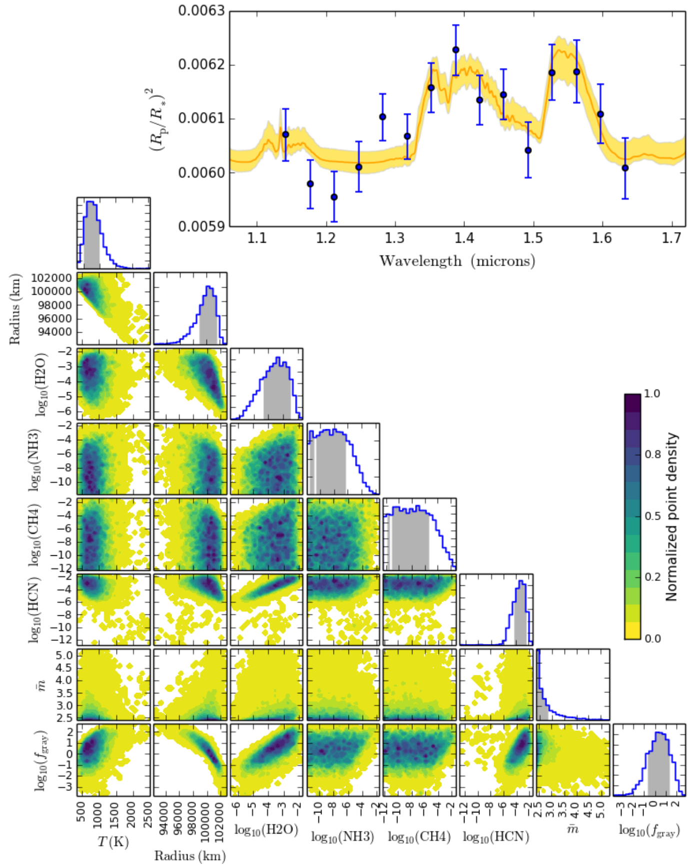

Figure A.1 Posteriors and fit from retrieval parameterized by free abundances of H_2O, NH_3, CH_4, and HCN along with the mean molecular mass of the atmosphere. The atmosphere is assumed to be isothermal (T as a free parameter) with a grey cloud (opacity as free parameter).

A.2 Line

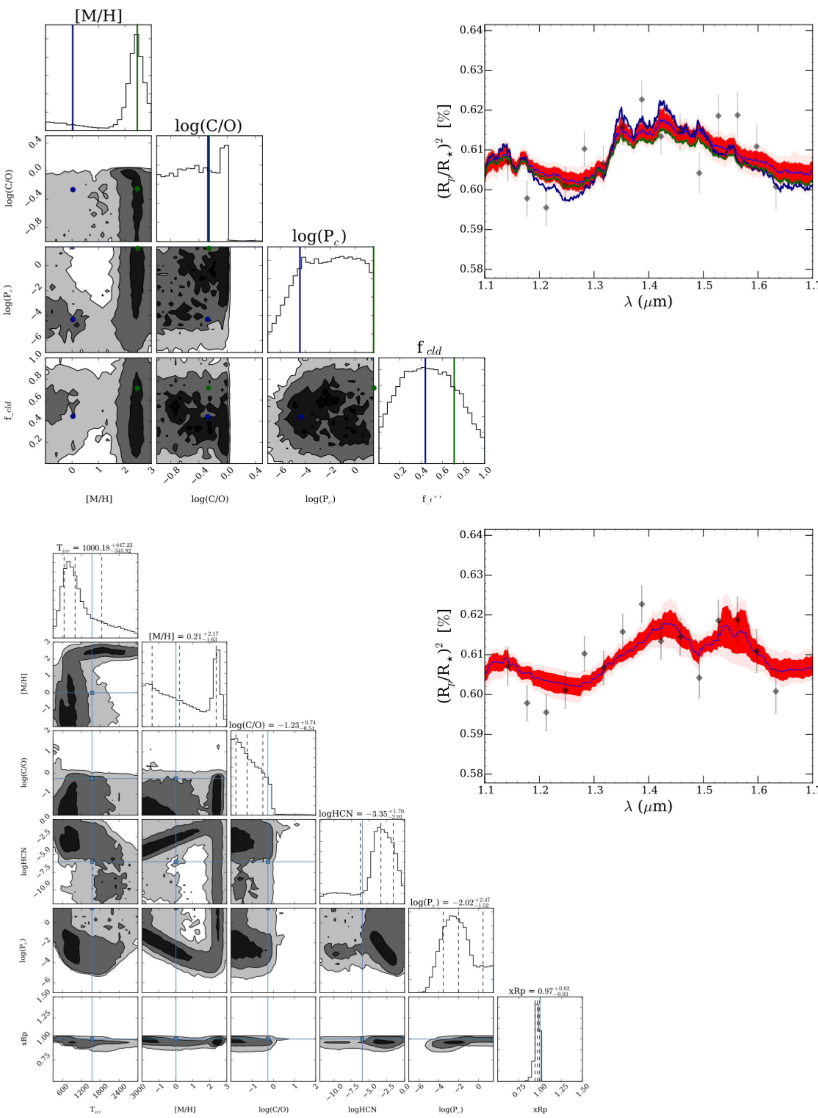

Figure A.2 *Top:* Posteriors and fit to spectrum of thermo-chemically consistent retrieval. The elemental abundances are parameterized by the metallicity $[\mathrm{M/H}]$, the carbon-to-oxygen ratio $\log(\mathrm{C/O})$, and the carbon- and nitrogen-species quench pressures. *Bottom:* Posteriors and fit to spectrum of assuming a thermo-chemically consistent atmosphere with the addition of HCN as a free parameter.

A.3 MacDonald & Madhusudhan

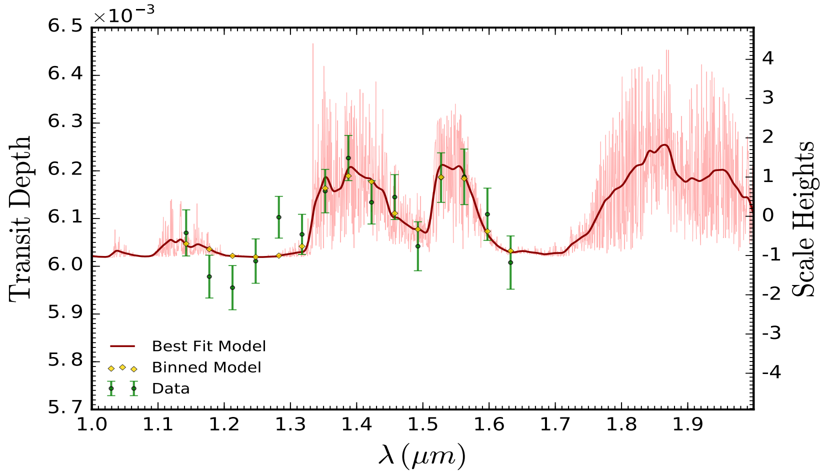

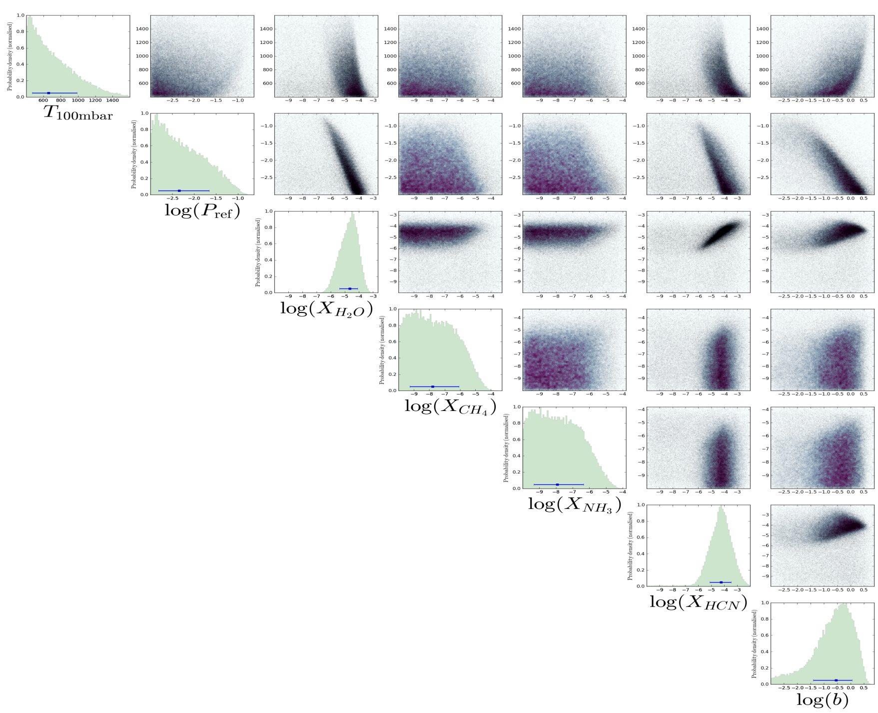

Figure A.3 *Top:* Fit to spectrum of free retrieval. *Bottom:* Posteriors of free retrieval assuming an isothermal temperature-pressure profile, including molecular opacities due to H_2O, CH_4, NH_3, and HCN, and clouds as a uniform-in-altitude gray opacity.

A.4 Waldmann

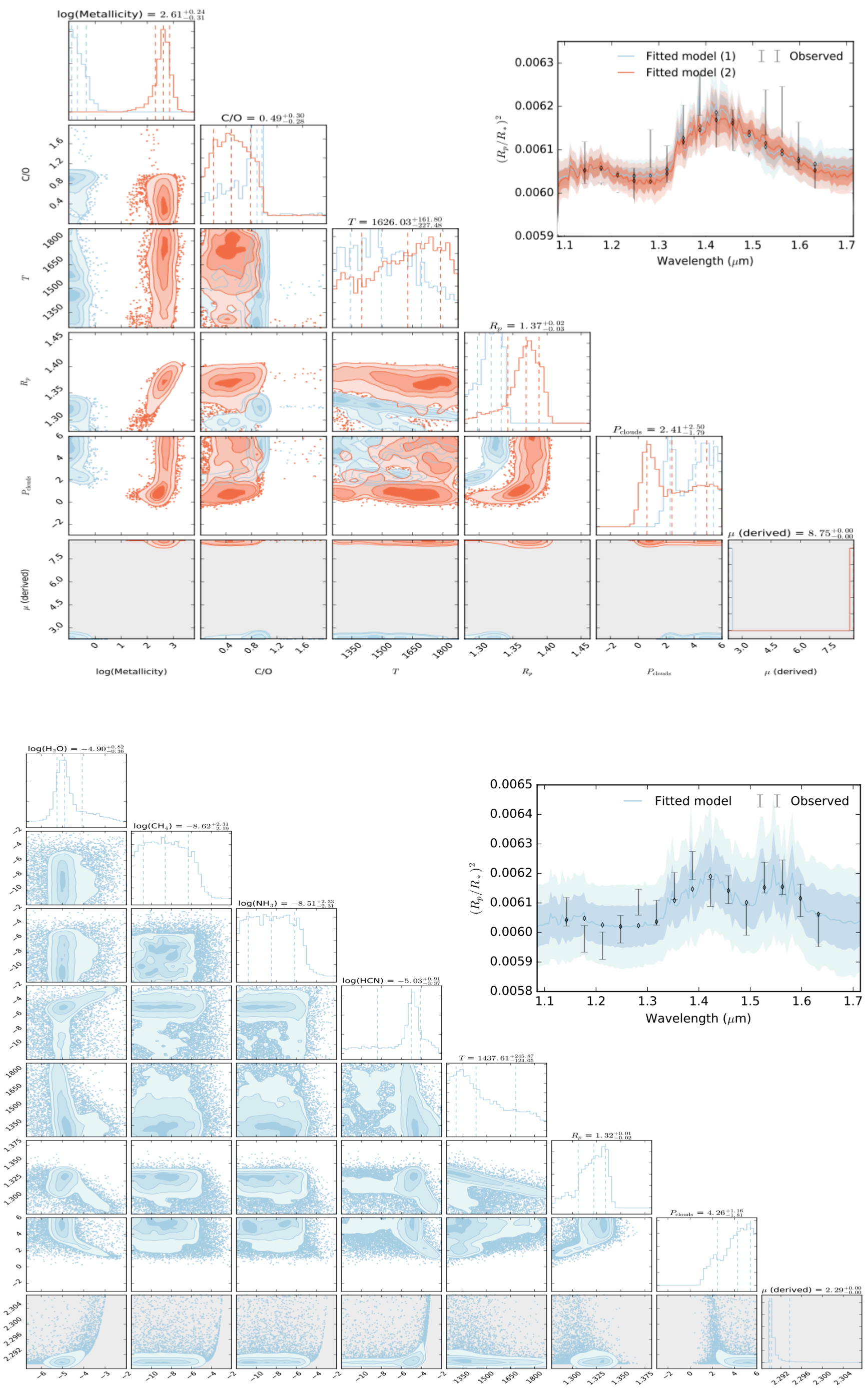

Figure A.4 *Top:* Posteriors and fit to spectrum of chemically consistent retrieval. The free parameters are the C/O ratio, atmospheric metallicity, planet radius, temperature and cloud-top pressure. *Bottom:* Posteriors and fit to spectrum of free retrieval with planet radius, temperature, cloud-top pressure and abundances of H_2O, CH_4, CO, CO_2, NH_3, and HCN as free parameters.

References

Kilpatrick, B. M., Cubillos, P. E., Stevenson, K. B., Lewis, N. K., Wakeford, H. R., MacDonald, R. J., Madhusudhan, N., Blecic, J., Bruno, G., Burrows, A., Deming, D., Heng, K., Line, M. R., Morley, C. V., Parmentier, V., Tucker, G. S., Valenti, J. A., Waldmann, I. P., Bean, J. L., Beichman, C., Fraine, J., Krick, J. E., Lothringer, J. D., & Mandell, A. M. 2018, AJ, 156, 103